Palaeomagnetic Assessment of High-Titanium Basalts from the Ethiopia-Yemen Traps Providing Insight into Volcanic Activity and Geomagnetic Field Behaviour

Baha' Naim Eid

München 2023

Palaeomagnetic Assessment of High-Titanium Basalts from the Ethiopia-Yemen Traps Providing Insight into Volcanic Activity and Geomagnetic Field Behaviour

Baha' Naim Eid

Dissertation

an der Fakultät für Geowissenschaften

der Ludwig-Maximilians-Universität

München

vorlegt von

Baha‘ Naim Eid

aus Libanon

München, den 13. März 2023

Disputation in München, den 17. Juli 2023

Erstgutachter: PD Dr. Florian Lhuillier

Zweitgutachter: Prof Dr. Pierre Rochette

Table of Contents

Preamble

This thesis is a monograph that represents the main contribution of my doctoral work and deals with the palaeomagnetism of the Ethiopia-Yemen traps emplaced 30 million years ago. It expands and discusses the results published in the two following papers:

Eid, B., Lhuillier, F., Gilder, S. A., Pfänder, J. A., Gebru, E. F., & Aßbichler, D. (2021). Exceptionally High Emplacement Rate of the Afar Mantle Plume Head. *Geophysical Research Letters*, *48*(23). https://doi.org/10.1029/2021GL094755

Eid, B., Lhuillier, F., Shcherbakov, V. P., & Shcherbakova, V. V. (2022). Do changes in geomagnetic secular variation, dipole moment and polarity reversal frequency correlate over the past 155 Myr? *Geophysical Journal International*, *230*(2), 1132–1146. https://doi.org/10.1093/gji/ggac112

Additionally, I also conducted during my doctoral work palaeomagnetic investigations on Late Cretaceous lava flows from the Okhotsk-Chukotka Volcanic Belt (NE Russia), the results of which were published in the three following papers:

Lebedev, I. E., Tikhomirov, P. L., Pasenko, A. M., **Eid, B.**, Lhuillier, F., & Pavlov, V. E. (2021). New Paleomagnetic Data on Late Cretaceous Chukotka Volcanics: the Chukotka Block Probably Underwent Displacements Relative to the North American and Eurasian Plates after the Formation of the Okhotsk-Chukotka Volcanic Belt? *Izvestiya, Physics of the Solid Earth, 57*(2), 232-246. https://doi.org/10.1134/S1069351321020014

Lebedev, I. E., Bobrovnikova, E. M., Tikhomirov, P. L., **Eid, B.**, Lhuillier, F., & Pavlov, V. E. (2022). Amplitude of Secular Geomagnetic Variation in Late Cretaceous Based on Paleomagnetic Studies of the Okhotsk–Chukotka Volcanic Belt from Upper Reaches of Malyi Anyui River, West Chukotka. *Izvestiya, Physics of the Solid Earth, 58*(2), 185-202. https://doi.org/10.1134/S1069351322020045

Bobrovnikova, E. M., Lhuillier, F., Shcherbakov, V. P., Shcherbakova, V. V., Zhidkov, G. V., Lebedev, I. E., **Eid, B.**, & Pavlov, V. E. (2022). High-latitude Paleointensities during the Cretaceous Normal Superchron from the Okhotsk-Chukotka Volcanic Belt. *Journal of Geophysical Research: Solid Earth, 127*, e2021JB023551. https://doi.org/10.1029/2021jb023551

Finally, I also conducted palaeomagnetic investigations on Palaeocene lava flows from Central Asia, the results of which were published in

Meng, J., Lhuillier, F., Wang, C., Liu, H., **Eid, B.**, & Li, Y. (2020). Paleomagnetism of Paleocene-Maastrichtian (60–70 Ma) Lava Flows From Tian Shan (Central Asia): Directional Analysis and Paleointensities. *Journal of Geophysical Research: Solid Earth, 125*, e2019JB018631. https://doi.org/10.1029/2019JB018631.

My main contribution in these latter four publications was to conduct palaeodirectional and absolute palaeointensity experiments and interpret the obtained results. The most reliable estimates of reconstructed dipole field strength were included into the global absolute palaeointensity database, which is used in this thesis to comment on the behaviour of Earth's magnetic field over the past 155 million years.

Summary

The geomagnetic field has its origins in the thermo-chemical convection of a liquid iron-nickel alloy in Earth's outer core. Changes in palaeosecular variation (PSV), dipole strength and polarity reversal frequency are salient features of Earth's magnetic field over the geological past, yet how these changes are linked by the geodynamo remains controversial. For the purpose of shedding light on these questions, we investigated a 1-km-thick sequence of lava flows (termed hereafter the Waja section) that erupted over the Afar plume axis of the ~31 Ma Ethiopia-Yemen Traps.

As the duration of the Waja section turned out to be much shorter than expected, we first strove to better understand the emplacement history of the Ethiopia-Yemen Traps. The Waja section, characterized by high-titanium concentrations (TiO_2 3.9 ± 0.5 wt%) in basalts close to picritic compositions, was emplaced at 31.18 ± 0.28 Ma (95% confidence) based on indistinguishable $^{40}Ar/^{39}Ar$ ages throughout the section. This date, together with solely normal polarity magnetization directions in 68 geomagnetically independent horizons, constrain the eruption to within chron C12n, with a maximum duration of a few hundreds of kyr for the entire 1-km-thick section. The rate of geomagnetic secular variation used as a chronometer refines the duration to only a few tens of kyr, leading to a local extrusion rate of 4–13 km^3/yr for the Afar plume head, which greatly exceeds the average rate of 0.3–1.2 km^3/yr for the entire Ethiopia-Yemen Traps.

On the other hand, we tackled the initial question of how changes in PSV, dipole moment and polarity reversal frequency may be linked over the past 155 Myr. To this end, we provided new absolute (API) and relative (RPI) palaeointensities from the Waja section, yielding an instantaneous virtual dipole moment of (57 ± 9)×10^{21} Am^2 (1σ, N = 18) and a relative variability in intensity ε_F = 0.39 ± 0.07 (1σ, N = 19). Our analysis of the API database with strict selection criteria fails to identify any robust correlation between changes in dipole moment and reversal frequency over the past 155 Myr. Nevertheless, the available RPI results on volcanic sequences are consistent with an increase of the PSV proxy ε_F with reversal rate, as predicted by numerical dynamo simulations. We thus speculate that the absence of negative

correlation between changes in dipole moment and reversal frequency in the API database over the past 155 Myr may be the result of insufficient sampling prior to 31 Ma rather than the signature of an intrinsic geomagnetic feature.

1. Introduction

Since the invention of the compass more than 2,000 years ago, humanity has been able to observe Earth's magnetic field. These observations were not reliably recorded until the Age of Exploration 500–600 years ago, with ship captains documenting the declination (defined as the angle between the geographic and magnetic north) and latitude on a daily basis while at sea. However, the purpose of these recordings was to determine the ship's location and not to examine the geomagnetic field itself, therefore the recording of the inclination (defined as the angle between the magnetic field and the horizontal plane) was missing in the majority of cases. More comprehensive records started to be collected in Paris, London, and Munich in the mid-19th century in dedicated geomagnetic observatories, which soon gave rise to a worldwide network of geomagnetic observatories (e.g. Turner et al., 2015)

Unfortunately, a few hundred years are extremely short relative to the geologic time scale, making direct observations insufficient to understand the geomagnetic field in its entirety. This is where palaeomagnetism intervenes as the field of science specializing in extracting and interpreting the magnetic signal recorded by rocks. Palaeomagnetism has come a long way since its creation in the mid-19th century. Since its beginnings, experts have been able to document hundreds of geomagnetic polarity reversals, several prolonged periods (> 20 Myr) without polarity reversals known as superchrons, temporal palaeodirectional changes over stable polarity periods termed palaeosecular variation, as well as variations in the magnitude of the geomagnetic field (e.g. Merrill et al., 1996; Tauxe et al., 2018). With the advances in mathematical and computing tools, palaeomagnetic observations provide precious inputs for geomagnetic field models and numerical dynamo simulations, and thus a much clearer picture of the origin of the geomagnetic field.

1.1. Earth's Magnetic Field

The main source of the geomagnetic field is in the outer core, with minor contributions from external origin (e.g. the ionosphere, the magnetosphere). Earth's outer core is liquid and mainly consists of an electrically conducting alloy of iron and nickel. As a result of Earth's secular cooling, a thermal gradient is produced between the inner-core boundary (ICB) and the core-mantle boundary (CMB), which maintains convective currents in the liquid outer core, the geometry of which is largely controlled by Earth's rotation (Tauxe, 2005). The geomagnetic field and the electrically-conducting flow interact in positive feedback which causes Earth's outer core to be a self-sustaining magnetohydrodynamic dynamo, more commonly known as the geodynamo. The magnetic field vector can be described at any point on the Earth's surface through the inclination, which is the angle between the magnetic field vector and the horizontal plane, and the declination, which is the angle of the magnetic field vector with respect the geographic north, and its intensity measured in nT (Butler, 2004).

The present-day geomagnetic field, at the surface of the Earth, is approximately 90% dipolar while the other 10% is composed of multipolar components likely caused by eddy currents produced at the core mantle boundary (Butler, 2004). Taking this into account, the best approximation of the geomagnetic field is a magnetic dipole at the centre of the Earth with a tilt of 11.5° west with respect to the rotation axis, with a geomagnetic equator perpendicular to it. The geomagnetic field changes with time, and it is known to undergo geomagnetic reversals. It decreased by 5% intensity over the last few 100 years, with a westward drift of around 0.4° longitude per year. Furthermore, the magnetic poles migrate near the geographic poles in unpredictable patterns, this phenomenon along with the westward drift, the changes in declination and inclination, changes in intensity are known as secular variations (Butler, 2004). It has been shown that secular variations average out over geologic time scales. Therefore, over a few thousand years the geomagnetic field can be approximated by a dipole magnet parallel to the rotational axis giving us 90° inclination at the poles (by convention north is positive) and 0° inclination at the equator. This alignment of the dipole of the magnetic field with the rotation axis is known as the Geocentric Axial Dipole hypothesis (GAD) (Butler, 2004).

1.2. Reversals, Field Strength, and Palaeosecular Variation

The geomagnetic field is approximated over geological timescales by a geocentric axial dipole that possesses the ability to stochastically reverse its polarity (Merrill et al., 1996; Tauxe et al., 2018). Even with the existence of numerous geodynamo simulations and extensive palaeomagnetic records, the processes leading to geomagnetic reversals are still not fully understood. Making the matter more complicated, the geomagnetic field's reversal rate f_{rev}, its average strength F and its temporal variability during stable periods (termed hereafter palaeosecular variation, PSV) are highly variable throughout Earth's history, most likely as a result of changes in the thermal boundary conditions imposed by the mantle on the core (e.g. McFadden & Merrill, 1984, 2000) and/or spontaneous bifurcations of the geodynamo (e.g. Gallet & Hulot, 1997; Hulot & Gallet, 2003). Numerical dynamo simulations suggest that the variations in F negatively correlate with the variations in PSV and f_{rev}, with a coupling controlled in first approximation by the vigour of convection (e.g. Driscoll & Olson, 2009; Lhuillier & Gilder, 2013). The reality may be of course more complex for the palaeomagnetic field. How the variations of these three quantities, systematically or sporadically, correlate over the Earth's history and which proxy, given the uncertainties of palaeomagnetic records, best represents the geodynamo activity remain highly controversial issues (e.g. Doubrovine et al., 2019; Kulakov et al., 2019; Tarduno et al., 2002).

From an observational viewpoint, the changes in f_{rev} are well documented over the past 155 Myr, mostly based on the analysis of sea floor anomalies (e.g. Cande & Kent, 1995; Channell, 1995). Four 'stationary' segments, each of them being described by a Poisson process and potentially characteristic of a distinct geodynamo regime, have been identified (Gallet & Hulot, 1997; Lowrie & Kent, 2004), yielding an average f_{rev} of 4.2 Myr^{-1} for 0 – 31 Ma, 1.3 Myr^{-1} for 31 – 74 Ma, nearly zero during the Cretaceous Normal Superchron (CNS, 84 – 121 Ma) and 2.8 Myr^{-1} for 121 – 155 Ma, according to the latest version of the geomagnetic polarity timescale (GPTS; Ogg, 2020). In simple words, a Poisson process is a renewal process in which the probability of a future event does not depend on the time since the last event.

PSV is traditionally quantified by the VGP scatter S (angular standard deviation of the virtual geomagnetic poles derived from a collection of rapidly cooled,

time-independent volcanic units, e.g. Cox, 1970) with the caveat that S strongly depends on site palaeolatitude and the consequence that latitudinal profiles are needed to compare different epochs. Thirty years ago, McFadden et al. (1991) suggested a clear link between changes in S and f_{rev}, in the form of a lower equatorial value and greater latitudinal increase in S during times of low reversal frequency. Later studies confirmed the strong increase in S with latitude during the CNS (e.g. Biggin et al., 2008; Tarduno et al., 2002) whereas S may be nearly invariant with latitude during time with high f_{rev} (e.g. Biggin et al., 2008; Doubrovine et al., 2019).

Absolute palaeointensity (API) determinations also yield contradictory results over the past 155 Myr. Some studies reported API values during the CNS up to three times higher than the average value during the Cainozoic (e.g. Tarduno et al., 2001, 2002; Tauxe & Staudigel, 2004), thereby supporting an increase in F with decreasing f_{rev}, whereas other studies reported API values during the CNS indistinguishable from the average value during the Cainozoic (e.g. Granot et al., 2007; Pick & Tauxe, 1993; Prévot et al., 1990; Shcherbakova et al., 2008, 2012), questioning the existence of a clear link between variations in F and f_{rev}.

Elucidating these potential correlations naturally depends on our ability to characterize the palaeomagnetic field with reliable proxies over the past 155 Myr. An alternative PSV proxy is the relative variability ε_F in intensity, defined as the ratio of the standard deviation to the mean derived from a sequence of palaeointensity determinations (e.g. Cronin et al., 2001). Its assumed latitudinal independence makes it more suitable than S to discriminate distinct dynamo regimes from collections of rapidly cooled, time-independent volcanic units (e.g. Lhuillier & Gilder, 2013). Its determination — practically difficult with API experiments because of their low success rate — can nevertheless be accomplished with relative palaeointensity (RPI) determinations using the pseudo-Thellier method (e.g. Tauxe et al., 1995; Yu et al., 2003). RPI is used to assess past geomagnetic field strength without determining its absolute strength, it is a measure of the ancient magnetic field's strength compared to a reference value, the Pseudo-Thellier method is more commonly used on sedimentary rocks but has recently been applied to volcanic rocks (e.g. Bogue, 2018; de Groot et al., 2013, 2015). Two preliminary estimates of ε_F during the Plio-Pleistocene and CNS support a positive correlation between changes in PSV and f_{rev} (Lhuillier et al., 2016, 2017).

1.3. Large Igneous Provinces

Large Igneous Provinces (LIPs) are large deposits of intrusive and extrusive igneous rocks most of which are attributed to mantle plumes with some being attributed to divergent plate tectonics (Mahoney & Coffin, 1997). They usually result in the massive outpouring of a few million km^3 of basaltic lava over a 1–3 Myr interval (Mahoney & Coffin, 1997). These geodynamic events are thought to have notable consequences on the biosphere due to the sudden release of CO_2 and SO_2 into the atmosphere or hydrosphere (e.g. Courtillot & Renne, 2003). Most of the 12 major LIPS are linked to mass extinctions or anoxia events, such as the end of the Palaeocene associated with the North Atlantic Volcanic Province (Phase 1), the Cretaceous – Palaeogene extinction event attributed to the Deccan Traps, the end of the Pliensbachian ascribed to the Karoo and Farrar traps, the end of the Triassic attributed to the Central Atlantic Magmatic Province and the end of the Permian better known as “The Great Dying” associated with the Siberian traps.

The focus of this study is on the Ethiopia-Yemen Traps (EYT) (Figure 2.1), also known as the Afro-Arabian Flood Basalts which erupted during the Early Oligocene and could potentially be associated with the end of the early Oligocene extinction. The EYT stem from the arrival of the Afar mantle plume around 30 Ma and represent among the youngest and best-preserved LIP (Hofmann et al., 1997; Rochette et al., 1998). Four previously studied sections have produced palaeomagnetic data: the Lima-Limo section by Rochette et al. (1998) also investigated by Hofmann (1997, PhD thesis), Ahn et al. (2021) and the Belessa section by Lhuillier and Gilder (2019) sections in the north-western part of the EYT in Ethiopia; As Sarat section studied by Kellogg and Reynolds (1983) and Sanaa section studied by Riisager et al. (2005) sections in the north-eastern part of the EYT in Yemen.

1.4. Scientific Aims

To further contribute to the discussion, we decided to sample a sequence of volcanic flows in Ethiopia that reliably recorded the geomagnetic field at equatorial latitudes during the Oligocene. It was chosen to investigate a volcanic section as volcanic rocks, carrying a thermoremanent magnetization, provide discrete snapshots of Earth's magnetic field, contrary to sedimentary rocks, carrying a chemical or detrital remanent magnetization that tends to smooth out the magnetic record (Constable et al., 2016; Hellio & Gillet, 2018). Additionally, as a thermoremanent magnetization can be reproduced in laboratory conditions, volcanic rocks can potentially be used for API experiments. Another desired requirement for this study was to sample a section spanning a sufficient amount of time to adequately sample PSV. The time interval required to obtain a reliable PSV estimate is a highly debated issue since it depends on several factors such as but not limited to: geological setting, quality of rock samples and scientific aims. For volcanic rocks, an interval of at least one million years is best suited to confidently determine if the geodynamo operated in a different regime in the past (Lhuillier & Gilder, 2013).

This thesis focusses on the palaeomagnetism of the EYT, with the twofold purpose to

- better characterize the behaviour of Earth's magnetic field at equatorial latitudes during the Oligocene, and in particular to address the question of the existence of a correlation between field strength, reversal frequency and PSV;
- better constrain the emplacement history of the EYT, and in particular to try to understand the spatiotemporal variability of the eruption rate of the flood basalts.

To this end, we chose to investigate a 1 km thick volcanic section (the so-called Waja section) in the west of the EYT, the palaeomagnetism of which had not been studied before. We practically sampled a collection of 1,029 oriented core samples from 123 cooling units, with the aim of

- determining the palaeodirections (declination and inclination) of each lava flow, to provide magnetostratigraphic constraints based on the polarity and the rate of change of Earth's magnetic field;
- determining the RPI between the lava flows using the pseudo-Thellier method (e.g. Tauxe et al., 1995; Yu et al., 2003), to estimate the vigour of PSV during the Oligocene at equatorial latitudes;
- determining, whenever possible, the API using the Thellier method (Coe, 1967), to provide new estimates of the reconstructed dipole strength, and thus improve the resolution of the API database.

Furthermore, to support our palaeomagnetic interpretations, we performed microscopic observations, rock-magnetic analyses, chemical analyses of the major and trace elements as well as $^{40}Ar/^{39}Ar$ age determinations on select samples.

2. Ethiopia-Yemen Traps

2.1. Geologic Setting and Geochemistry

The Ethiopia-Yemen Traps stem from the arrival of the Afar mantle plume around 30 Ma and represent among the youngest and best-preserved LIP (Hofmann et al., 1997; Rochette et al., 1998). Geographically, the EYT are located at the junction of two oceanic rifts (Red Sea, Gulf of Aden) and the East-African continental rift, with the consequence that the original edifice has been dissected into several parts, the main part lying in Ethiopia with the rest being located in Yemen. Initially covering an area of $4–8 \cdot 10^5$ km^2 for an estimated volume of $0.6–1.2 \cdot 10^6$ km^3 (Natali et al., 2016; Rochette et al., 1998), this pile of several hundred lava flows is 2–5 times less voluminous than the Deccan and Siberian Traps but is singular in several respects.

Geochemically, the EYT is unique in that it comprises the entire range of LIP magmas from low titanium (1–3 wt% TiO_2) to high titanium (3–7 wt% TiO_2) basalts. The geochemistry of the north-western part of the EYT in Ethiopia has been studied by Pik et al. (1998, 1999) and Beccaluva et al. (2009) while the north-eastern part of the EYT in Yemen was studied by Natali et al. (2016) with extensive results for major elements (Table 2.1) and rare Earth elements (Table 2.2). In addition to this we had at our disposal geochemical data from the Belessa section (Lhuillier & Gilder, 2019) which was used extensively to compare with the Waja section.

The EYT (Figure 2.1) are zoned with High-Ti (HT) picritic basalts (HT2, TiO_2 3–7 wt%) above the inferred location of the plume head, followed by progressively Lower Ti (LT) tholeiitic basalts (HT1, TiO_2 2–4 wt% and then LT, TiO_2 1–3 wt%) toward the periphery (Beccaluva et al., 2009; Pik et al., 1998). This was further substantiated by the analysis of the rare Earth elements (Beccaluva et al., 2009; Natali et al., 2016; Pik et al., 1999) which show that HT2 basalts are of a more primitive origin while the corresponding LT basalts are characteristic of less primitive basalts and having more crustal contamination that the HT2 basalts. Beccaluva and Natali's conclusions suggest that the origins of HT2 basalts are from >75 km in depth while the LT basalts originate from a less primitive mantle source <75 km in depth.

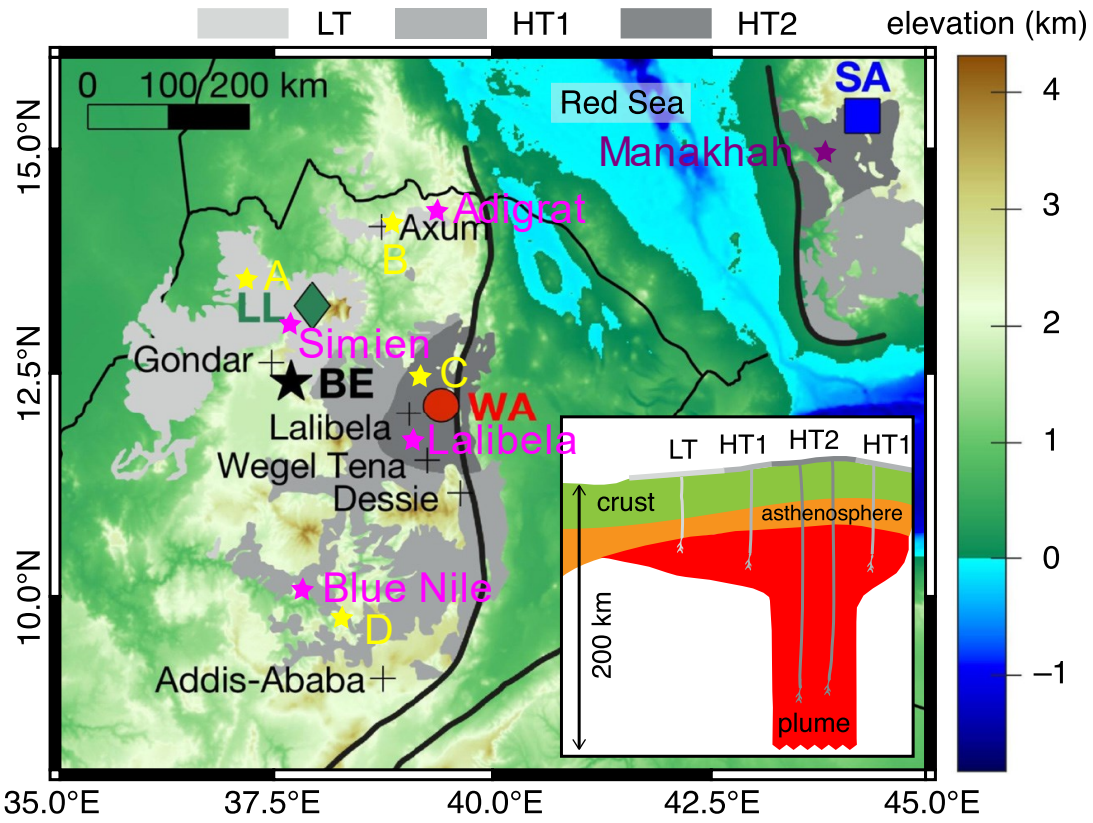

Figure 2.1: Schematic map and geodynamic interpretation of the Ethiopia-Yemen Traps (adapted from Eid et al., 2021; Natali et al., 2016). Palaeomagnetic sections are: Belessa (BE, Lhuillier & Gilder, 2019), Lima-Limo (LL, Rochette et al., 1998), Sana'a (SA, Kellogg & Reynolds, 1983) and Waja (WA, Eid et al., 2021, 2022). Sections sampled for geochemistry: A, B, C and D (Pik et al., 1998, 1999), Adigrat, Simien, Lalibela and Blue Nile (Beccaluva et al., 2009) and Manakhah (Natali et al., 2016). Gray patches indicate the spatial distribution of the basalt flows based on titanium concentrations following Pik et al. (1998): LT. TiO_2 1–3 wt%. HT1. TiO_2 2–4 wt%. and HT2. TiO_2 3–7 wt%. Thin black lines indicate country boundaries. Thick black lines delimit the Afar escarpment.

Table 2-1: Compilation of Major elements (wt%) from previous studies on the Ethiopia-Yemen Traps (Beccaluva et al., 2009; Lhuillier & Gilder, 2019; Natali et al., 2016; Pik et al., 1998).

Study	Location	Group	Sample	SiO_2	Al_2O_3	Fe_2O_3	MnO	MgO	CaO	Na_2O	K_2O	TiO_2	P_2O_5	Total	L.O.I
Lhuillier & Gilder (2019)	Belessa	LT	B02	48.48	13.04	15.03	0.21	5.17	9.71	2.7	0.39	4.15	0.54	100.04	0.52
			B06	50.22	13.71	13.72	0.21	4.58	9.18	3.16	0.48	3.53	0.486	100	0.61
			B12	48.25	16.98	10.99	0.12	2.38	7.44	3.69	0.98	2.89	0.43	99.66	5.5
			B14	47.34	16.77	11.14	0.14	2.6	7.64	3.3	1.21	2.84	0.43	99.62	6.2
			B23	43.66	14.66	14.86	0.19	6.76	10.86	2.33	0.44	4.39	0.232	100.77	2.27
			B31	45.82	13.85	13.88	0.17	7.86	11.19	2.3	0.24	2.07	0.22	100	2.19
			B32	47.13	13.56	13.01	0.17	7.7	10.25	1.98	0.92	1.99	0.178	99.94	2.85
			B46	47.96	14.71	14.38	0.18	5.61	8.05	3.04	1.03	3.38	0.407	100.42	1.53
			B50	48.82	14.61	16.26	0.13	3.53	7.76	3.4	0.74	3.29	0.441	100.30	1.14
			B56	49.06	12.42	13.43	0.11	6.95	9.16	2.23	0.71	2.36	0.243	99.74	2.79
			B58	47.56	10.69	12.97	0.18	10.81	10.41	2.42	0.46	2.27	0.262	99.43	0.85
			B62	48.13	13.3	12.2	0.15	8.04	11.03	2.27	0.72	2.29	0.232	100.42	1.9
			B63	47.83	13.46	12.49	0.17	8.02	10.76	2.3	0.77	2.39	0.25	100.49	1.9
			B68	45.95	14.32	15.03	0.2	5.69	9.31	2.74	0.77	4.31	0.299	99.33	0.61
		Phonolite	B65	56.73	21	2.71	0.27	0.22	1.64	8.75	5.97	0.4	0.059	99.45	1.51
Pik et al. (1998)	A	LT	E100	49.52	18.19	11.09	0.12	2.61	7.68	3.98	1.25	2.59	0.61	99.67	2.04
			E166	50.15	15.9	11.9	0.19	6.42	11.53	2.61	0.27	1.58	0.17	101.25	0.53
			E168	49.95	15.3	12.03	0.3	5.62	11.1	2.82	0.59	2.1	0.26	100.93	0.86
			E171	48.65	14.78	13.26	0.21	5.65	11.07	2.71	0.24	1.88	0.23	99.11	0.44
			E178	49.1	15.58	13	0.18	6.41	10.7	2.34	0.27	1.98	0.25	100.43	0.62
			E181	48.63	16.5	10.45	0.17	7.76	11.26	2.91	0.56	1.32	0.2	100.44	0.68
			E202	49.31	15.85	12.95	0.19	6.51	9.57	3.08	0.55	1.63	0.29	100.95	1.02
			E210	47.46	17.15	13.66	0.17	5.96	7.69	3.72	0.58	2.26	0.34	99.11	1.27
			E84	48.1	16.69	11.35	0.18	7.74	9.76	2.71	0.24	1.15	0.14	99.26	1.18
			E88	48.05	16.05	11.63	0.17	8.67	10.58	2.38	0.16	1.08	0.1	99.9	1.04
			E90	47.94	15.61	11.78	0.17	6.6	9.59	2.76	0.35	1.59	0.22	99.49	2.88
			E95	50.74	13.32	14.82	0.23	4.62	9.04	3.03	0.65	2.29	0.26	100.81	1.8
			E98	50.74	15.02	11.85	0.17	5.94	10.66	2.69	0.29	1.85	0.19	100.32	11.4
			PM6	51.06	15.37	12.44	0.16	5.46	10.25	2.87	0.43	1.8	0.24	99.92	0.79
	B	HT1	E215	46.1	15.36	15	0.16	5.48	6.71	4.72	0.76	3.37	0.74	99.71	1.31
			E216	46.06	14.44	13.39	0.18	9.78	8.53	3.39	0.43	2.05	0.3	100.5	1.95
		LT	E217	43.45	15	15.64	0.2	7.08	7.26	4.18	0.72	3.73	0.66	99.29	1.37
			E218	47.43	16.46	13.59	0.19	6.17	8.39	3	0.48	2.26	0.3	99.94	1.17

Table 2-1: Continued (1)

Study	Location	Group	Sample	SiO_2	Al_2O_3	Fe_2O_3	MnO	MgO	CaO	Na_2O	K_2O	TiO_2	P_2O_5	Total	L.O.I
Pik et al. (1998)	A	HT1	E235	48.33	13.96	13.54	0.19	5.44	9.4	2.9	0.83	2.69	0.41	99.14	1.45
			E236	48.11	13.79	13.35	0.19	6.26	11.02	2.59	0.36	2.45	0.22	99.99	1.65
	C (middle)	HT2	E225	48.27	9.57	13.1	0.18	13.51	10.1	1.84	0.41	2.62	0.28	100.63	0.75
			E226	44.99	8.11	13.79	0.18	15.97	8.68	1.48	0.96	3.77	0.44	100.29	1.92
			E232	46.15	9.78	13.1	0.19	10	9.53	3.25	1.21	4.39	0.57	99.85	1.68
			E31	46.02	7.88	13.46	0.18	14.71	9.01	1.67	0.86	4.02	0.47	99.13	1.89
			E33	46.8	9.95	14.67	0.2	10.6	9.81	2.2	0.72	4.28	0.43	99.97	1.52
			E35	46.92	11.49	14.07	0.19	7.05	10.35	2.46	0.77	4.62	0.51	99.21	1.94
			E37	46.69	10.9	14.66	0.18	6.84	9.91	2.48	1.11	4.99	0.59	100.12	2.71
			E38	47.49	9.38	12.81	0.17	13.61	8.81	1.9	1.13	3.79	0.45	100.4	1.66
			E40	45.95	7.67	13.74	0.18	16.1	9.22	1.55	0.43	3.92	0.4	99.08	1.05
	C (top)	HT1	E223	51	15.44	10.34	0.16	4.86	9.58	3.23	0.87	2.48	0.3	100.69	2.43
			E228	49	14.43	12.47	0.18	5.42	9	3.21	1.16	3.5	0.55	100.1	1.18
			E230	50.57	14.79	11.29	0.16	4.48	9.28	2.88	1.02	3.07	0.37	99.31	1.41
			E24	48.69	12.85	15.14	0.22	4.91	9.6	2.95	0.59	3.26	0.46	99.43	1.79
			E43	48.1	13.17	15.83	0.22	5.25	9.1	3.1	0.72	3.8	0.52	100.39	1.81
			E44	48.01	12.96	14.98	0.21	5.35	9.38	2.83	0.81	3.84	0.53	99.21	1.53
			PM39	49.89	13.98	13.09	0.16	4.46	8.08	3.36	1.11	4.15	0.6	99.28	1.39
	D	HT1	E54	50.33	13.82	13.68	0.25	4.9	8.49	3.3	0.84	3.45	0.85	100.72	1.9
			E59	49.85	14.38	13.3	0.2	5.45	10.32	2.63	0.66	3.06	0.31	101.12	1.95
			E66	50.68	12.46	14.84	0.2	4.33	8.61	2.52	10.3	3.99	0.44	100.74	1.64
			E70	54.62	14.2	13.54	0.22	5.1	8.84	3.16	0.89	3.39	0.89	100.03	1.18
Beccaluva et al. (2009)	Simien	LT	SIM2	50.09	14.62	14.81	0.2	3.77	8.51	3.47	0.86	3.31	0.36	-	0
			SIM7	49.55	17.19	10.78	0.13	5.41	10.82	2.57	0.33	1.7	0.16	-	1.36
			SIM15	47.16	15.38	10.78	0.16	9.23	10.33	2.47	0.33	1.33	0.18	-	2.64
			SIM17	49.36	16.18	11.97	0.16	7.38	9.75	2.63	0.38	1.52	0.23	-	0.44
	Adigrat	LT	ADG3	45.1	15.34	12.55	0.14	12.13	8.4	1.5	0.27	1.45	0.2	-	2.93
		HT1	ADG4	44.99	16.63	12.04	0.16	10.44	9.96	1.83	0.17	1.31	0.17	-	2.3
			ADG6	48.52	17.59	10.96	0.16	7.38	9.91	2.78	0.21	1.48	0.2	-	0.82
			ADG7	42.2	12.85	18.05	0.16	8.42	6.72	3.28	0.6	4.77	0.69	-	2.28
			ADG8	41.87	12.78	17.84	0.16	9.27	6.56	3.39	0.63	4.68	0.63	-	2.19
	BlueNile	HT1	BLN2	49.94	13	13.62	0.22	5.14	9.64	3	0.69	3.23	0.84	-	0.67
			BLN4	48.67	14.62	14.64	0.17	5.29	10.15	2.39	0.72	3.09	0.2	-	0.04
	Lalibela	HT1	LAL20	49.82	13.28	14.59	0.21	4.58	9.11	3.13	1.02	3.51	0.75	-	0

Table 2-1: Continued (2)

Study	Location	Group	Sample	SiO_2	Al_2O_3	Fe_2O_3	MnO	MgO	CaO	Na_2O	K_2O	TiO_2	P_2O_5	Total	L.O.I
Beccaluva et al. (2009)	Simien	HT2	LAL1	47.52	8.05	12.76	0.17	10.32	11.68	2	1.3	5.44	0.61	-	0.16
			LAL3	50.02	10.99	13.05	0.17	8.08	9.74	2.4	1.27	3.92	0.36	-	0
			LAL5	46.02	8.59	13.39	0.19	13	10.03	1.89	0.96	4.51	0.41	-	1
			LAL6	45.1	8.3	13.94	0.18	16.2	9.25	1.73	0.74	4.02	0.4	-	0.16
			LAL9	46.25	8.76	14.07	0.18	14.41	10.28	1.53	0.79	3.44	0.29	-	0
			LAL11	44.22	6.19	11.61	0.17	25.1	6.1	0.56	0.87	3.02	0.35	-	1.82
			LAL14	45.64	7.78	15.04	0.17	11.97	9.83	1.95	1.17	5.91	0.52	-	0.02
			LAL15	45.23	9.22	15.06	0.19	9.27	10.32	2.91	1.17	5.5	0.49	-	0.64
			LAL18	50.15	13.46	14.32	0.18	4.85	8.7	2.86	1.2	3.87	0.41	-	0
			LAL19	49.91	13.38	14.41	0.19	5	8.93	2.85	0.96	4.01	0.36	-	0
Natali et al. (2016)	Lalibela	HT2	LAL5	46.57	8.69	1.61	0.2	13.16	10.15	1.92	0.97	4.57	0.41	-	1.01
			LAL6	45.66	8.4	1.68	0.18	16.4	9.37	1.75	0.75	4.07	0.4	-	0.16
			LAL9	46.83	8.87	1.69	0.18	14.59	10.41	1.55	0.8	3.49	0.29	-	0
			LAL33	47.79	8.99	1.77	0.18	13.39	9.58	1.65	0.57	3.61	0.4	-	0.3
			LAL41	48.15	8.3	1.68	0.18	14.89	9.97	1.53	0.54	3.09	0.3	-	0.16
			LAL45	45.77	8.62	1.85	0.18	14.64	9.15	1.63	1.1	3.86	0.46	-	0.42
			LAL47	46.26	7.79	1.84	0.17	16.04	8.74	1.44	0.89	3.93	0.44	-	0.17
			LAL70	44.52	6.02	1.9	0.18	21.21	7.79	0.98	0.98	3.34	0.39	-	0
			LAL73	44.36	6.87	1.96	0.18	17.7	8.89	1.1	0.57	3.53	0.25	-	1.51
			LAL1	48.06	8.14	1.53	0.17	10.43	11.81	2.02	1.31	5.5	0.61	-	0.16
			LAL3	50.6	11.12	1.57	0.17	8.17	9.85	2.43	1.28	3.97	0.36	-	0
			LAL14	46.26	7.88	1.81	0.17	12.13	9.96	1.98	1.18	5.99	0.53	-	0.02
			LAL15	45.84	9.34	1.81	0.19	9.4	10.46	2.95	1.19	5.57	0.5	-	0.65
			LAL31	48.55	9.22	1.68	0.18	12.92	9.2	1.84	1.01	3.44	0.53	-	0.2
			LAL42	48.14	9.57	1.74	0.17	12.06	9.57	1.69	0.85	3.76	0.37	-	0.45
			LAL43	45.64	7.95	1.93	0.17	12.44	9.94	1.53	1.19	5.09	0.63	-	0.63
			LAL43	45.64	7.95	1.93	0.17	12.44	9.94	1.53	1.19	5.09	0.63	-	0.63
			LAL44	45.41	8.35	1.91	0.16	11.83	9.35	1.88	1.27	5.13	0.55	-	1.4
			LAL60	47.21	8.51	1.88	0.17	10.24	10.19	2.15	1.16	4.85	0.48	-	0.62
			LAL65	45.8	8.1	1.85	0.16	12.78	9.26	2.11	1.17	4.48	0.52	-	1.46
			LAL69	45.75	7.48	1.83	0.17	13.22	10.48	1.87	0.96	4.68	0.5	-	0.85
			LAL72	48.12	8.87	1.77	0.17	9.84	10.62	1.84	1.2	4.44	0.55	-	0.8
			LAL76	48.92	9.99	1.7	0.17	10.61	9.97	2.06	1.09	3.69	0.49	-	0
	Manakhah	HT2	YE26	42.22	9.98	1.61	0.2	16.21	9.98	1.74	0.47	3.31	0.31	-	3.21
			YE29	40.93	9.9	1.74	0.19	16.98	10.38	1.74	0.81	3.21	0.43	-	2.09
			YE23	37.86	9.55	2.11	0.23	12.3	13.93	1.32	0.2	4.16	0.46	-	3.77

Table 2-1: Continued (3)

Study	Location	Group	Sample	SiO_2	Al_2O_3	Fe_2O_3	MnO	MgO	CaO	Na_2O	K_2O	TiO_2	P_2O_5	Total	L.O.I
Natali et al. (2016)	Manakhah	HT2	YE24	39.2	13.25	1.93	0.21	9.46	11.49	3.81	0.76	4.46	0.6	-	1.98
			YE25	41.2	11.2	1.85	0.2	11.34	13.1	2.2	0.12	3.52	0.47	-	2.42
			YE27	38.15	11.76	2.31	0.21	6.77	13	2.8	0.92	5.07	0.54	-	3.05
			YE28	40.31	12.1	2.22	0.2	7.96	12.31	2.26	0.85	4.69	0.47	-	1.84
			YE31	40.98	12.33	1.62	0.17	11.93	12.48	1.81	1.13	3.52	0.71	-	2.52

Table 2-2: Compilation of Rare Earth Elements (ppm) from studies on the EYT (Beccaluva et al., 2009; Lhuillier & Gilder, 2019; Natali et al., 2016; Pik et al., 1999)

Study	Location	Group	Sample	La	Ce	Pr	Nd	Sm	Eu	Gd	Tb	Dy	Ho	Er	Tm	Yb	Lu
Lhuillier & Gilder (2019)	Belessa	LT	B02	20	46.3	6.56	30.1	7.15	2.56	7.92	1.17	6.32	1.18	3.2	0.41	2.25	0.35
			B06	22.7	52.6	7.24	32.8	7.98	2.73	8.28	1.24	6.74	1.24	3.36	0.41	2.68	0.38
			B31	10.9	27.5	3.46	15.9	4.05	1.4	4.46	0.71	4.13	0.79	2.14	0.28	1.73	0.25
			B32	11.2	25.1	3.57	16.2	4.25	1.45	4.58	0.72	3.97	0.79	2.21	0.29	1.72	0.25
			B58	13.9	31.3	4.58	18.4	4.43	1.52	4.61	0.72	3.9	0.72	1.83	0.24	1.45	0.22
			B62	15.1	32.2	4.33	18.8	4.41	1.47	4.54	0.69	3.8	0.72	1.9	0.25	1.55	0.21
Pik et al. (1999)	A	LT	E100	23.1	58.7	8.2	38.7	9.2	3.2	9.8	1.5	8.5	1.62	4.1	0.56	3.6	0.54
			E166	7.9	18.5	2.7	13.5	3.76	1.32	4.3	0.7	4.44	0.88	2.55	0.351	2.2	0.341
			E168	11.9	27.1	3.8	18.7	5.15	1.67	5.93	0.96	6.11	1.24	3.64	0.497	3.2	0.492
			E171	7.8	19.2	2.9	14.8	4.41	1.56	5.31	0.85	5.5	1.12	3.14	0.437	2.72	0.443
			E178	13.4	24.4	3.6	17.6	4.69	1.64	5.35	0.84	5.23	1	2.87	0.378	2.3	0.364
			E181	9.4	18.2	2.5	11.6	3	1.14	3.82	0.63	4.03	0.85	2.44	0.36	2.36	0.355
			E202	10.1	24.8	3.6	17.3	4.46	1.58	5.17	0.79	4.85	0.98	2.63	0.368	2.37	0.354
			E210	8.8	24.9	3.8	19.7	5.22	1.92	5.92	0.89	5.45	1.08	2.82	0.403	2.41	0.389
			E84	4.7	12.5	1.9	9.8	2.9	1.1	3.7	0.64	4	0.83	2.3	0.33	2.1	0.33
			E88	2.9	8.2	1.3	7.2	2.4	1	3.3	0.56	3.6	0.75	2	0.29	1.9	0.29
			E90	9.3	23	3.4	15.9	4.1	1.5	5	0.8	4.9	0.97	2.6	0.36	2.3	0.35
			E95	13.4	33.6	4.8	23.2	6.1	2.1	8	1.31	8.1	1.64	4.4	0.62	3.9	0.6
			E98	8.2	21.5	3.1	15.2	4.2	1.6	5.4	0.92	5.6	1.12	2.9	0.4	2.5	0.38
			PM6	8.7	21.5	3.1	15	4.07	1.45	4.85	0.76	4.78	0.96	2.61	0.36	2.2	0.335
	B	HT1	E215	20.2	57.3	8.6	41.2	9.26	3.15	8.46	1.09	5.24	0.81	1.71	0.189	1.02	0.13
			E216	5.5	18.7	3.3	17.4	4.96	1.81	5.53	0.82	4.96	0.94	2.58	0.345	2.25	0.329
	B	LT	E217	18.9	54.1	8.3	40.1	9.46	3.22	8.93	1.17	6.3	1.09	2.61	0.327	1.88	0.261
			E218	8.6	24.5	3.9	19.8	5.3	1.96	6.08	0.92	5.72	1.12	3.04	0.425	2.75	0.412
	C (bottom)	HT1	E235	32.8	69.4	8.5	34.8	7.09	2.22	6.99	0.99	5.74	1.08	2.84	0.386	2.35	0.355
			E236	13	32.2	4.5	21.6	5.89	1.95	7.05	1.09	6.69	1.34	3.59	0.489	2.96	0.467
	C (middle)	HT2	E225	17.9	40.7	5.6	25.7	6.15	1.99	6.55	0.94	5.34	0.97	2.5	0.322	1.97	0.291
			E226	26.7	65.5	8.9	40.4	9.15	2.82	9.01	1.21	6.64	1.14	2.78	0.35	1.92	0.286
			E232	37.1	87.8	11.6	51.9	11.36	3.5	10.72	1.4	7.4	1.28	3.06	0.378	2.08	0.303
			E31	29.9	71.8	9.5	41.9	9.47	2.77	8.43	1.17	6	1.06	2.53	0.321	1.84	0.26
			E33	31	70	9.7	44	9.6	3	9.3	1.4	7.2	1.29	3.1	0.4	2.4	0.35
			E35	37	87	11.6	52	11.1	3.5	10.7	1.5	8.2	1.46	3.5	0.45	2.7	0.39
			E37	43.9	103.6	13.2	57.3	12.3	3.6	10.8	1.46	7.55	1.32	3.21	0.41	2.4	0.34
			E38	27.1	65	8.8	38.3	8.54	2.56	7.94	1.1	5.93	1.07	2.62	0.33	1.98	0.27

Table 2-2: Continued (1)

Study	Location	Group	Sample	La	Ce	Pr	Nd	Sm	Eu	Gd	Tb	Dy	Ho	Er	Tm	Yb	Lu
Pik et al. (1999)	C(middle)	HT2	E40	27.9	67.9	9.1	42.2	9.3	2.9	8.8	1.2	6.4	1.11	2.7	0.34	2	0.3
	C (top)	HT1	E223	23.8	54.9	7.1	30.1	6.67	2.15	6.69	0.97	5.67	1.07	2.84	0.386	2.28	0.355
			E228	28.5	68.5	9.1	40.3	8.89	2.98	8.94	1.27	7.17	1.33	3.41	0.451	2.72	0.403
			E230	26.2	61.5	8	35.5	8	2.5	8.02	1.12	6.37	1.18	3.04	0.404	2.43	0.373
			E24	25.7	61	7.9	34	8.4	2.55	8.82	1.38	8.38	1.7	4.57	0.64	4.01	0.6
			E43	18.5	44.9	6.2	28.8	6.61	2.54	6.59	0.96	5.47	1.07	2.75	0.37	2.29	0.33
			E44	18.9	45.6	6.3	28.9	6.71	2.56	6.64	0.98	5.55	1.06	2.77	0.37	2.29	0.33
			PM39	37.6	87.4	11.2	49.3	10.75	3.34	10.58	1.49	8.47	1.55	3.9	0.516	2.97	0.451
	D	HT1	E54	27	66	9.1	45	9.7	3.7	9.8	1.4	7.5	1.38	3.5	0.45	2.8	0.42
			E59	18.8	46.4	6.1	27	6.51	2.1	6.39	0.98	5.41	1.01	2.52	0.34	2.01	0.28
			E66	29	71	9.3	43	9.9	3.2	10.3	1.6	8.7	1.59	4.1	0.54	3.3	0.49
			E70	27	65.5	9.2	45	10.1	4	10.3	1.4	7.8	1.42	3.6	0.47	2.9	0.44
Beccaluva et al. (2009)	Simien	LT	SIM2	18	41.5	5.67	28.2	6.85	2.35	7.36	1.49	7.82	1.58	4.27	0.57	3.77	0.51
			SIM7	8.86	23.1	3.23	15.3	4.12	1.43	4.97	0.83	4.88	0.96	2.7	0.36	2.18	0.3
			SIM15	6.05	14.9	2.25	11.3	3.02	1.3	2.85	0.62	3.42	0.68	1.94	0.28	1.76	0.26
			SIM17	9.91	23	3.24	16.1	3.52	1.57	3.87	0.86	4.41	0.84	2.34	0.33	2.14	0.28
	Adigrat	LT	ADG3	5.95	15.2	2.51	12.6	3.43	1.36	3.18	0.66	3.87	0.75	2.23	0.32	2.08	0.26
			ADG4	4	12.4	2.09	11.5	3.75	1.39	4.56	0.79	4.8	0.97	2.81	0.38	2.36	0.34
			ADG6	4.05	14.3	1.79	8.98	2.43	0.82	2.78	0.46	2.67	0.53	1.48	0.2	1.18	0.16
		HT1	ADG7	20.7	54.4	8.73	44.9	11.1	3.39	8.32	1.26	5.59	0.78	1.81	0.18	1.07	0.15
			ADG8	18.8	49.5	7.98	40.4	9.48	3.01	7.66	1.18	5.29	0.7	1.65	0.19	0.91	0.14
	BlueNile	HT1	BLN2	27.4	61.8	8.94	44.9	9.36	3.68	8.87	1.33	6.92	1.19	3.3	0.43	2.62	0.37
			BLN4	22.2	50.4	6.72	32	7.36	2.3	6.59	1.1	5.73	1.05	2.87	0.34	2.32	0.35
	Lalibela	HT1	LAL20	26	63.3	8.49	39.7	8.76	3	8.47	1.44	6.57	1.33	3.32	0.51	2.84	0.42
		HT2	LAL1	47.5	113	15.2	68.9	15.3	4.45	14.6	1.95	9.46	1.59	4.01	0.47	2.64	0.34
			LAL3	37.7	80.5	10.7	45.1	9.64	2.79	9.52	1.31	6.62	1.17	3.06	0.38	2.19	0.29
			LAL5	36	81.4	11.04	51.1	10.8	3.03	8.83	1.37	6.81	1.08	2.8	0.34	2.06	0.24
			LAL6	28.3	65.9	8.8	41.2	8.58	2.53	7.01	1.1	5.47	0.88	2.27	0.27	1.63	0.23
			LAL9	60.8	58.3	7.57	33.9	7.63	2.27	7.65	1.07	5.47	0.97	2.51	0.31	1.79	0.24
			LAL11	22.8	53	6.84	33.3	6.51	2.24	6.04	1	4.83	0.73	2	0.26	1.43	0.2
			LAL14	49	115	16.2	79.9	17	4.8	14	2.12	10.3	1.65	4.29	0.46	2.94	0.39
			LAL15	61.2	142	18.2	77.6	15.5	4.5	14.5	1.85	8.87	1.5	3.79	0.44	2.5	0.33
			LAL18	37.2	86	11	48.1	10.3	3.02	9.92	1.67	7.45	1.46	3.58	0.54	2.97	0.43
			LAL19	46.4	107	13.7	60.2	13	3.83	12.5	2.13	9.44	1.86	4.56	0.7	3.77	0.55
			LAL5	33.2	74.5	11	43.5	9.3	3.05	8.73	1.4	6.23	1.11	2.4	0.38	1.84	0.26
			LAL6	26.1	60.3	8.8	35	7.4	2.55	6.93	1.13	5	0.9	1.94	0.3	1.46	0.25

Table 2-2: Continued (2)

Study	Location	Group	Sample	La	Ce	Pr	Nd	Sm	Eu	Gd	Tb	Dy	Ho	Er	Tm	Yb	Lu
Natali et al. (2016)	Lalibela	HT2	LAL9	35	58.3	7.57	33.9	7.63	2.27	7.65	1.07	5.47	0.97	2.51	0.31	1.79	0.24
			LAL33	30.8	74	10.3	45	10	2.98	8.94	1.49	6.63	1.25	2.97	0.42	2.36	0.33
			LAL41	34	79.6	11.3	49.7	11.6	3.48	10.3	1.78	8.11	1.54	3.68	0.52	2.93	0.41
			LAL45	27.3	62.7	9.5	42	9.5	3.05	10.8	1.44	5.57	1.01	2.61	0.33	2.03	0.26
			LAL47	25.7	61.5	9.2	40.9	9.1	2.69	8.15	1.29	5.37	1.02	2.39	0.32	1.83	0.24
			LAL70	20.4	46.7	6.6	28.7	6.3	1.9	5.52	0.91	3.68	0.68	1.54	0.24	1.14	0.18
			LAL73	20.8	47.1	6.3	26.4	5.7	1.74	5.18	0.87	3.61	0.69	1.59	0.25	1.22	0.19
			LAL1	47.5	113	15.2	68.9	15.3	4.45	14.6	1.95	9.46	1.59	4.01	0.47	2.64	0.34
			LAL3	37.7	80.5	10.7	45.1	9.64	2.79	9.52	1.31	6.62	1.17	3.06	0.38	2.19	0.29
			LAL14	45.2	105	16.2	68	14.7	4.83	13.8	2.18	9.43	1.69	3.68	0.52	2.63	0.42
			LAL15	61.2	142	18.2	77.6	15.5	4.5	14.5	1.85	8.87	1.5	3.79	0.44	2.5	0.33
			LAL31	57.5	142	19.2	83.5	18.6	5.47	16.4	2.72	12.1	2.29	5.44	0.77	4.3	0.6
			LAL42	40	94.4	13.2	57.2	12.9	3.81	11.1	1.91	8.51	1.6	3.8	0.54	3.01	0.42
			LAL43	67.4	161	22.9	101	23	6.64	19.3	3.2	13.9	2.54	5.87	0.81	4.39	0.61
			LAL43	67.4	161	22.9	101	23	6.64	19.3	3.2	13.9	2.54	5.87	0.81	4.39	0.61
			LAL44	49.2	117	16.4	72.7	16.1	4.66	13.1	2.16	9.23	1.67	3.85	0.52	2.81	0.38
			LAL60	39	90.2	12.3	51.4	10.3	2.89	7.91	1.26	5.3	0.95	2.21	0.31	1.68	0.24
			LAL65	30.7	75	10.5	46.2	10.5	3.13	9.27	1.56	6.34	1.19	2.64	0.42	1.97	0.31
			LAL69	31.2	78.9	10.8	46.7	10.1	2.96	8.72	1.43	5.74	1.06	2.36	0.36	1.71	0.27
			LAL72	34.5	80.4	11.4	50.1	11.2	3.44	9.61	1.64	6.64	1.24	2.77	0.45	2.09	0.34
			LAL76	23.3	57.7	8.2	35.7	7.96	2.49	7.86	1.24	5.01	0.96	2.25	0.36	1.77	0.28
	Manakhah	HT2	YE26	32.8	72.7	8.74	35.9	6.84	2.12	6.66	0.85	4.09	0.71	1.91	0.23	1.36	0.18
			YE29	46.2	105	12.7	52.4	9.94	3.01	9.62	1.23	5.81	0.99	2.54	0.29	1.71	0.22
			YE23	51.2	112	13.1	51.9	9.17	2.73	8.86	1.06	4.84	0.81	2.12	0.24	1.41	0.18
			YE24	50.4	116	14.3	58.5	11	3.3	10.8	1.39	6.77	1.19	3.21	0.39	2.37	0.32
			YE25	30.1	69.6	8.52	36.2	6.96	2.13	6.74	0.85	4.08	0.71	1.89	0.23	1.34	0.18
			YE27	58.7	130	15.7	64.1	12	3.58	11.6	1.45	6.88	1.19	3.12	0.37	2.16	0.29
			YE28	46.8	104	12.5	51.4	9.66	2.93	9.49	1.2	5.76	1	2.67	0.32	1.93	0.26
			YE31	40.5	91.6	11	45.3	8.35	2.57	7.99	0.98	4.57	0.78	2.06	0.24	1.43	0.19

2.2. Age and Duration of Volcanism

The north-western part of the EYT in Ethiopia has been radioisotopically dated by Hofmann et al. (1997), Rochette et al. (1998), Ukstins et al. (2002) and Coulié et al. (2003) (Table 2.4) while the north-eastern part of the EYT in Yemen has been radioisotopically dated by Baker et al. (1996) and Riisager et al. (2005) (Table 2.5). Hofmann et al. (1997), Rochette et al. (1998) and Ukstins et al. (2002) used an Hb3gr (1,072 Ma) hornblende standard; Coulié et al. (2003) used an HD-B1 (24.2 Ma) biotite standard; Baker et al. (1996) used an MMhb-1 (520.4 Ma) hornblende standard and Riisager et al. (2005) used a Fish Canyon sanidine (28.02 Ma) standard, while all of them used the decay constant of Steiger and Jäger (1977) for determining the isotopic age of their samples.

In order to be able to analyse the compiled dates together, all of them required to be recalculated to the same standard and decay constant. The compiled dates were recalculated with respect to the Fish Canyon Tuff sanidine age of Rivera et al. (2011) using the decay constants of Min et al. (2000). The compiled results (Figure 2.2) confirm that the EYT was emplaced in a 1–2 Myr interval 29–31 Ma.

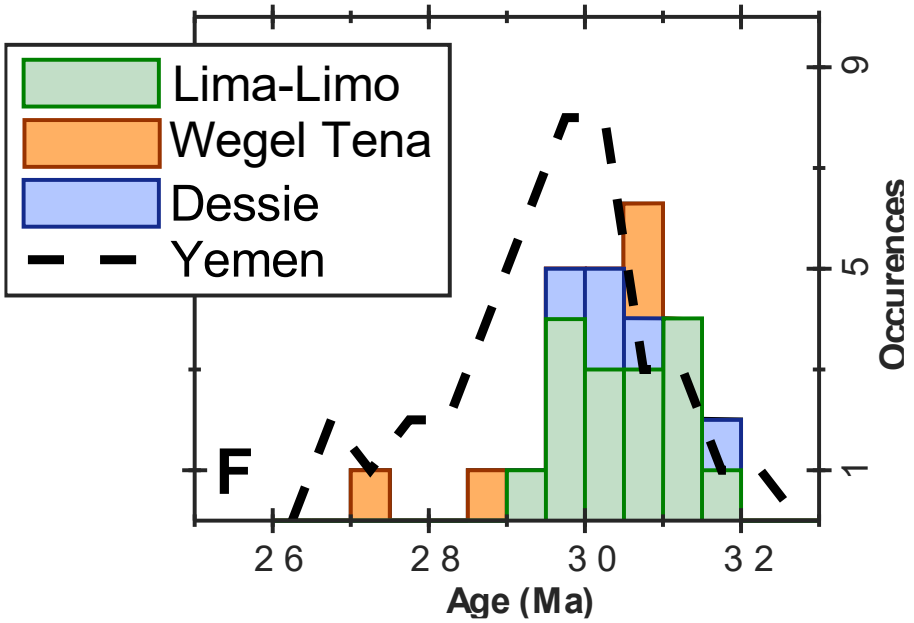

Figure 2.2: Compilation of $^{40}Ar/^{39}Ar$ ages for Ethiopia (data from Coulié et al., 2003; Hofmann et al., 1997; Rochette et al., 1998; Ukstins et al., 2002) and Yemen (Baker et al., 1996; Riisager et al., 2005, Table 2.3) recalculated to a Fish Canyon Tuff sanidine age of 28.172 ± 0.028 Ma (Rivera et al., 2011) and using the decay constants of Min et al. (Min et al., 2000).

Table 2-3: Compilation of $^{39}Ar/^{40}Ar$ ages from previous studies done on samples from **Ethiopia**. Recalculation was performed with respect to the Fish Canyon Tuff sanidine age of Rivera et al. (2011) using the decay constants of Min et al. (2000).

Study	Section	Site	Sample type	Original Data				Recalculated Data	
				Age (Ma)	σ (Myr)	Standard	Decay Constant	Age (Ma)	σ (Myr)
Hofmann et al. (1997)	Lima-Limo	E192	Feldspar/Sanidine	30.70	0.26	Hb3gr (1,072 Ma)	Steiger & Jäger (1977)	31.31	0.27
		PM26	Plagioclase	29.40	1.10			29.98	1.12
		E100		29.60	0.30			30.19	0.31
		E199		31.10	0.60			31.72	0.61
		E86		30.50	1.00			31.11	1.02
		PM29	Whole Rock	30.00	0.10			30.60	0.10
		PM6		30.00	0.30			30.60	0.31
		E98		28.70	0.69			29.27	0.70
		E203		30.40	0.40			31.00	0.41
		E84		30.80	0.40			31.41	0.41
	Adigrat	E216	Whole Rock	30.40	0.40			31.00	0.41
	Wegel Tena	PM37	Whole Rock	26.70	0.10			27.23	0.10
		PM35	Sanidine	28.20	0.14			28.76	0.14
		PM31		30.20	0.10			30.80	0.10
	Chinese Road	E41	Sanidine	29.55	0.23			30.14	0.24
		E34		29.30	0.20			29.88	0.20
Rochette et al. (1999)	Lima-Limo	LLA	Sanidine	30.10	0.10	Hb3gr (1,072 Ma)	Steiger & Jäger (1977)	30.55	0.10
		LLC		29.70	0.05			30.15	0.05
	Wegel Tena	WT31	Sanidine	30.20	0.10			30.66	0.10
Ukstins et al. (2002)	Dessie-Bati	EEWB1	Phlogopite	30.92	0.11	Hb3gr (1,072 Ma)	Steiger & Jäger (1977)	31.53	0.11
		EIU99035	Sanidine	30.16	0.13			30.76	0.13
		EIU99029		29.61	0.12			30.20	0.12
		EEWB7		29.43	0.12			30.02	0.12
		EEWB20	Whole Rock	29.34	0.15			29.92	0.15
		EEWB22	Plagioclase	25.10	0.20			25.60	0.20
		EEWB9		25.00	0.20			25.50	0.20
Coulié et al. (2003)	Lima-Limo	VC97-01	K-Feldspar	29.76	0.30	HD-B1 (24.2 Ma)	Steiger & Jäger (1977)	29.92	0.30
		VC97-02		29.81	0.30			29.97	0.30
		98EH150		29.62	0.30			29.78	0.30
		98EH163		29.84	0.30			30.00	0.30
	Digdiga	80X	K-Feldspar	30.07	0.30			30.23	0.30

Table 2-4: Compilation of $^{39}Ar/^{40}Ar$ ages from previous studies done on samples from **Yemen**. Recalculation was performed with respect to the Fish Canyon Tuff sanidine age of Rivera et al. (2011) using the decay constants of Min et al. (2000).

Study	Section	Site	Sample type	Original Data				Recalculated Data	
				Age (Ma)	σ (Myr)	Standard	Decay Constant	Age (Ma)	σ (Myr)
Baker et al. (1996)	NE Sana'a	JB148	Plagioclase	29.23	0.28	MMhb-1 (520.4 Ma)	Steiger & Jäger (1977)	29.56	0.28
		JB163	Anorthoclase	28.55	0.16			28.88	0.16
		JB177	Amphibole	19.74	0.60			19.96	0.61
		JB171	Whole Rock	28.50	0.10			28.82	0.10
		JB186		26.60	0.40			26.90	0.40
		JB191		27.70	0.40			28.02	0.40
	Sana'a	JB284	Whole Rock	27.60	0.40			27.91	0.40
		JB281		29.80	0.70			30.14	0.71
		JB335		28.90	0.20			29.23	0.20
		JB279	Plagioclase	29.85	0.18			30.19	0.18
		JB261		29.65	0.64			29.99	0.65
		JB276	Anorthoclase	29.13	0.13			29.46	0.13
		JB326		29.06	0.22			29.39	0.22
	10 Km West Sana'a	JB216	Anorthoclase	29.34	0.12			29.67	0.12
		JB221		28.21	0.10			28.53	0.10
		JB228II	Sanidine	28.18	0.14			28.50	0.14
		JB232		27.75	0.10			28.07	0.10
		JB227II		26.94	0.20			27.25	0.20
	South Sana'a	JB133	Anorthoclase	29.02	0.10			29.35	0.10
		JB124	Whole Rock	30.52	0.10			30.87	0.10
		JB136		28.70	0.20			29.03	0.20
	SW Yemen	J14B	Biotite/Amphibole	29.37	0.34			29.70	0.35
		J40	Plagioclase	28.97	0.18			29.30	0.18
		J56	Anorthoclase	26.51	0.12			26.81	0.12
	Shibam-Kawkaban	MNY221	Whole Rock	29.60	0.20			29.94	0.20
	Saihan	MNY401	Whole Rock	30.14	0.14			30.48	0.14
	Al Rebat	MNY354	Whole Rock	31.40	0.40			31.76	0.40
	Murais	MNY388	Whole Rock	30.69	0.14			31.04	0.14
	Al Khorg	MNY357	Whole Rock	31.76	0.10			32.12	0.10
	At Turbah	MNY355	Whole Rock	31.07	0.10			31.42	0.10
		J73	Plagioclase	30.71	0.26			31.06	0.26
	Wadi Zaydan	MNY200	Amphibole	30.44	0.27			30.79	0.27

Table 2-4: Continued

Study	Section	Site	Sample type	Original Data				Recalculated Data	
				Age (Ma)	σ (Myr)	Standard	Decay Constant	Age (Ma)	σ (Myr)
Riisager et al. (2005)	Bayt Mawjan	BM6	Ignimbrite	27.67	0.12	FCs (28.02 Ma)	Steiger & Jäger (1977)	27.82	0.12
	Bayt Baws	BB1	Lava	29.61	0.08			29.77	0.08
		BB5	Tuff	29.59	0.12			29.75	0.12
		BB7		29.48	0.13			29.64	0.13
	Jabal Shahirah	JS6	Lava	29.94	0.24			30.10	0.24
	Shibam-Kawkaban	SK1	Lava	30.24	0.18			30.40	0.18
		SK4		30.20	0.26			30.36	0.26
		SK6		30.51	0.36			30.68	0.36
		SK7		30.03	0.26			30.19	0.26
		SK10		30.30	0.14			30.46	0.14

2.3. Palaeomagnetism

From the 1980s, palaeodirectional investigations have been performed on the EYT. Four extensively studied sections are worth mentioning: **Lima-Limo** (Ahn et al., 2021; Hofmann et al., 1997, PhD thesis; Rochette et al., 1998) and **Belessa** (Lhuillier & Gilder, 2019) sections in the north-western part of the EYT in Ethiopia and **As Sarat** (Kellogg & Reynolds, 1983) and **Sanaa** (Riisager et al., 2005) sections in the north-eastern part of the EYT in Yemen (Table 2.5). Each of these studies added comprehensive datasets for the purposes of studying the PSV during the Oligocene (Figure 2.3). The directions were recentred around their principal axe (Tauxe & Kent, 2004; Lhuillier & Gilder, 2013) in order to negate the differences due to tectonic displacement between the African and Arabian plates. The Belessa and Lima-Limo sections proved useful to this contribution for correlating the north-western part of the EYT in Ethiopia with the Geomagnetic Polarity Time Scale (GPTS, Ogg, 2020) (Figure 2.4).

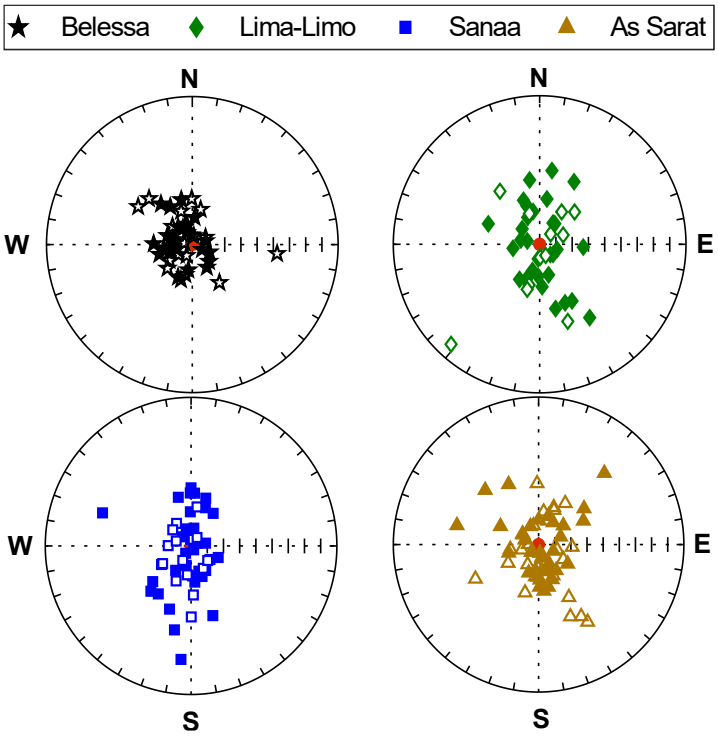

Figure 2.3: Recentred directions with respect to the section-level Fisher's mean (Tauxe & Kent, 2004) from Belessa (Lhuillier & Gilder, 2019), Lima-Limo (Rochette et al., 1998), Sanaa (Riisager et al., 2005), and As Sarat (Kellogg & Reynolds, 1983) sections.

Radioisotopic dating coupled with magnetostratigraphy point to an emplacement of the EYT over a 1–2 Myr interval (from chron C11r.2r to chron C11r.1r or C10r), leading to an average extrusion rate of 0.3–1.2 km^3/yr (Natali et al., 2016; Rochette et al., 1998), lower than the values for the Siberian Traps (~1.5 km^3/yr) and the Deccan Traps (~3.0 km^3/yr; Courtillot & Renne, 2003). Partial mismatches in the magnetostratigraphy of the continuous sections of Lima-Limo and Belessa, both located in the LT area of the North Ethiopian plateau (Figure 2.4), however suggest possible spatiotemporal variability of the extrusion rate by at least a factor two (Lhuillier & Gilder, 2019), with possible consequences on the amplitude of the climatic forcing produced by the release of aerosols into the atmosphere.

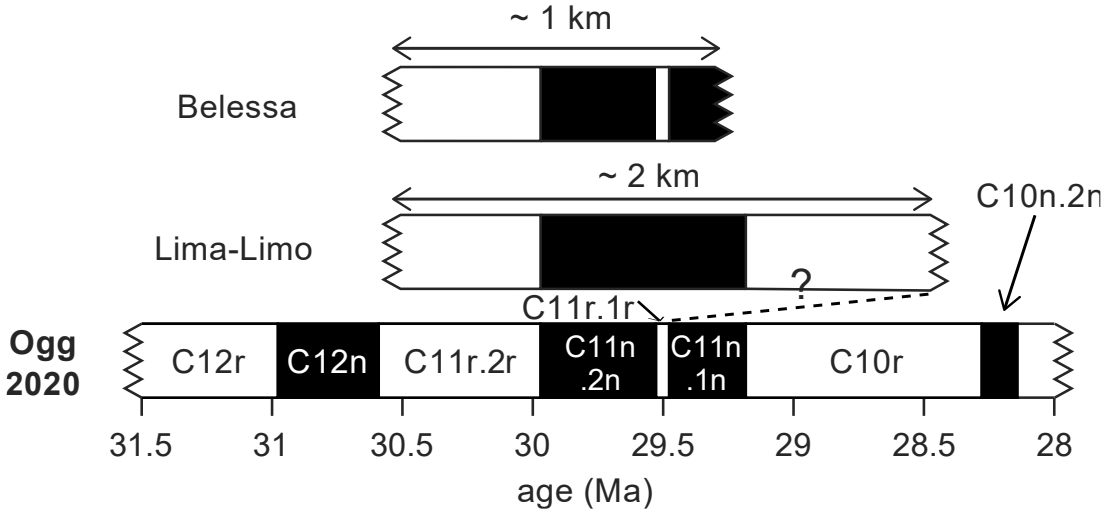

Figure 2.4: Tentative match of the Belessa (Lhuillier & Gilder, 2019) and Lima-Limo (Rochette et al., 1998) sections with the geomagnetic polarity time scale (Ogg, 2020).

Table 2-5: Palaeomagnetic directions from the Ethiopia – Yemen Traps (Kellogg & Reynolds, 1983; Lhuillier & Gilder, 2019; Riisager et al., 2005; Rochette et al., 1998). The quantity (n) is the number of samples used in determining, site Latitude and Longitude (Slat & Slon) the Declination (D) and Inclination (I) with (k) as the precision parameter and (α95) as the 95% confidence. Sites marked with (*) were merged into directional groups, sites marked with (†) recorded excursional directions.

Study	Section	Site	n	Slat (°)	Slon (°)	*D* (°)	*I* (°)	*k*	*α95* (°)
Kellogg et al. (1983)	As Sarat	K103	4	18.15	43.43	-3.4	19.7	70	8.4
		K104	6	18.15	43.43	33.5	-27.9	4	28.5
		K105	5	18.15	43.43	-10.6	16.8	107	6.1
		K106	1	18.15	43.43	-2.6	38.3	-	-
		K107	5	18.15	43.43	-12.5	28.1	24	12.8
		K108	1	18.15	43.43	-4.5	19.8	-	-
		K109	3	18.15	43.43	4.6	26.6	225	5.9
		K110	2	18.15	43.43	-52.8	-1	-	-
		K111	1	18.15	43.43	2.2	16	-	-
		K112	3	18.15	43.43	-23.7	16.6	149	6.6
		SA22	3	18.15	43.43	0.3	36	21	27.3
		SA23	3	18.15	43.43	-36.9	-18.3	24	25.6
		SA24	5	18.15	43.43	174.9	-46.7	4	45.7
		SA27	4	18.15	43.43	175.5	5	40	14.7
		K92	3	18.18	43.17	11.3	22.6	391	4.1
		K94	3	18.18	43.17	-4.1	26.9	264	5
		K95	3	18.18	43.17	-8.1	27.2	50	11.4
		K96	3	18.18	43.17	0.1	23.1	251	5.1
		K97	3	18.18	43.17	-27.6	1.9	258	5
		K98	3	18.18	43.17	7.5	1.9	276	4.9
		K99	3	18.18	43.17	6.1	8.1	685	3.1
		K100	3	18.18	43.17	-1.3	27.4	67	9.9
		K101	4	18.18	43.17	-5.6	36.1	395	3.5
		K102	1	18.18	43.17	183.2	-18.3	-	-
		K102Q	2	18.18	43.17	183.3	-9.6	-	-
		K36	3	28.06	43.17	19.1	-8	9	26.3
		K37	3	28.06	43.17	0.8	25.1	107	7.8
		K38	3	28.06	43.17	2.5	31.7	26	5
		K39	3	28.06	43.17	-6.8	30.5	83	8.9
		K40	2	28.06	43.17	-5.4	32.1	-	-

Table 2-5: Continued (1)

Study	Section	Site	n	Slat (°)	Slon (°)	*D* (°)	*I* (°)	*k*	*α95* (°)
Kellogg et al. (1983)		K41	3	28.06	43.17	-1.1	26.9	409	4
		K42	3	28.06	43.17	143.7	31.1	49	11.6
		K43	3	28.06	43.17	154.8	27.9	12	23.6
		K44	3	28.06	43.17	148.3	27.9	40	12.8
		K45	3	28.06	43.17	156.6	16.9	28	15.4
		K46	3	28.06	43.17	159.9	-4.2	83	8.9
		K47	3	28.06	43.17	165.7	4.6	100	8.1
		K48	3	28.06	43.17	168.2	-25.6	97	8.2
		K49	3	28.06	43.17	174.4	-0.4	194	5.8
		K50	3	28.06	43.17	179.7	-12.7	56	10.8
		K51	3	28.06	43.17	18.7	-1.3	82	8.9
		K52	1	28.06	43.17	154.6	-10.6	-	-
		K53	3	28.06	43.17	181.3	14.1	114	7.6
		K54	3	28.06	43.17	163.2	-9.6	357	4.3
		K55	2	28.06	43.17	209.3	7.8	-	-
		K56	1	28.06	43.17	-23.5	-21.1	-	-
	As Sarat	K179	3	17.89	43.29	1.8	0.4	78	9.2
		K180	2	17.89	43.29	167.2	-28.2	-	-
		K78	2	17.89	43.29	-5.5	17.3	-	-
		K79	2	17.89	43.29	-14	9.9	-	-
		K80	5	17.89	43.29	-15	7.1	283	2.6
		K81	3	17.89	43.29	-10.8	2.6	47	11.8
		K82	3	17.89	43.29	-6.2	-1	79	9.1
		K83	2	17.89	43.29	-0.7	-3.4	-	-
		K84	3	17.89	43.29	155.9	-34.7	299	4.7
		K85	3	17.89	43.29	163.8	-31.4	988	2.6
		K86	5	17.89	43.29	163.8	-32.9	166	4.9
		K86A	4	17.89	43.29	170.5	-30.7	217	4.8
		K87A	3	17.89	43.29	176.8	-23.1	15	21.1
		K88A	2	17.89	43.29	189.8	-9.6	-	-
		K89A	3	17.89	43.29	190.7	-2	351	4.3
		K90A	3	17.89	43.29	179.8	-1.6	259	5
		K91A	2	17.89	43.29	173.9	0.4	-	-

Table 2-5: Continued (2)

Study	Section	Site	n	Slat (°)	Slon (°)	*D* (°)	*I* (°)	*k*	*α95* (°)
Rochette et al. (1998)	Lima-Limo	LL24	7	13.25	37.93	191,4	-8,8	88	6,5
		LL23	6	13.25	37.93	199,4	34,4	149	5,5
		LL22	7	13.25	37.93	193,6	37,9	197	4,3
		LL21A	7	13.25	37.93	350,1	-20	188	5,6
		LL21B	3	13.25	37.93	168,1	4,5	1000	2,7
		LL20	5	13.25	37.93	191,1	-38,6	91	8,1
		LL18	7	13.25	37.93	154	-8,7	12	18,1
		LL17	7	13.25	37.93	190,4	-9,2	153	4,9
		LL16	8	13.25	37.93	184,4	25,7	291	3,3
		LL15	9	13.25	37.93	203,7	33,1	32	9,3
		LL14	6	13.25	37.93	173,5	-21,7	95	6,9
		LL54	11	13.25	37.93	182,1	10,4	97	4,6
		LL25	5	13.25	37.93	75,1	46,3	48	11,2
		LL55	9	13.25	37.93	192,6	5,2	18	12,4
		LL56	9	13.25	37.93	2,6	4,7	83	5,7
		LL13	5	13.25	37.93	349,8	-7,4	268	4,7
		LL12	6	13.25	37.93	8,9	-19,2	41	10,6
		LL57	4	13.25	37.93	9	19,9	564	3,9
		LL11	8	13.25	37.93	343,8	40,2	102	5,5
		LL58	14	13.25	37.93	28	-30,8	39	6,4
		LL09	4	13.25	37.93	359,6	3,7	203	6,9
		LL61	5	13.25	37.93	342,5	-19,7	54	10,5
		LL60	8	13.25	37.93	10,2	22,3	58	7,3
		LL59	6	13.25	37.93	356,8	-8	131	5,9
		LL10	5	13.25	37.93	188,9	8	219	5,2
		LL62	4	13.25	37.93	190,4	7,9	127	8,2
		LL08	7	13.25	37.93	175,6	-18,6	382	3,1
		LL07	6	13.25	37.93	188,1	19,1	278	4
		LL06	6	13.25	37.93	176,6	-33,2	284	4
		LL05	8	13.25	37.93	218,5	41,2	214	3,8
		LL04	7	13.25	37.93	172,5	0	507	2,7
		LL03	8	13.25	37.93	176,1	0,6	71	6,6
		LL63	9	13.25	37.93	204,5	-31,8	57	6,9
		LL02	7	13.25	37.93	178,8	16,8	57	8,1
		LL01	8	13.25	37.93	171,1	21,5	84	6,1
		LL30	5	13.25	37.93	175	21,6	253	4,8

Table 2-5: Continued (3)

Study	Section	Site	n	Slat (°)	Slon (°)	*D* (°)	*I* (°)	*k*	*α95* (°)
Rochette et al. (1998)	Lima-Limo	LL29	5	13.25	37.93	182,1	20	72	9,1
		LL26	9	13.25	37.93	179,2	-15,5	222	3,5
		LL27	7	13.25	37.93	176,2	-12,3	456	2,8
		LL28	6	13.25	37.93	173,2	-6	455	3,1
		LL64	5	13.25	37.93	207,3	3,7	114	7,2
	Wegel-Tena	WT49	20	11.61	39.21	324,7	-0,2	53	4,5
		WT53	8	11.61	39.21	357,5	0,7	84	6,1
		WT52	5	11.61	39.21	6,2	6,9	191	4,9
		WT51	11	11.61	39.21	346,9	13,8	3,9	26,4
		WT50	11	11.61	39.21	7,2	18,1	53	4,5
		WT47	9	11.61	39.21	358,9	-14,7	206	3,6
		WT48	13	11.61	39.21	169	-14,2	344	2,2
		WT46	13	11.61	39.21	186,7	-20,1	66	5,1
		WT40	8	11.61	39.21	183,7	-27,2	185	4,1
		WT45	10	11.61	39.21	188,8	-7,6	59	6,4
		WT39	8	11.61	39.21	180,5	-6,1	255	3,5
		WT31	15	11.61	39.21	168,3	64	91	5,4
		WT44	14	11.61	39.21	184,3	-21,1	126	3,6
		WT32	8	11.61	39.21	174,4	-34	121	5
		WT43	9	11.61	39.21	348,6	2,6	12,6	15,1
		WT33	4	11.61	39.21	6,6	-6,3	68	11,2
		WT34	8	11.61	39.21	6,4	0,9	105	5,4
		WT42	6	11.61	39.21	354,3	0,1	9	23,6
		WT38	13	11.61	39.21	177,8	28,3	153	3,4
		WT35	8	11.61	39.21	190,5	46,5	44	8,5
		WT36	9	11.61	39.21	337,3	18,5	3,2	34
		WT41	12	11.61	39.21	337,9	-4,6	185	3,2
		WT37	4	11.61	39.21	354,1	26,7	39	15
Riisager et al. (2005)	Escarpment	Esc1	6	15,17	43,97	181,3	12	87,2	7,2
		Esc2	6	15,17	43,94	173,9	15	228,8	4,4
		Esc3	6	15,17	43,94	150,8	17,9	59,2	8,8
		Esc4*	17	15,18	43,94	348	4,2	164,3	2,8
		Esc5*	7	15,16	43,95	6,4	-6,3	510,1	2,7
		Esc6*	8	15,16	43,95	4,2	-1,5	223,1	3,7
		Esc7	3	15,16	43,95	164,3	11,9	231,3	8,1

Table 2-5: Continued (4)

Study	Section	Site	n	Slat (°)	Slon (°)	*D* (°)	*I* (°)	*k*	*α95* (°)
Riisager et al. (2005)	Escarpment	Esc8	6	15,16	43,95	172,5	-30,6	381,4	3,4
		Esc9	5	15,16	43,94	351,6	28,4	88,1	8,2
		Esc10*	6	15,15	43,95	26,6	18,1	476,7	3,1
	Bayt Mawaj	BM1	4	15,2	43,98	170,3	9,2	200,5	6,5
		BM2	7	15,2	43,98	159,3	33,4	310,2	3,4
		BM3	7	15,2	43,98	153,4	24,7	462,7	2,8
		BM4	3	15,2	43,98	174,5	0,7	249,8	7,8
		BM5	6	15,2	43,98	173	-33,5	545,4	2,9
		BM6*	5	15,2	43,98	351,2	9,4	38,4	12,5
	Sect. A	A1*	8	15,29	44,07	3,3	0,7	142,8	4,7
		A2*	7	15,28	44,08	0,9	-3,9	263	3,7
	Bayt Baws	BB3*	4	15,27	44,2	6,8	-7,7	179,5	6,9
		BB4*	14	15,27	44,2	345,8	-9,8	85	4,3
		BB5*	4	15,27	44,2	355,5	19	53,3	12,7
		BB6*	38	15,27	44,2	3,7	-0,8	83	2,6
	Jabal Shahirah	JS1	4	15,4	44,14	149,1	23,1	537,6	4
		JS2	6	15,4	44,14	179,3	15,3	344,6	3,6
		JS3	7	15,4	44,14	188,2	4,9	82,4	6,7
		JS4	8	15,4	44,14	181,1	-2,9	245,5	3,5
		JS6	7	15,4	44,14	176,6	-2,8	29,8	11,2
		JS7*	15	15,38	44,14	175,6	-11	192,4	2,8
		JS8*	7	15,38	44,14	176,8	-9	367,5	3,2
		JS9	2	15,38	44,14	1,8	20,5	-	-
		JS10	5	15,38	44,14	349,6	-20	170,4	5,9
		JS11	6	15,38	44,14	352,9	40,9	81,4	7,5
		JS12	3	15,38	44,14	346,1	13,6	78,4	14
		JS13*	6	15,38	44,14	6,4	-2,4	93,8	7
		JS14*	3	15,38	44,14	352,8	10,9	193,1	8,9
		JS15*	9	15,38	44,14	1,3	1	367,4	2,7
		JS16*	8	15,38	44,14	357,1	-0,6	95,3	5,7
	Shibam Kawakabam	SK1†	8	15,42	44,09	120	-17,1	100,2	5,6
		SK2	6	15,41	44,11	185,9	-19,1	344,3	3,6
		SK4†	4	15,42	44,09	162,3	63,8	247,7	5,8
		SK5*	7	15,42	44,09	178,6	10,8	664,5	2,3
		SK6*	6	15,42	44,09	172,1	-11,6	128,8	5,9

Table 2-5: Continued (5)

Study	Section	Site	n	Slat (°)	Slon (°)	*D* (°)	*I* (°)	*k*	*α95* (°)
Riisager et al. (2005)	Shibam Kawakabam	SK7*	5	15,42	44,1	166,7	-8,4	28,9	14,5
		SK8	8	15,42	44,1	355,2	17,2	130,3	4,9
		SK9	4	15,42	44,1	156,4	8,7	48,8	13,3
		SK10	7	15,42	44,1	170,3	-10,7	31,3	10,9
	Wadi Dhar	WD1	5	15,43	44,12	165,2	-28,1	160,5	6,1
		WD2	9	15,43	44,12	175,2	18,4	40,1	8,2
		WD3	5	15,43	44,12	175,2	-30,5	84	8,4
		WD4	6	15,43	44,12	172,6	-20,1	465,4	3,1
		WD5	6	15,41	44,12	172,8	-5	501,9	3
		WD6	12	15,41	44,12	170	2,6	175,6	3,3
		WD7	6	15,41	44,12	168,3	-6,4	596,4	2,7
		WD8	8	15,41	44,11	183,6	6	266,7	3,4
		WD9	6	15,41	44,11	182	-27,6	342,1	3,6
		WD10	7	15,41	44,11	181,5	-22,3	1331,3	1,7
		WD11*	5	15,41	44,11	175,5	14,7	342,9	4,1
	Jabal Kura'a	JK1*	6	15,49	44,42	168,5	-4,1	303,8	3,9
		JK2	7	15,49	44,42	1,2	-10,9	139,2	5,1
		JK3*	7	15,49	44,42	358,6	-11,5	525,7	2,6
		JK4*	11	15,49	44,42	346,3	-3,8	98,1	4,6
		JK5*	5	15,49	44,42	18,6	2,3	103,4	7,6
		JK6*	13	15,49	44,42	354,7	0,6	30	7,7
		JK7	5	15,48	44,42	160,9	45,5	476,3	3,5
		JK8	9	15,48	44,42	343,7	9,3	15	13,7
		JK9	9	15,48	44,42	351,9	-2,2	151	4,2
		JK10	5	15,48	44,42	357,7	9,3	64,7	9,6
		JK12	12	15,48	44,42	187,4	37,1	26,5	8,6
		JK13*	9	15,48	44,42	7,5	5,9	8,5	18,8

Cooling Unit	n	Sites	D (°)	I (°)	k	α95 (°)
CU 1 lava	12	SK5, WD11	177,4	12,4	344,4	2,3
CU 2 lava	21	JS7, SK6	174,6	-11,1	167,4	2,5
Jabal Kura'a lava	18	JS8, SK7, JK1	171,2	-7,2	72,1	4,1
Jabal Kura'a ignimbrite	17	BB3, JS13, JK3	3,3	-7,4	99,9	3,6
Escarpment ignimbrite	53	Esc4, A1, BB4, JS14, JK4	349,7	-3,2	57,9	2,6
Green tuff	25	Esc5, BB5, JS15, JK5	5,8	1,2	36,8	4,8
SAM ignimbrite	74	Esc6, A2, BB6, JS16, JK6	1,3	-1,3	62,9	2,1
Bayt Mawjan ignimbrite	20	Esc10, BM6, JK13	9,1	10,9	11,7	10

Table 2-5: Continued (6)

Study	Section	Site	n	Slat (°)	Slon (°)	*D* (°)	*I* (°)	*k*	*α95* (°)
Lhuillier & Gilder (2019)	Belessa	B01†	5	12.45	37.78	21.9	−19.1	92	8.0
		B02	8	12.45	37.78	176.3	−11.5	139	4.7
		B03	6	12.45	37.78	157.4	−27.9	304	3.8
		B04*	5	12.45	37.78	171.4	−33.0	615	3.1
		B05*	5	12.45	37.78	168.4	−28.7	76	8.8
		B04–05	10	-	-	169.9	−30.9	132	4.2
		B06	8	12.45	37.78	168.7	−15.7	157	4.4
		B07	8	12.45	37.78	186.1	3.1	429	2.7
		B08	8	12.45	37.78	186.4	−2.0	253	3.5
		B09*	7	12.45	37.78	166.6	−7.8	197	4.3
		B10*	8	12.45	37.77	166.0	−8.4	160	4.4
		B09–10	15	-	-	166.3	−8.1	187	2.8
		B11	8	12.45	37.77	155.1	−6.2	143	4.6
		B12*	8	12.48	37.76	182.6	−5.0	269	3.4
		B13*	6	12.44	37.76	181.7	−1.3	105	6.6
		B12–13	14	-	-	182.2	−3.4	160	3.2
		B14	8	12.44	37.76	184.4	−8.1	348	3.0
		B15*	8	12.45	37.76	178.9	−20.6	1026	1.7
		B16*	8	12.45	37.76	177.5	−21.5	1140	1.6
		B15–16	16	-	-	178.2	−21.1	1044	1.1
		B17	8	12.45	37.76	167.9	−3.6	307	3.2
		B18	9	12.45	37.76	173.7	−12.7	175	3.9
		B19	8	12.45	37.76	163.3	−26.7	171	4.3
		B20*	8	12.44	37.73	163.7	−12.4	361	2.9
		B21*	9	12.44	37.73	162.0	−9.5	294	3.0
		B20–21	17	-	-	162.8	−10.9	299	2.1
		B22*	9	12.44	37.73	163.2	−4.4	297	3.0
		B23*	6	12.44	37.73	166.0	0.3	112	6.4
		B22–23	15	-	-	164.3	−2.5	159	3.0
		B24	8	12.44	37.73	158.5	−0.6	208	3.8
		B25*	5	12.44	37.73	174.5	7.5	184	5.7
		B26*	7	12.45	37.73	174.7	7.9	437	2.9
		B25–26	12	-	-	174.6	7.7	309	2.5
		B27	8	12.45	37.73	184.9	6.3	161	4.4
		B28	7	12.45	37.73	2.1	−2.8	315	3.4
		B29	8	12.45	37.73	349.5	2.2	852	1.9

Table 2-5: Continued (7)

Study	Section	Site	n	Slat (°)	Slon (°)	*D* (°)	*I* (°)	*k*	*α95* (°)
Lhuillier & Gilder (2019)	Belessa	B30	8	12.45	37.72	12.8	8.3	774	2.0
		B31	9	12.45	37.72	4.6	11.6	2023	1.1
		B32	7	12.45	37.72	9.9	14.6	921	2.0
		B33*	4	12.45	37.72	0.2	28.0	164	7.2
		B34*	8	12.45	37.72	7.0	24.9	80	6.2
		B35*	5	12.45	37.72	1.4	24.0	569	3.2
		B33–35	17	-	-	3.8	25.4	115	3.3
		B37	9	12.45	37.72	3.2	−12.2	828	1.8
		B41	8	12.45	37.71	1.0	22.6	98	5.6
		B44	8	12.45	37.70	1.2	−3.3	123	5.0
		B45	8	12.45	37.70	0.2	12.1	71	6.6
		B46	7	12.45	37.70	168.9	11.7	171	4.6
		B47	6	12.45	37.70	161.0	−3.0	198	4.8
		B48	8	12.45	37.70	173.7	−17.3	625	2.2
		B50	7	12.45	37.70	11.4	18.9	402	3.0
		B51†	8	12.45	37.70	27.9	−14.8	397	2.8
		B52	8	12.45	37.70	7.9	−3.8	654	2.2
		B53	6	12.45	37.70	6.0	4.7	1453	1.8
		B54	8	12.45	37.70	352.2	−13.2	249	3.5
		B55*	8	12.45	37.70	355.6	2.1	208	3.8
		B56*	8	12.45	37.70	356.5	0.5	437	2.7
		B55–56	16	-	-	356.0	1.3	291	2.2
		B57*	8	12.45	37.70	0.3	4.8	494	2.5
		B58*	7	12.45	37.70	2.3	5.9	1223	1.7
		B57–58	15	-	-	1.3	5.3	634	1.5
		B61	8	12.45	37.70	357.2	−19.2	788	2.0
		B62	8	12.45	37.70	10.8	7.8	531	2.4
		B69	6	12.44	37.66	340.2	26.7	90	7.1
		B68†	6	12.44	37.66	307.6	8.6	125	6.0
		B67	8	12.45	37.66	8.0	3.4	843	1.9

2.4. Palaeointensities

Three studies already reported API determinations from the Early Oligocene Ethiopian Traps, the API results with at least two determinations per cooling unit were compiled (Figure 2.4 and Table 2.3). Riisager et al. (1999) reported API results using Thellier–Thellier experiments which involves replacing a specimen's NRM in progressive stages with partial TRMs in a known laboratory field B_{lab}. Lhuillier et al. (2019a) reported API results using Thellier-Coe experiments which is a refined version of the Thellier-Thellier method that adds additional steps to address limitations and improve the reliability of API determinations. Yoshimura et al. (2020) recently reported API results using the Tsunakawa–Shaw method which aims to minimize the effects of heating on the reliability of the final API results, this involves demagnetizing the sample using alternating field methods then applying a TRM in a known B_{lab}.

For the Lima-Limo section (chrons C11r.2r to C11n.1r or C10r; Ahn et al., 2021; Coulié et al., 2003; Rochette et al., 1998), Riisager et al. (1999) reported API results from six lava flows, yielding an average intensity of 23.7 ± 9.3 (1σ) μT (VDM = 57 ± 24 [1σ] ZAm^2, N = 17). For the same section, Yoshimura et al. (2020) recently reported results from eleven lava flows, yielding an average intensity of 16.2 ± 8.0 (1σ) μT (VADM = 42 ± 21 [1σ] ZAm^2, N = 30). For the Belessa section (chrons C11r.2r to C11n.1n, (Lhuillier & Gilder, 2019), Lhuillier et al. (2019a) reported results from five lava flows, yielding a mean intensity of 12.0 ± 3.0 (1σ) μT (VDM = 30 ± 8 [1σ] ZAm^2, N = 48). In comparison, the present-day magnetic field at Lalibela was computed using the IGRF-12 model (Thébault et al., 2015), resulting in 36 μT.

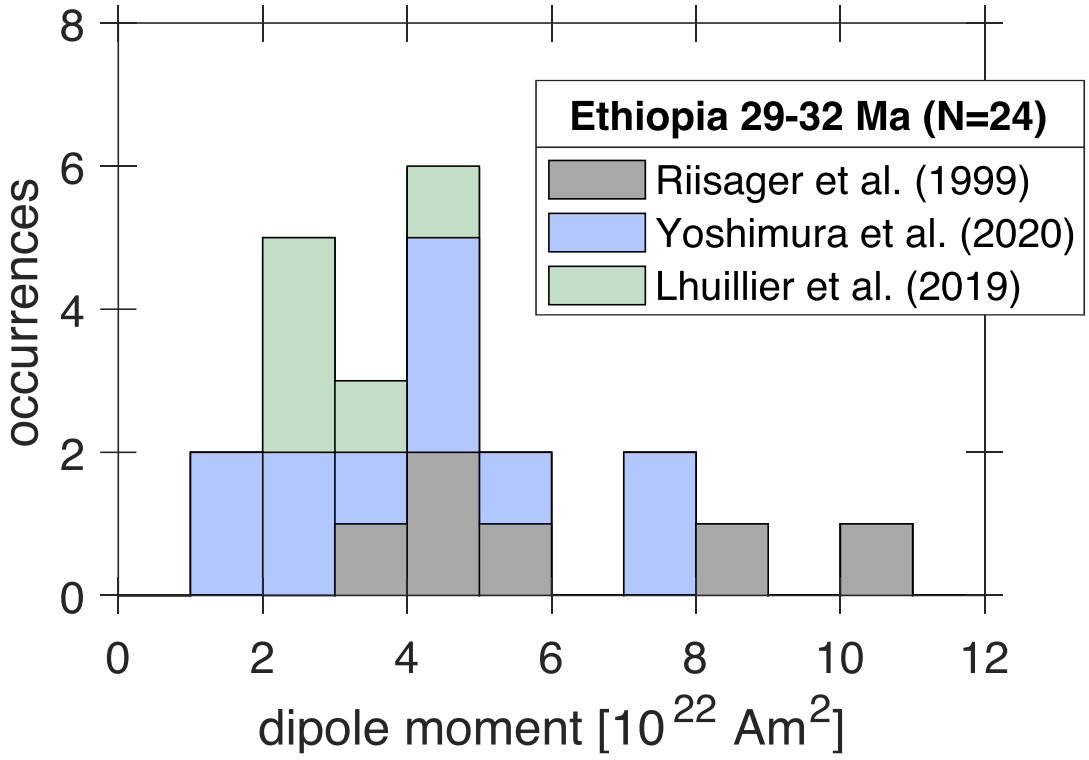

Figure 2.3: Histogram of dipole moments from the Ethiopian Traps (29 – 32 Ma) (adapted from Eid et al., 2021) without applying selection criteria except a minimum of two determinations per cooling unit.

Table 2-6: Compilation of published flow-mean absolute palaeointensities from Ethiopia Yemen Traps results from the Lima-Limo section (Riisager et al., 1999; Yoshimura et al., 2020) and Belessa section (Lhuillier et al., 2019a): site latitude and longitude (Slat & Slon) polarity (Pole; Normal or Reverse) number n of samples used to determine the palaeointensity B_{anc} with standard deviation $\sigma(B_{anc})$; virtual dipole moment (VDM) provided with its standard deviation σ(VDM); virtual axial dipole moment (VADM) provided with its standard deviation σ(VADM).

Study	Section	Site	n	Slat (°)	Slon (°)	Pole	B_{anc}	σ (B_{anc})	VDM	σ (VDM)	VADM	σ (VADM)
Riisager et al. (1999)	Lima-Limo	LL5	2	13.25	37.93	R	14.2	3.3	3	0.7	-	-
		LL8	3	13.25	37.93	R	17.3	1.3	4.3	0.3	-	-
		LL16	2	13.25	37.93	R	19.7	3.8	4.7	0.9	-	-
		LL17	3	13.25	37.93	R	39.2	4.4	10	1.1	-	-
		LL19	2	13.25	37.93	R	35.4	1.4	8.6	0.3	-	-
		LL23	3	13.25	37.93	R	24.9	4	5.6	0.9	-	-
Lhuillier et al. (2019a)	Belessa	B31	7	12.45	37.72	N	11.8	1.8	3	0.5	-	-
		B32	10	12.45	37.72	N	11.3	1.8	2.8	0.4	-	-
		B50	12	12.45	37.70	N	10	2.7	2.5	0.7	-	-
		B56	10	12.45	37.70	N	17.1	1.2	4.4	0.3	-	-
		B58	9	12.45	37.70	N	9.6	1.6	2.5	0.4	-	-
Yoshimura et al. (2020)	Lima-Limo	A2-04	3	13.19	37.89	R	9.8	0.7	-	-	2.5	0.19
		A2-19	3	13.21	37.89	R	27.7	3.2	-	-	7.2	0.82
		A2-49	3	13.26	37.89	N	8.5	0.4	-	-	2.2	0.1
		A2-59	4	13.26	37.88	N	7.5	0.5	-	-	1.9	0.13
		A2-61b	2	13.27	37.88	N	22.8	0.5	-	-	5.9	0.13
		A3-04	2	13.27	37.88	R	5.7	0.5	-	-	1.5	0.12
		A3-07a	4	13.28	37.88	R	12.4	1.5	-	-	3.2	0.38
		A3-10	2	13.28	37.88	R	19.1	2.4	-	-	4.9	0.62
		A3-21	3	13.29	37.86	R	18.3	2.0	-	-	4.7	0.51
		A3-24	2	13.32	37.86	R	28.2	0.5	-	-	7.3	0.13
		A3-25	2	13.34	37.88	R	18.3	0.7	-	-	4.7	0.18

3. Geology and Geochronology

3.1. Sampling

The field location was chosen in the western part of the North Ethiopian plateau (represented in the Maychew area Geologic maps by Tadesse et al., 2011). The area comprises approximately two kilometres of Early Oligocene flood basalts capped by 500–800 m of Early Miocene shield volcanism (Tadesse et al., 2011). The Early Oligocene basalts are separated into three distinctive formations while the Early Miocene comprises one formation:

1) The Ashangi formation (also labelled as Tab, Tadesse et al. 2011) is the oldest Oligocene volcanic formation in the area, it comprises flood basalts that are greyish black in colour with minor tuffs. The formation is tilted with no clear bedding, severely weathered and is heavily dissected by dykes, it is exposed between the elevations of 1,500–2,450 m.
2) The Aiba basalts (also labelled as Taib, Tadesse et al. 2011) are the second Early Oligocene formation and they unconformably overly the Ashangi formation from 2,450–2,700 m. It consists of horizontally layered flood basalts that vary from greyish black to reddish brown in colour, it is also heavily cut by dykes and weathered but less so than the Ashangi formation.
3) The Alaje formation (also labelled as Talb, Tadesse et al. 2011) is the final Early Oligocene formation and it conformably overlies the Aiba basalts from 2,700–3,500 m. It contains horizontally layered dark grey to greyish black and slightly weathered basic and acidic rocks. It is penetrated by dykes as well, however much less than the previous formations.
4) The Termaber-Gussa formation (also labelled as Ttb, Tadesse et al. 2011) is the youngest volcanic formation in the area, which is Early Miocene in age and overlies the Alaje formation from 3,500–4,100 m. It is formed of horizontally layered dark grey, coarse-grained basalts which are connected to the volcanic centre. The formation is much less weathered, and the flows are much thicker than the previous formations.

Note that the concept of “formation” is debated for the Ethiopian Traps as the three Oligocene formations are barely indistinguishable in the field. The presence of

a well pronounced baked contact was the only characteristic that could reliably be used in conjunction with the geologic map for us to be able to know which formation we were sampling. Furthermore, there are minor petrological differences that were pointed at by Tadesse et al. (2011) to describe the Oligocene formations. The presence of an unconformity clearly identifies the end of the Ashangi formation while the boundary between the Aiba basalts and the Alaje formation is less distinguishable, and it could be argued that both together define only one formation. It is also worth noting the high number of dykes in the area which, in combination with the sampled area being located near the centre of the EYT, the high titanium content and primitive composition of the basalts; all points to the possibility that the sampled location was above the Afar plume axis at the time of eruption.

After two days of field reconnaissance, we decided to sample two key locations: the Waja section located west of the town of Waja along the Kobo-Lalibela Mountain Road (12.127°N, 39.412°E; Figure 3.1) and the Termaber-Gussa Basalts on a mountain road that was still under construction at the time, north of Lalibela (12.101°N, 39.082°E; Figure 3.1). The Ashangi formation near the base (1,500–2,500 m in altitude) is highly weathered and tilted yet with poorly exposed bedding structures. In contrast, the Aiba basalts and Alaje formation (2,500–3,500 m altitude) are horizontally stratified, clearly exposed, and suitable for palaeomagnetic investigations (Figure 3.2). We used a petrol-powered drill, to collect 923 cores in 117 cooling units in the Aiba basalts and Alaje formation (ca. eight one-inch palaeomagnetic cores per unit). The cores were oriented with a Pomeroy device, with sundial readings in 82% of the cases, leading to an average magnetic anomaly of 2.7±1.9°, which coincides well with the predicted IGRF (Thébault et al., 2015) declination of 2.6° after discarding data from sites W014 (6.2°) and W024 (15.8°).

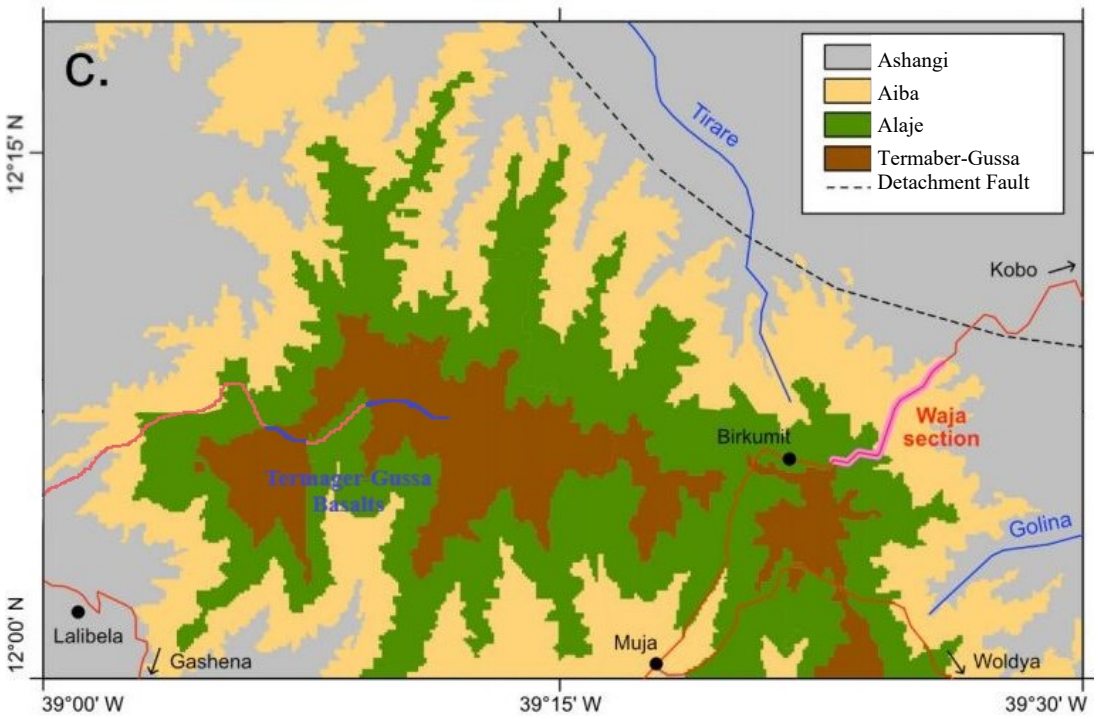

Figure 3.1 Simplified geological map (adapted from Eid et al., 2022; Tadesse et al., 2011) showing the geological settings of the Waja section (12.127°N. 39.412°E. 2400–3500 m) and the sampled Termaber-Gussa Basalts (12.101°N, 39.082°E. 3500–4000 m) located in the eastern part of the northern Ethiopian plateau.

The Termaber-Gussa formation from 3,550–4,050 m in altitude was horizontally stratified and exhibited good potential for palaeomagnetic investigation. It was sampled using a petrol-powered rock drill obtaining 106 cores in 14 cooling units (ca. eight one-inch palaeomagnetic cores per unit). However, 30% of orientations needed to be discarded since they exhibited a magnetic anomaly >10°, this could be explained by the fact that the Termaber-Gussa formation is located at high altitudes making it more susceptible to lightning strikes.

Figure 3.2: Field photographs (adapted from Eid et al., 2022) of the Waja section (12.127°N, 39.412°E). (a) overview of the section. (b-e) details from flows W004 (2497 m), W068 (3019 m), W082 (3110 m) and W118 (3509 m).

3.2. Geochemistry

3.2.1. X-Ray Fluorescence

Methods

Sample powders (grain size < 63 μm) were first dried at 110°C for more than two hours and subsequently ignited at 1050°C for more than six hours to determine the loss on ignition (L.O.I). Following the L.O.I, glass beads were prepared by fusion of 1 g ignited sample powder and 9 g SPECTROMELT A12 (66% di-lithium tetraborate, 34% lithium metaborate) in a PANalytical Eagon 2 furnace fusion system. Major and minor element contents of the whole rocks were measured by Donjá Aßbichler at Ludwig-Maximilian University (LMU) using a Philips MagiX Pro WD-XRF spectrometer. The calibration was done using international certified standards and analytical quality was ensured by analysing USGS reference materials as unknowns.

Results

Whole-rock powders from 21 flows underwent XRF measurements (Table 3.1) and yielded TiO_2 concentrations of 3.8±0.5 wt.%, representative of the HT2 classification (TiO2 3–7 wt%, Pik et al., 1998). The mean L.O.I values for flows below 3000 m was 1.52 wt.% compared to 0.67 wt.% from flows above 3000 m which was consistent with the visual determination that the older flows underwent more weathering than the consequently younger ones. After taking L.O.I values and K_2O concentrations into consideration, six flows were chosen and samples from which were sent for $^{40}Ar/^{39}Ar$ dating (Table 3.3).

The XRF results also allowed us to compare the data from the Waja and Belessa sections in contrast with data from low titanium (LT; 1–3 wt%), intermediate-high titanium (HT1; 2–4 wt%) and high titanium (HT2; 3–7 wt%) (Beccaluva et al., 2009; Lhuillier & Gilder, 2019; Natali et al., 2016; Pik et al., 1998, 1999) basalts from the EYT. On the Total Alkali-Silicate (TAS) (Le Bas et al., 1986) diagram (Figure 3.3), it is evident that the samples obtained from the Termaber-Gussa formation (above 3600 m in elevation) are of different geochemical composition compared to the Waja section. Samples from the Aiba and Alaje formations (Waja basalts below 3600 m) except for two flows (23 and 24) plot within the picritic field or close to it, consistent

with Beccaluva et al. (2009) and Natali et al. (2016) who interpreted the HT2 basalts as being more primitive and characteristic of the central part of the Afar plume.

Table 3-1: Major Elements results in (wt.%) computed from X-Ray fluorescence measurements alongside the sample's elevation and its corresponding Loss On Ignition (L.O.I) values. Results shown are from the Waja section (L004–L119) and from the Termaber-Gussa formation (L132–L143)

Study	Location	Group	Sample	Elev. (m)	SiO_2	Al_2O_3	Fe_2O_3	MnO	MgO	CaO	Na_2O	K_2O	TiO_2	P_2O_5	Total	L.O.I
Eid et al. (2021)	Waja	HT2	L004	2500	44.61	7.09	15.46	0.18	14.48	10.02	1.36	0.82	4.13	0.47	100.5	1.46
			L005	2516	44.62	7.49	15.40	0.17	13.00	10.04	1.71	0.88	4.49	0.51	100.2	1.58
			L020	2682	44.33	7.28	15.73	0.18	13.43	9.72	1.76	0.99	4.49	0.55	99.43	0.69
			L021	2695	45.03	7.30	15.11	0.17	14.12	9.65	1.86	0.76	4.23	0.47	100.4	1.38
			L023	2725	51.34	9.77	11.88	0.13	6.56	7.68	1.47	4.49	4.00	0.46	99.59	1.58
			L024	2734	48.63	8.96	14.07	0.17	6.80	10.24	1.17	3.54	4.49	0.57	100.5	1.69
			L025	2744	44.50	6.93	15.11	0.18	14.99	9.22	2.26	0.61	4.18	0.43	100.5	1.81
			L026	2751	44.00	7.32	14.86	0.18	14.62	9.63	1.59	0.73	3.99	0.41	99.06	1.45
			L027	2757	42.68	6.23	14.80	0.19	17.93	9.86	0.89	0.56	3.17	0.32	99.76	2.74
			L078	3085	44.57	6.44	14.90	0.17	17.23	8.59	1.79	0.59	3.36	0.38	99.35	0.94
			L082	3095	44.80	6.60	14.95	0.17	17.24	9.02	1.35	0.73	3.16	0.37	99.69	0.84
			L080	3107	43.15	6.12	15.09	0.19	18.45	8.94	1.09	0.69	3.23	0.33	99.81	2.05
			L081	3109	42.97	6.29	14.81	0.19	17.93	9.23	1.01	0.73	3.11	0.32	99.84	2.83
			L116	3487	44.81	7.84	15.10	0.17	12.38	10.24	1.89	0.97	4.60	0.56	99.08	0.21
			L117	3492	44.44	6.82	15.37	0.18	15.38	9.58	1.56	0.78	3.95	0.46	99.24	0.40
			L118	3505	45.00	6.73	15.01	0.17	15.16	9.95	1.63	0.83	3.83	0.44	99.10	0.02
			L119	3516	44.79	7.40	15.09	0.18	14.52	9.46	1.64	0.80	3.99	0.46	99.29	0.65
-	Termaber-Gussa	HT2	L132	3605	48.10	12.11	16.34	0.20	4.71	10.18	2.66	0.71	3.78	0.59	99.66	0.14
			L134	3683	46.37	14.51	13.01	0.25	3.37	10.68	3.81	1.94	3.13	1.16	99.41	0.89
			L142	3967	40.98	11.93	17.19	0.20	7.41	13.38	2.97	0.40	4.34	0.65	101.2	1.54
			L143	4050	45.87	14.37	13.66	0.21	4.11	11.18	3.96	0.85	3.54	0.93	100.1	1.18

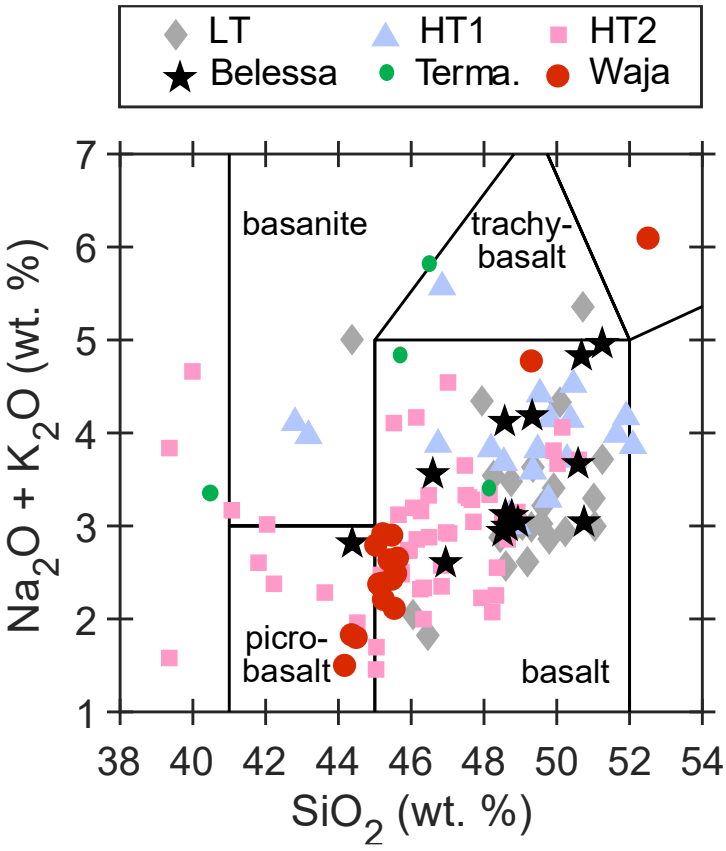

Figure 3.3: Total alkali – silica diagram (Le Bas et al., 1986) (adapted from Eid et al., 2021) of the Belessa (LT) and Waja (HT2) sections, Termaber-Gussa formation (Green) compared with previous studies (Beccaluva et al., 2009; Lhuillier & Gilder, 2019; Natali et al., 2016; Pik et al., 1998, 1999; Table 3.1).

3.2.2. Rare Earth Elements

Methods

Trace elements of the whole rocks were determined by ICP-MS at the mineral laboratory of Bureau Veritas in Canada. The calculations and analysis based on the Rare Earth Element concentrations were performed in collaboration with Jörg Pfänder at the Technische Universität Bergakademie Freiberg.

Results

To attain more concrete confirmation for the hypothesis that the sampled Waja Basalts are more primitive in nature than the Belessa Basalts, eight samples from the Waja section and six from the Belessa section were chosen for Rare Earth Elements (REE) determination (Table 3.2). Chondrodite-normalized REE patterns determined from the selected samples confirm that Waja conforms to HT2 while Belessa to LT basalts (Figure 3.4). The ratio La/Sm gave values of 3.5-4.4 at Waja and 2.6-3.4 at Belessa, Sm/Yb gave values of 4.5-5.6 at Waja and 2.3-3.2 at Belessa; both suggested lower partial melt composition and a deeper source for the Waja basalts in contrast with higher partial melt composition and a shallower source for the Belessa basalts.

Table 3-1: Rare Earth Elements (ppm) from The Waja section

Study	Location	Group	Sample	La	Ce	Pr	Nd	Sm	Eu	Gd	Tb	Dy	Ho	Er	Tm	Yb	Lu
Eid et al. (2021)	Waja	HT2	L004	33.2	74.7	10.13	44.1	9.51	2.84	8.6	1.15	5.75	1.03	2.48	0.3	1.82	0.24
			L005	36	80.3	10.72	46.6	10.09	3.03	9.1	1.23	6.2	1.04	2.67	0.34	1.95	0.26
			L020	40.1	88.4	11.85	49.4	10.33	3.12	9.21	1.27	6.27	1.06	2.54	0.33	1.85	0.25
			L023	34.5	79.4	10.36	44.8	9.68	2.92	8.84	1.24	6.3	1.08	2.62	0.33	2	0.26
			L078	26.4	57.8	7.74	34.7	7.42	2.24	6.81	0.96	4.74	0.84	2.1	0.27	1.52	0.22
			L082	27	59.2	7.76	33.3	7.23	2.22	6.78	0.94	5	0.84	2.18	0.26	1.6	0.21
			L116	46.4	101.3	13.35	55.3	10.85	3.32	9.6	1.26	6.41	1.08	2.68	0.33	2.01	0.27
			L118	36.4	78.3	10.02	42.4	8.36	2.6	7.73	1.01	5.07	0.85	2.22	0.27	1.6	0.21

Partial melt modelling based on REE partition coefficients of garnet and spinel peridotite suggested that the Waja basalts were derived from a primitive mantle source (Sun & McDonough, 1989) in the garnet stability field (i.e., at a depth >~75 km) with

~3% of partial melt (Figure 3.4 b). In contrast, REE patterns from Belessa suggest a primitive mantle source at the transition between the spinel and garnet stability fields (Figure 3.4 a), i.e., a two-stage model with initial partial melting in the garnet stability field followed by partial melting or melt equilibration in the spinel stability field. Because crustal contamination tends to produce concave REE patterns, the slightly convex shape of the latter argues against significant crustal contamination (Figure 3.4).

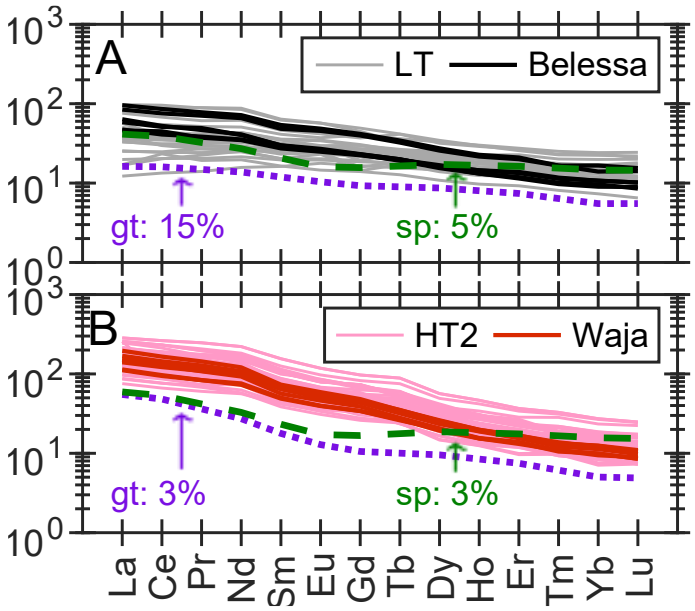

Figure 3.4: Chondrite-normalized Rare Earth Element (REE) patterns (Sun & McDonough. 1989) (adapted from Eid et al., 2021) for the Belessa (LT) and Waja (HT2) basalts compared with other LT and HT2 basalts (Beccaluva et al., 2009; Lhuillier & Gilder, 2019; Natali et al., 2016; Pik et al., 1998, 1999 Table 2.2). The label x% indicates calculated composition (non-modal batch melting) of a basalt derived by x% partial melting of a garnet (gt) or spinel peridotite (sp) with a primitive mantle like trace-element composition (Sun & McDonough, 1989).

3.3. Geochronology

Methods

The sample preparation and geochronology was performed in collaboration with Jörg Pfänder at the Technische Universität Bergakademie Freiberg. Groundmass fragments were separated using standard methods and handpicked to remove any visually observable alteration and secondary phases. The 300-500 µm size fractions were then repeatedly washed in deionised water in an ultrasonic bath to remove any fine-grained particles and dust. After drying, the samples were wrapped in Al foil and loaded along with fluence monitors in wells of an Al disc (33 mm diameter). The samples were then sent to be irradiated without Cd-shielding for 17.75 hours in the rotational facility of the LVR-15 research reactor of the Centrum Výzkumu Řež (CVŘ), Czech Republic. The thermal (<0.5 eV), fast (>1 MeV) and total neutron fluence rates were ~3.7×1013 n/cm^{2}s, ~7.5×1012 n/cm^{2}s and ~7.6×1013 n/cm^{2}s at a reactor power of 8.2 MW.

After irradiation, the samples were unwrapped and ~10-20 mg was loaded into 5- or 7-mm diameter wells on an oxygen-free copper disc for laser step wise heating. The latter was performed using a 25 W Synrad CO_2-laser coupled to a Raylase Scan-head for beam deflection. Deflection frequencies were 55 and 300 Hz on the x and y axes, and the amplitude of the Scan-head was set correspondingly to cover the individual sizes of the wells. Gas purification was achieved by two SAES NP10 getter pumps, one at room temperature and one at ~400°C. Heating and cleaning times were 3 min and 5 min per step. Argon isotope compositions were measured in multi-dynamic mode on a Thermo ARGUS VI noble gas mass spectrometer equipped with five faraday cups (1011 Ω resistor at position H2, 1012 Ω resistors at positions H1 to L2) and a CDD multiplier at the low mass side (L3). Typical blank levels range between 0.5×10^{-16} to 1.4×10^{-16} mol ^{40}Ar and 1.0×10^{-18} to 3.4×10^{-18} mol ^{36}Ar. Twenty cycles with a total duration of ~9 min was measured per temperature step. Each cycle comprised two acquisition sequences with masses 38 and 39 on the axial cup, respectively, and 8.4 s integration time plus 5.0 s delay per sequence.

For time-zero intercept calculation, blank-, mass-bias and interference correction was used by a Matlab® toolbox compiled at the Technische Universität Bergakademie Freiberg. Mass bias was corrected assuming linear mass dependent

fractionation and using an atmospheric $^{40}Ar/^{36}Ar$ ratio of 298.6 ± 0.3 (Lee et al., 2006). Isochron, inverse isochron and weighted mean average (plateau) ages have been calculated using ISOPLOT 3.7 (Ludwig, 2008). All ages were calculated relative to the in-house standard DRF1 (Drachenfels sanidine) as a fluence monitor with an age of 25.682 ± 0.030 Ma, calibrated against a Fish Canyon Tuff sanidine (FCs) age of 28.305 ± 0.036 Ma (Renne et al., 2010). For reasons of comparability, all ages referred to in the main text and figures have been recalculated to a FCs age of 28.172 ± 0.028 (Rivera et al., 2011) using the decay constants of Min et al. (2000). All reported errors are 1σ. Interference correction factors are given in the supplementary dataset.

Results

The results reported are the inverse isochron Ar-Ar ages instead of plateau ages from age spectra data because the calculation of the latter is usually done under the assumption of an atmospheric initial Ar isotope composition. Non-atmospheric initial compositions due to argon loss or the presence of excess argon, however, compromise the age spectra in a way that no plateau might be identifiable. In contrast, isotope ratio plots of $^{36}Ar/^{40}Ar$ vs. $^{39}Ar/^{40}Ar$ (inverse isochron diagrams) do not assume a predetermined precise initial Ar isotope composition (atmospheric $^{40}Ar/^{36}Ar$ = 298.6 ± 0.3; Lee et al., 2006), but calculates it from the data themselves with the effect of propagating the data scatter (over- or under dispersion expressed by MSWD >1 or <1; see Schaen et al., 2021 for details) into the initial value and therefore resulting in a larger uncertainty which is, in addition, dependent on the spread of the data. We suggest that this larger uncertainty, which also propagates into the inverse isochron age, is a more realistic estimate of the initial value. This is also valid for the inverse isochron age itself and its assigned error.

Five samples from the Aiba and Alaje formations and one from the Termaber-Gussa formation were chosen for the purposes of accurately dating the Waja section. Five whole-rock $^{40}Ar/^{39}Ar$ ages were determined for flows at elevations of 2500 m (W004), 2680 m (W020), 3110 m (W082), 3490 m (W116), 3510 m (W118) and 4050 m (W143). The inverse isochron ages except for W143 (17.02 ± 0.43) range between 30.96 ± 0.12 and 31.84 ± 0.14 Ma (1σ), with close to atmospheric (298.56 ± 0.31; Lee et al., 2006) initial $^{40}Ar/^{36}Ar$ values (Figure 3.5, Table 3.3). The fact that the age from the Termaber-Gussa formation (W143) was 14 Myr younger than the rest of the

sampled formations along with the contrast in chemical composition observed in the TAS diagram (Figure 3.3) made it clear that the Termaber-Gussa formation is a consequence of shield volcanism that occurred after the end of flood basalt volcanic activity. Therefore, the Termaber-Gussa formation was excluded from further analysis.

Table 3-3: $^{39}Ar/^{40}Ar$ ages from Waja section recalculated to a Fish Canyon Tuff sanidine age of 28.172 ± 0.028 Ma (Rivera et al., 2011) and using the decay constants of Min et al. (Min et al., 2000). Sample W143 was not published.

Study	Section	Site	Sample type	Original Data				Recalculated Data	
				Age (Ma)	σ (Myr)	Standard	Decay Constant	Age (Ma)	σ (Myr)
Eid et al. (2021)	Waja	W004	Whole Rock	31.37	0.14	DRF1 (25.682) Renne et al. (2010)		31.22	0.14
		W020		31.11	0.12			30.96	0.12
		W082		31.54	0.18			31.39	0.18
		W116		31.99	0.14			31.84	0.14
		W118		31.41	0.11			31.26	0.11
-	Termaber-Gussa	W143		17.10	0.43			17.02	0.43

Excluding sample W116 with a marked sub-atmospheric initial $^{40}Ar/^{36}Ar$ ratio, the $^{40}Ar/^{39}Ar$ ages are indistinguishable within their 2σ errors and thus we computed a weighted-mean $^{40}Ar/^{39}Ar$ eruption age for the Waja section of 31.18 ± 0.28 Ma (95% confidence; Ludwig, 2008). The 2σ-precision of this age (internal error) is ± 0.13 Ma, suggesting that the Waja section was emplaced over a period less than ~260 kyr. Compared to other $^{40}Ar/^{39}Ar$ ages from the EYT, the Waja section was clearly emplaced at the beginning stages of trap eruption (Figure 3.5).

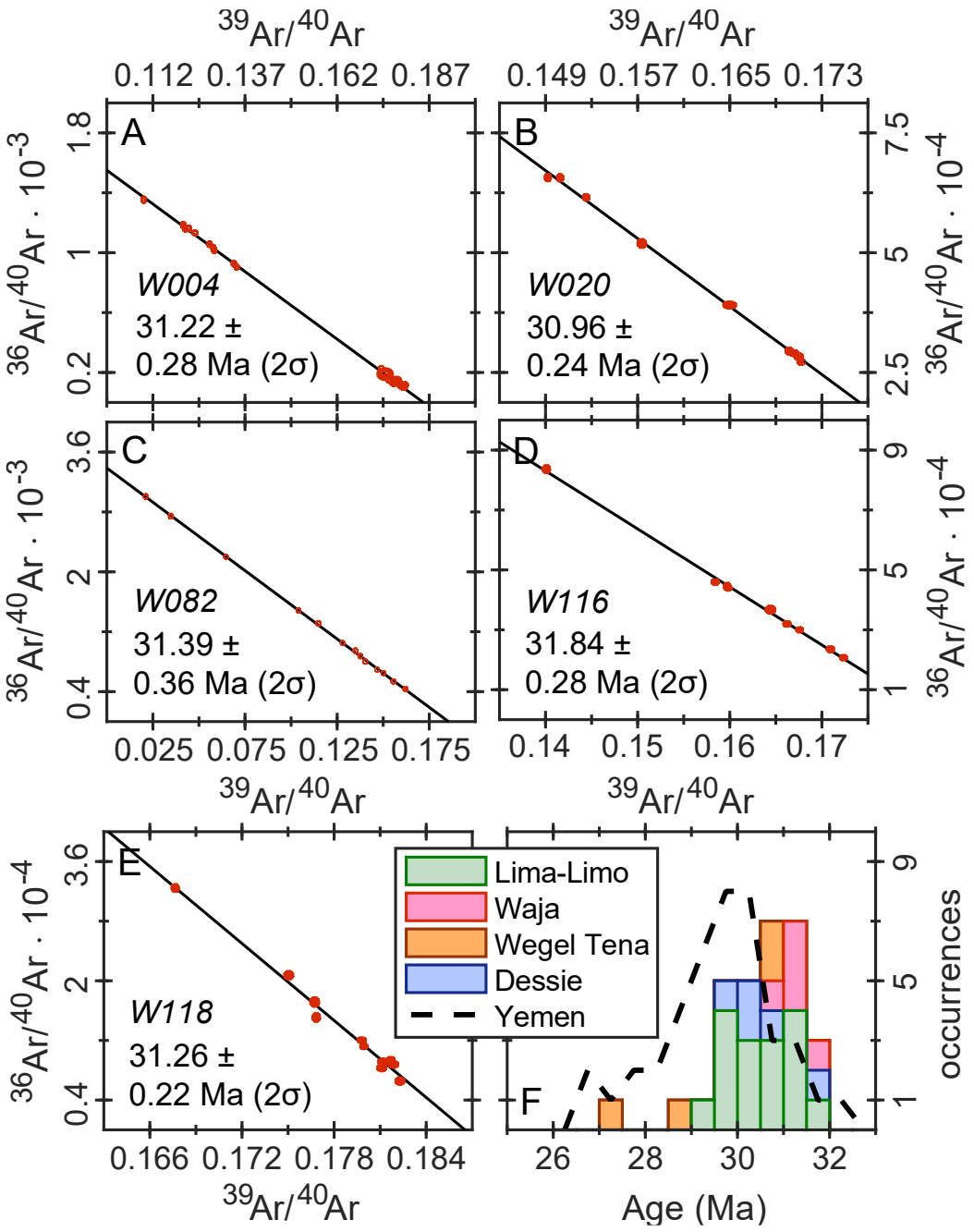

Figure 3.5: $^{40}Ar/^{39}Ar$ dating results (adapted from Eid et al., 2021). (a – e) $^{40}Ar/^{39}Ar$ inverse isochron ages for flows W004 (2500 m). W020 (2680 m). W082 (3110 m). W116 (3490 m). and W118 (3510 m). Error ellipses on individual data-points are 1σ. (f) Compilation of $^{40}Ar/^{39}Ar$ ages for Ethiopia (data from Coulié et al., 2003; Hofmann et al., 1997; Rochette et al., 1998; Ukstins et al., 2002) and Yemen (Baker et al., 1996; Riisager et al., 2005, Table 2.3) recalculated to a Fish Canyon Tuff sanidine age of 28.172 ± 0.028 Ma (Rivera et al., 2011) and using the decay constants of Min et al. (Min et al., 2000).

4. Rock-magnetism

4.1. Königsberger Ratio

Methods

To exclude any remagnetised samples due to lightning, the Königsberger ratio Q (Koenigsberger, 1938) was determined which provided some insight into the magnetic quality of the sites. To obtain Q for each sample, its NRM was normalized by the induced magnetization (magnetic susceptibility * present-day magnetic field/the magnetic constant).

$$Q = \frac{NRM}{B \cdot \chi_m} / \mu_0$$

NRM = Natural remanent magnetization of the sample (A/m)

B = The present-day magnetic field (μT)

χ_m = The magnetic susceptibility of the sample (1)

μ_0 = The magnetic constant ($1.25663706 \cdot 10^{-6}$ $m \cdot kg/s^2 \cdot A^2$)

The Magnetic Susceptibility was measured using a Bartington MS2B meter operating at a frequency of 0.465 kHz followed by measurements of the Natural Remanent Magnetization (NRM) using an AGICO JR6 spinner magnetometer. The present-day magnetic field at Lalibela was computed using the IGRF-12 model (Thébault et al., 2015), resulting in B = 36 μT.

Results

Thirteen sites were determined to have been contaminated most likely by lightning strikes since their Q was >20. Figures 4.1 and 4.2 portray the site-mean susceptibility, NRM and Königsberger ratio values along with their histogram and the probability density function (PDF).

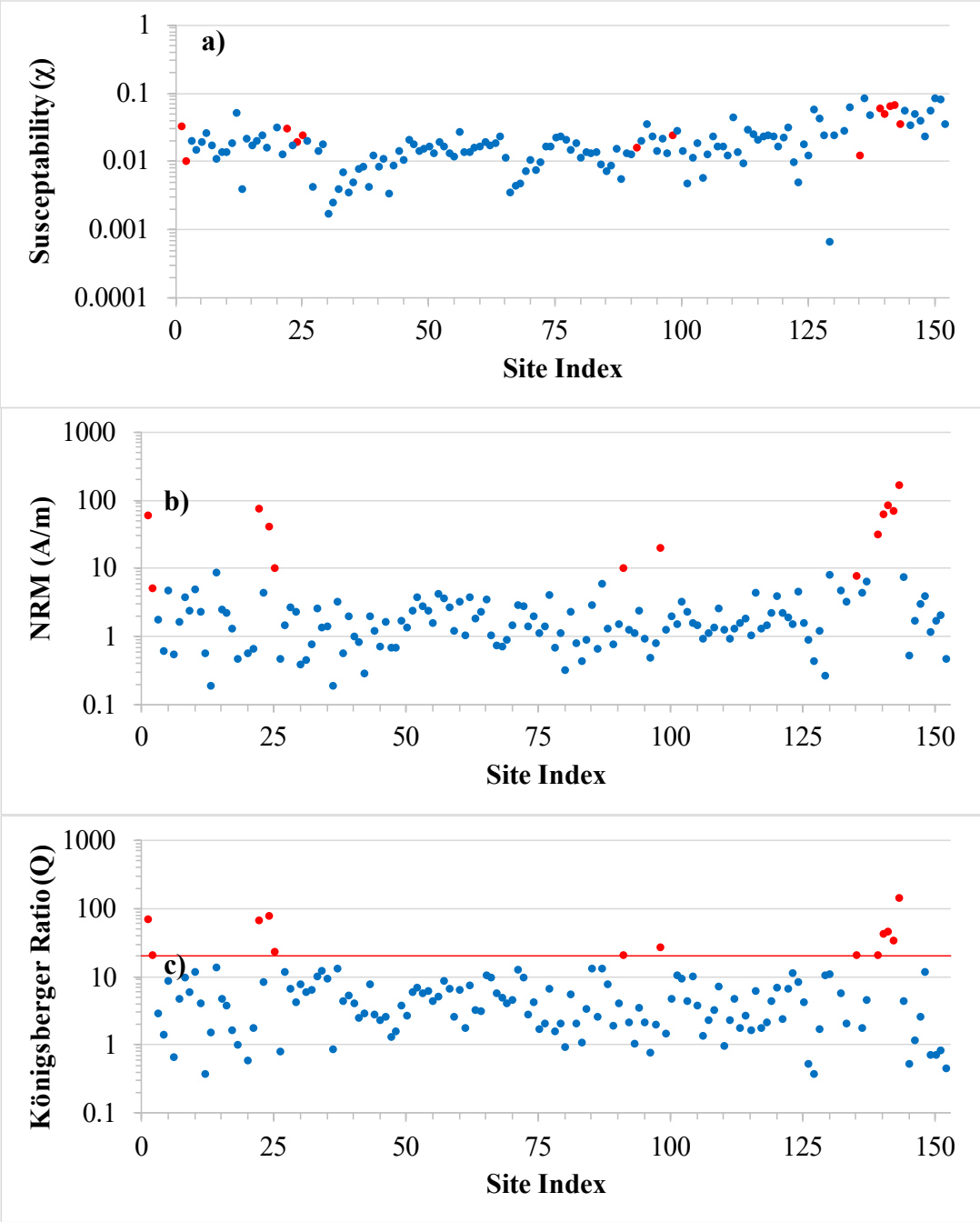

Figure 4.1: Site-mean Susceptibility (a), NRM (b) and Königsberger Ratio values (c). Sites accepted for further measurements (blue) and sites rejected (red) due to having Q>20 (red line in panel c).

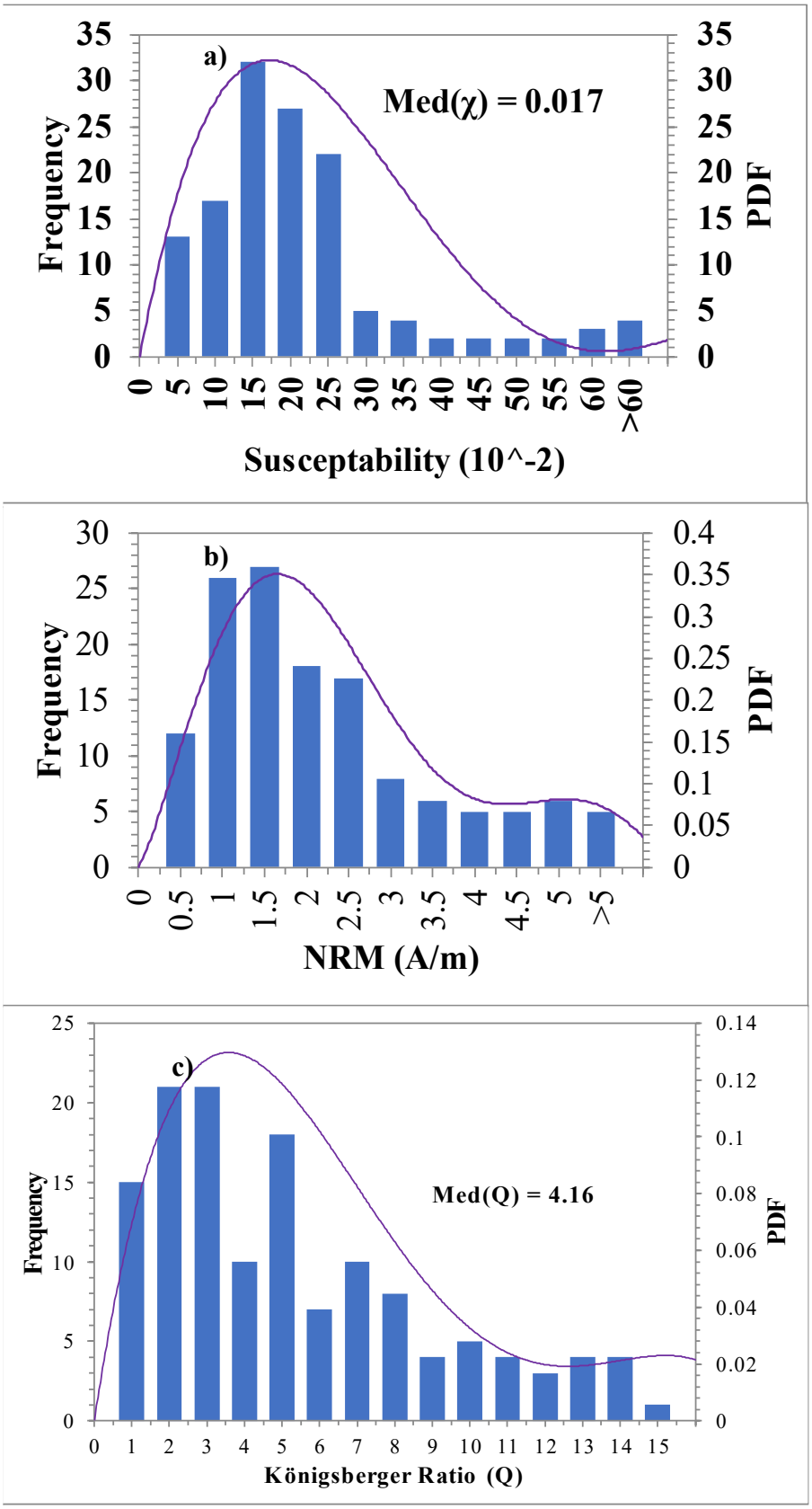

Figure 4.2: Histograms showing probability density function (PDF) and median values were obtained from the accepted site-mean values. Site-mean Susceptibility (a), NRM (b) and Königsberger Ratio values (c).

4.1. Hysteresis Parameters

Methods

To better characterise the magneto-mineralogy of the section, we determined, at the Ludwig Maximilian University (LMU) of Munich, the hysteresis parameters using a one-component Vibrating Sample Magnetometer (VSM) manufactured by Lakeshore. Hysteresis and backfield curves were obtained from the pilot samples, the paramagnetic contribution of the samples, which contaminated the hysteresis loops results, were filtered out. With this it was then possible to compute the standard hysteresis parameters:

M_s	=	Saturation magnetization	(Am^2)
M_{rs}	=	Remnant saturation magnetization	(Am^2)
B_c	=	Coercive force	(T)
B_{cr}	=	Remanent coercive force	(T)

Results

The calculated *Mrs/Ms* ratios produced values with a mean of 0.12 while the *Bcr/Bc* values had a mean of 2.63 (Figure 4.3 a–b). The Mrs/Ms ratios were plotted against the *Bcr/Bc* ratios, giving us the Day plot (Day et al., 1977). Of specific interest were the results from W035, W060, W062, W105, W108, W114 and W117 which were the flows that gave Thellier-Coe API results that passed our selection criteria (Figure 4.3, Day et al., 1977). The Day diagram shows the bulk hysteresis properties, which could be used to estimate the hypothetical domain structures of the tested samples.

The results coincide with the SD-MD mixing curves of magnetite (Dunlop, 2002), with flows W035, W060 and W062 (hereafter termed group 1) closer to the SD area; flows W105, W108, W114 and W117 (hereafter termed group 2) closer to the MD area (Figure 4.3c). However, due to the intricate nature of magnetic domain states further observations were needed to be made to determine the suitability of the collected samples for API determination.

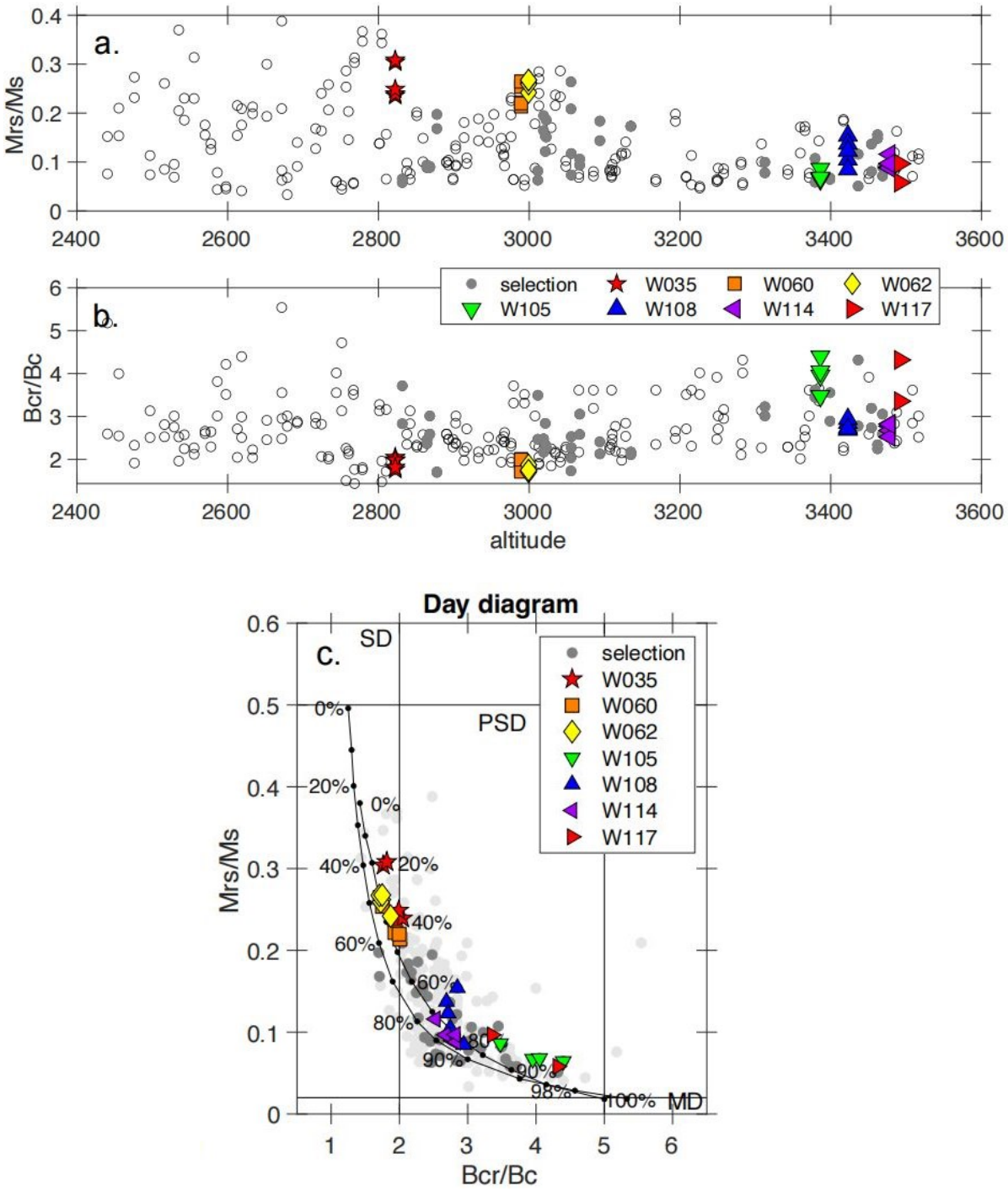

Figure 4.3: Bulk hysteresis parameters from the Waja section (adapted from Eid et al., 2022). (a) Ratio of remanent saturation magnetization (*Mrs*) to saturation magnetization (*Ms*) as a function of elevation. (b) Ratio of the remanent coercive force (*Bcr*) to the coercive force (*Bc*). (c) Day diagram with the SD-MD mixing curves of magnetite (Dunlop, 2002). The grey discs represent the 27 preselected flows for absolute palaeointensity determinations whereas the colour-coded symbols represent the seven flows reported in this study.

4.2. Thermomagnetic Experiments

4.2.1. Susceptibility and Magnetization Curves

Methods

A solenoid-based Variable Field Translation Balance (VFTB) was used to produce the continuous thermomagnetic curves for two samples per cooling unit.

M(T) : Magnetization Vs Temperature

$\chi(T)$: Magnetic susceptibility Vs Temperature

The experiments were performed in air from room temperature up to 620˚C and in the ambient magnetic field (300 mT for 60 s before commencing the measurement and no applied field during measurement). The minimum of the first derivative of the heating and cooling of the $\chi(T)$ curves was used to estimate the Curie temperature (T_C) of the different samples.

Results

Approximately 60% of the measured samples showed a negligible signal from possible secondary phases, making it easy to identify the dominant Curie points (Figure 4.4). The remaining 40% of samples clearly showed at least one secondary phase between 300–400°C and exhibited several characteristics that could be sorted into three distinct types (Figure 4.5).

Type 1 showed evidence for a tertiary phase between 100–200°C along with a highly noticeable difference in χ between heating and cooling (Figure 4.5 a). Type 2 had a prominent secondary phase and the χ recovered quite well after cooling (Figure 4.5 b), type 3 was like type 2 however with a less noticeable secondary phase (Figure 4.5 c).

It was determined that the dominant Curie point lay between 450 and 550°C. The apparent dichotomy between the two groups of samples that produced API results is also visible on the $\chi(T)$ curves with a dominant Curie point T_C = 540–560°C for group 1 (Figure 4.6 b–c), and T_C = 500–530°C for group 2 (Figure 4.6 d–f).

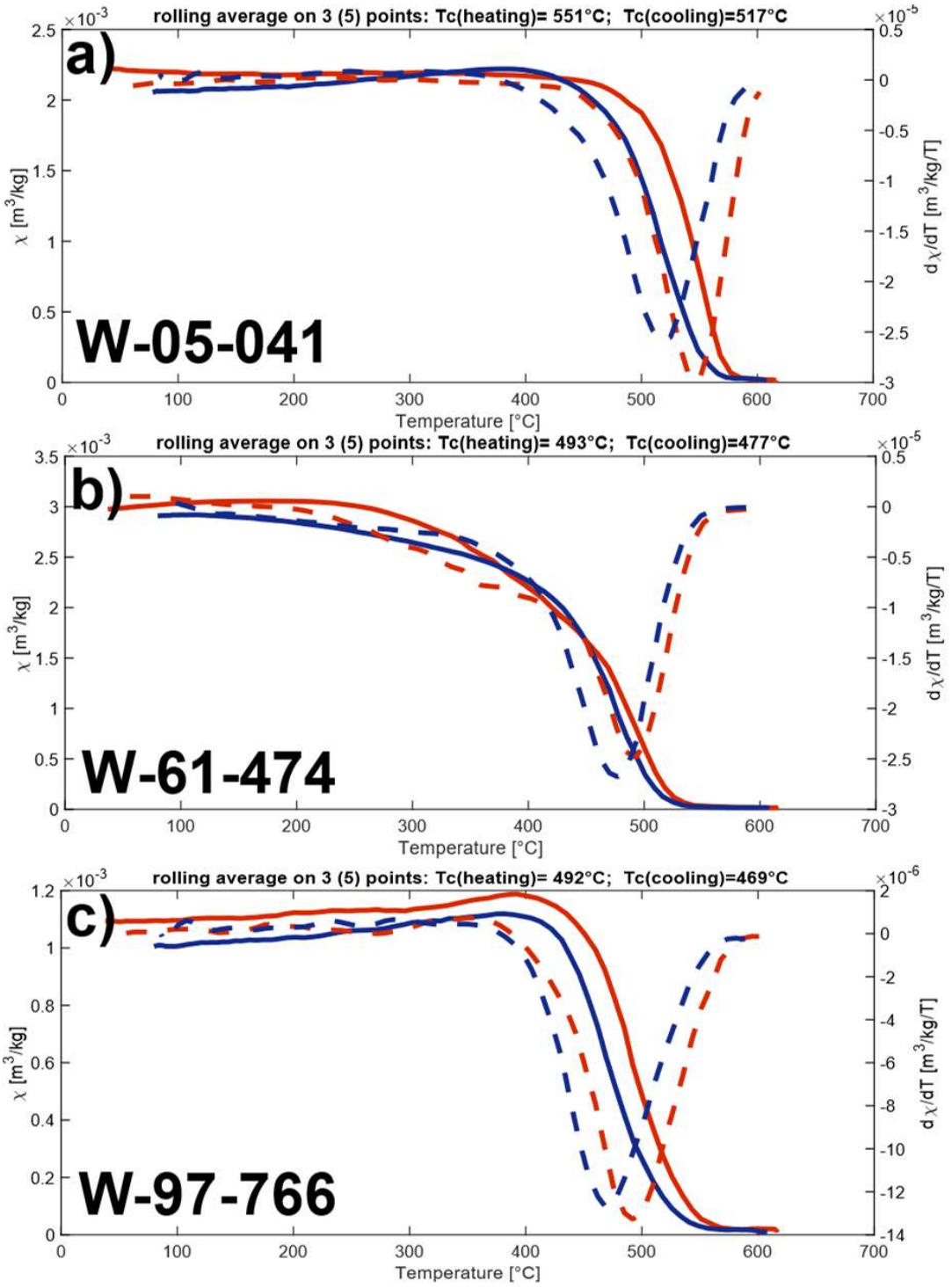

Figure 4.4: Samples with easily identifiable dominant Curie point and negligible influence of secondary phases. Heating (red) and cooling (blue) branches of the *χ(T)* curves for typical samples from the Waja section, continuous curves are the measured χ values, dashed curves show $d\chi/dT$, *Tc* (heating and cooling) values were interpreted according to the $d\chi/dT$ minima.

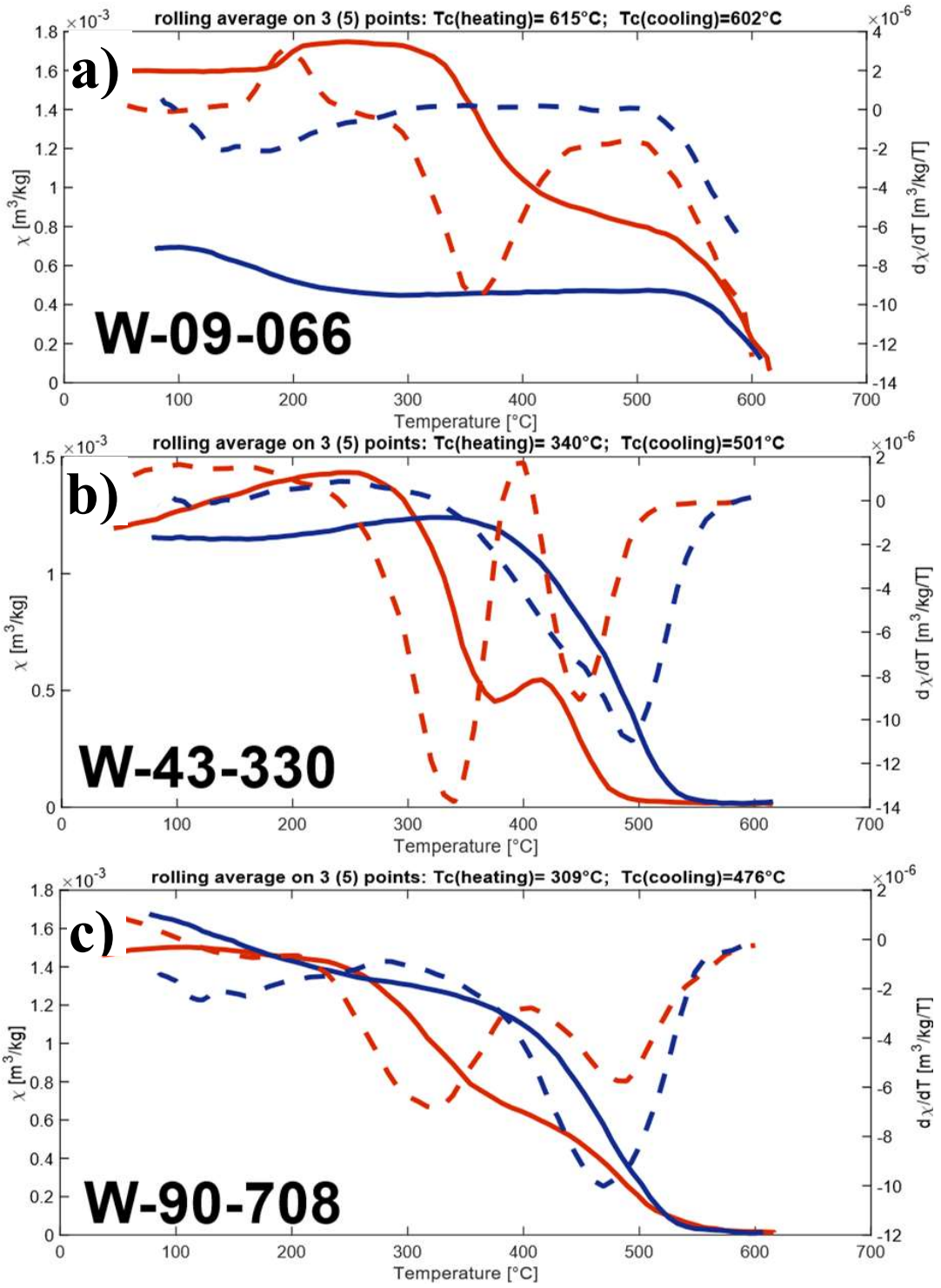

Figure 4.5: Samples with ambiguous dominant Curie point due to the presence of prominent secondary phases. Heating (red) and cooling (blue) branches of the $\chi(T)$ curves for typical samples from the Waja section, continuous curves are the measured χ values, dashed curves show $d\chi/dT$, *Tc* (heating and cooling) values were interpreted according to the $d\chi/dT$ minima.

4.2.2. Cyclic Magnetization Curves

Methods

Determining flows suitable for API measurements required further thermomagnetic investigation, namely the reversibility of the samples' magnetization during heating. For that purpose, samples from selected sites had to undergo cyclic *Ms(T)* curves using an electromagnet based VFTB in a field of 100 mT which may not have allowed the samples to reach saturation but was considered as the best option since higher fields would have caused the equipment to overheat. The cycles were as follows: *Tmax* = 200, 300, 400, 500, 600°C for two samples per flow (Figure 4.6).

Results

From the Cyclic *Ms(T)* curves thermal stability could be quantified by calculating the changes between the different *Ms(T)* heating and cooling branches for each *Tmax*. Twenty-five out of 117 sites produced cyclic *Ms(T)* curves with less than 20% variation were determined to be thermally stable up to 600°C meaning they were suitable for API determination. However, samples with greater than 20% difference were rejected since they were deemed to lack thermal stability.

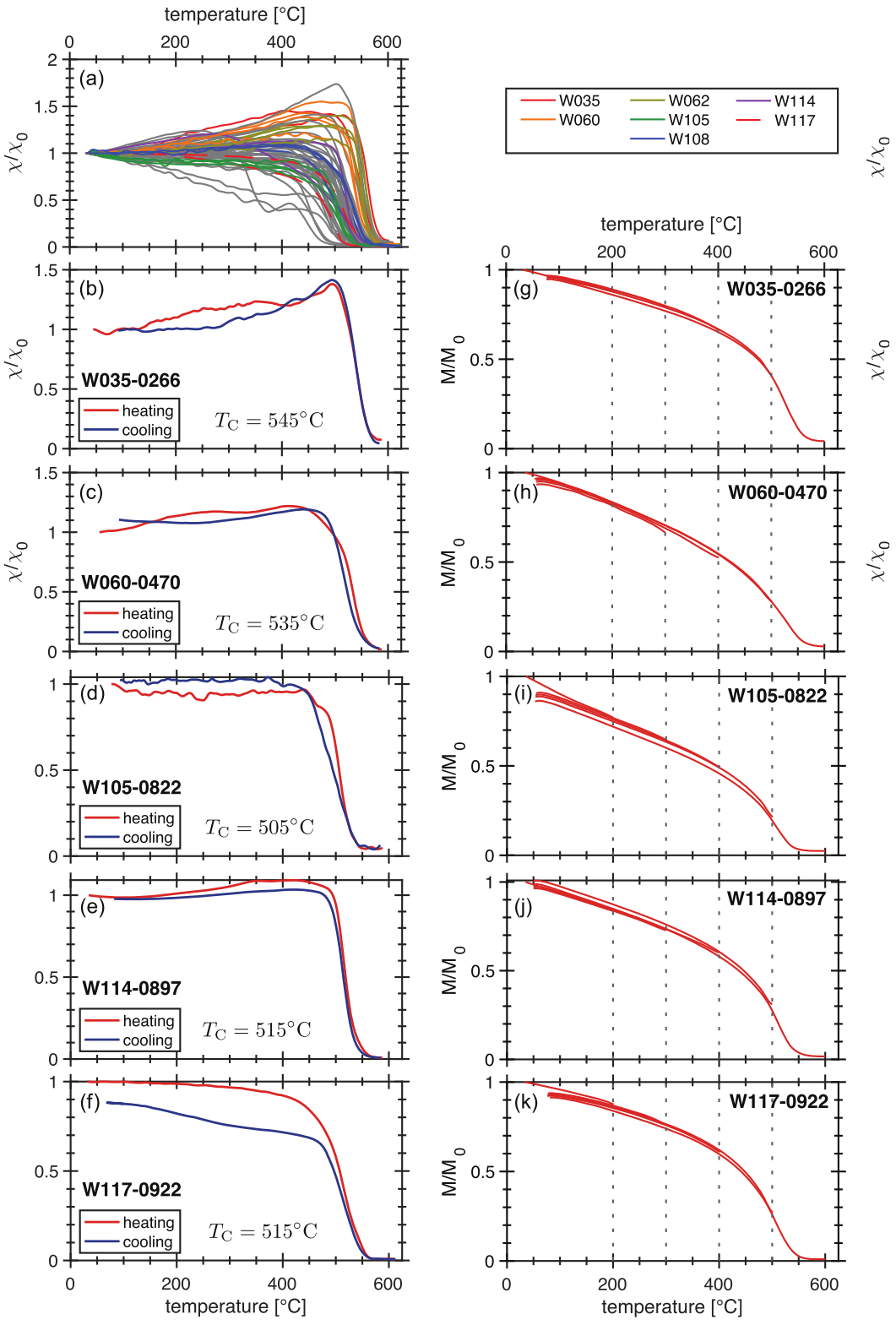

Figure 4.6 Thermomagnetic behaviour from the Waja section (adapted from Eid et al., 2022). (a) Heating branches of the *χ(T)* curves for the whole section. (b–f) Heating and cooling branches of the *χ(T)* curves for typical samples. (j–k) Heating branches of the cyclic *Ms(T)* curves for the same samples. The dashed vertical lines mark the successive maximal temperatures.

4.2.3. pTRM Tail Experiments

Methods

The domain structure of 1 cm cube samples, selected based on API results, was assessed by obtaining the amplitude of partial thermoremanent magnetization (pTRM) tails by a collaborator at the Borok Geophysical Observatory using an ORION two-component VSM with a noise threshold of $3*10^{-9}$ Am^2 with a maximum external field of 0.4 mT and a field of <100 nT with the coil switched off. To this end, the sample was first cooled down from T_C, with a laboratory field B_{lab} switched on between T1 and T2 to impart the pTRM (T1, T2). The sample was then demagnetised until T1 and cooled down in zero field to monitor the presence of a pTRM tail.

Results

pTRM tail experiments on four select samples point to the presence of small-size PSD grains (tail amplitude of 4–7%, Figure 4.7), closer to SD grains (tail amplitude ≤ 5%) than MD grains (tail amplitude ≥ 15%; Shcherbakova et al., 2000)).

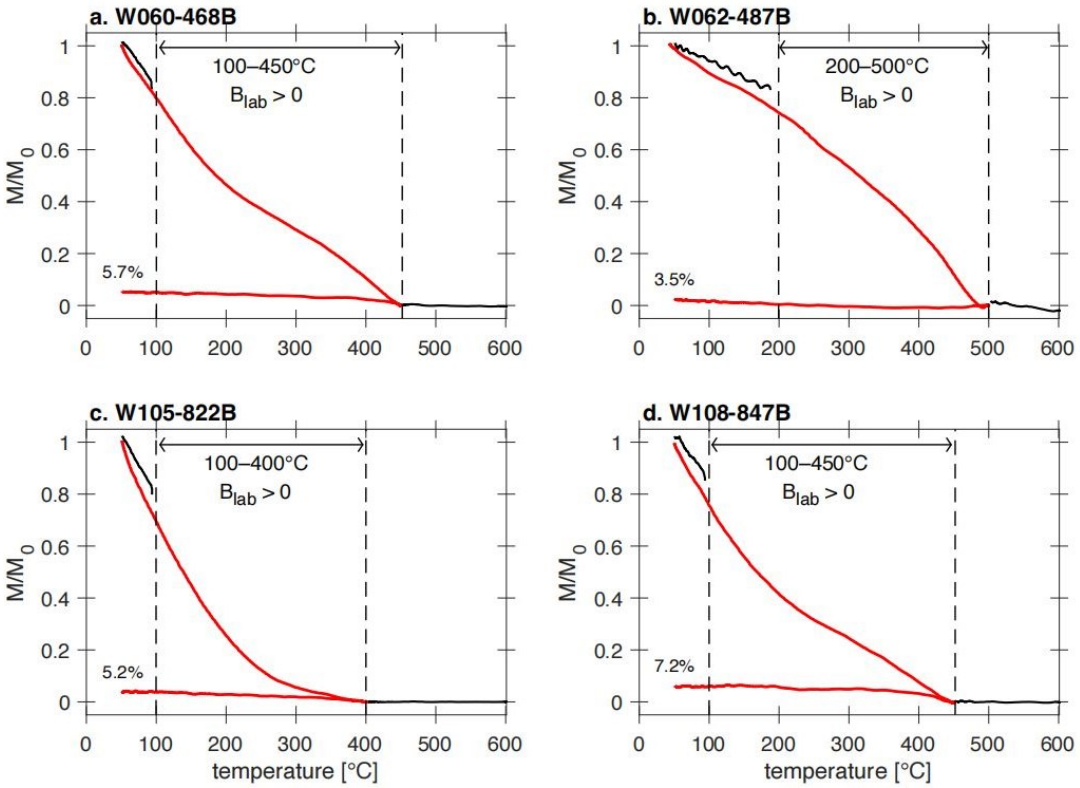

Figure 4.7: Typical pTRM tail experiments (adapted from Eid et al., 2022) for flows W060, W062, W105 and W108. Specimens were first imparted a pTRM (T1, T2) by cooling down from the Curie point (black curve). Samples were then continuously demagnetised until T1 and cooled down in zero field to monitor the presence of a pTRM tail (red curve). The chosen range (T1, T2) corresponds to the temperature interval of the best fit line in the Arai-Nagata diagram. Tail amplitudes of 4–7% are characteristic of small-size PSD grains (Shcherbakova et al., 2000).

4.3. X-Ray Diffraction

Methods

X-ray diffraction measurements were performed and evaluated by a collaborator at the Geophysical Observatory of Borok. First sample fragments were ground to powder and then the magnetic fraction of the samples was separated by a strong neodymium magnet. A STOE STADI multipurpose X-Ray powder diffractometer was used to measure the magnetic fraction at room temperature. Monochromatized cobalt Kα1 radiation with a wavelength of 0.1788965 nm was emitted by the curved germanium monochromator crystal. During measurements the X-ray beam diffracted on the crystal lattice of the magnetic minerals in certain directions characterised by the Bragg equation (Warren, 1969). The diffracted rays' intensity was measured with respect to the incidence angle of the X-ray beam with a linear position-sensitive detector. "STOE WinXPOW (version 2.23)" and the Crystal Impact Match program were used to process the obtained X-ray diffraction spectra. Observed comparison with the ICDD PDF-2 (version 2008) and COD (version 2016) was the basis for the identification and derivation of the individual phases, their lattice constant, and their abundance.

Results

For both groups, XRD structural analysis on four select specimens reveal two titanomagnetite $Fe_{3-X}Ti_XO_4$ phases: one with lattice parameter a = 8.37–8.38 Å, associated with the dominant T_C; a second with a = 8.40 Å, associated with a secondary T_C present 50–100°C below the dominant T_C (Table 4.4). Using the Nishitani & Kono (1983)'s diagram to deduce the ulvöspinel content x and the oxidation parameter z—fraction of original Fe^{2+} converted to Fe^{3+}—, we find that (i) the two titanomagnetite phases with x = 0.2–0.3 have a low-titanium content; and (ii) group 2 with z = 0.45–0.60 is more oxidised than group 1 with z = 0.30–0.45 (Table 4.4).

Table 4-4: Structural analysis of titanomagnetite $Fe_{3-X}Ti_XO_4$ phases for four select samples: lattice constant *a*; volume fraction *f*; Curie point T_C (deduced from thermomagnetic experiments); ulvöspinel content *x* and oxidation parameter *z* (fraction of original Fe^{2+} converted to Fe^{3+}). The parameters *a* and *f* were determined with a multifunctional powder X-ray diffractometer STOE STADI MP (cobalt $K\alpha_1$ radiation) at the Borok observatory. The parameters x and z were then deduced from a and T_C according to Nishitani & Kono (1983).

Study	Location	Sample	Phase	*a* [Å]	*f* [%]	*Tc* [°C]	*X*	*Z*
Eid et al. (2021)	Waja	W060-0471B	Low Temp.	8.40	0.47	480	0.27	0.30
			High Temp.	8.38	0.53	540	0.20	0.40
		W062-0484B	Low Temp.	8.40	0.38	450	0.35	0.40
			High Temp.	8.37	0.62	560	0.15	0.45
		W105-0820B	Low Temp.	8.40	0.30	430	0.35	0.45
			High Temp.	8.38	0.70	500	0.30	0.55
		W108-0845B	Low Temp.	8.39	0.42	460	0.35	0.55
			High Temp.	8.37	0.58	530	0.25	0.60

4.4. Microscopy

Methods

One sample from each site that underwent API experimentation were polished and observed by Florian Lhuillier at LMU using a Leitz reflective microscope (No. 00618), a Nikon DS-Di3 and the computer program ACT-1 version 2.70 were used to obtain microphotographs of magnetic grains. First the samples were polished according to the following steps (each step was controlled by observing the sample under the microscope):

1) Samples were treated for 15 minutes with SiC Paper FEPA P # 180 to remove scratches caused by cutting.
2) Further treatment for another 15 minutes with the SiC Paper FEPA P # 320 provided the base for finer polishing.
3) A polycrystalline diamond paste with particle diameter of 1 μm was used for 90-120 minutes.
4) A final 30 minutes of treatment with 0.25 μm particle diameter polycrystalline diamond past completed the polishing procedure.

Select polished samples from 4 sites were sent to Borok Geophysical Observatory and measured by a Scanning-electron microscope by Valeri Shcherbakov using a Tescan Vega microscope.

Results

Reflected light microscopy confirms the dichotomy between the two groups. Polished sections from group 1 reveal titanomagnetite (TM) grains with fine ilmenite exsolution lamellae whereas those from group 2 sometimes reveal TM titanomagnetite grains with ilmenite granular exsolution (Figure 4.8). These observations indicate that the TRM from group 1 samples may have been stabilized by high-temperature (i.e., deuteric) oxidation, whereas the remanence from group 2 samples may sporadically have experienced low-temperature (i.e., post-emplacement) oxidation.

Scanning-electron microscopy which indicate that flows W060, W062, W105 and W108 are all characterised by the presence of euhedral to sub euhedral titanomagnetite grains with maximum sizes of ~ 100 μm but also reveal distinctive features (Figure 4.8). Grains from group 1 often show micro-cracks along the margins,

indicative of low-temperature oxidation (Figure 4.8 a and c, e.g. Haggerty, 1991). In contrast, grains from group 2 sometimes show trellis-like intergrowths of ilmenite, pointing to high-temperature oxidation (Figure 4.8 b and d, e.g. Haggerty, 1991) whereas the rest of the grains are homogeneous and unexsolved.

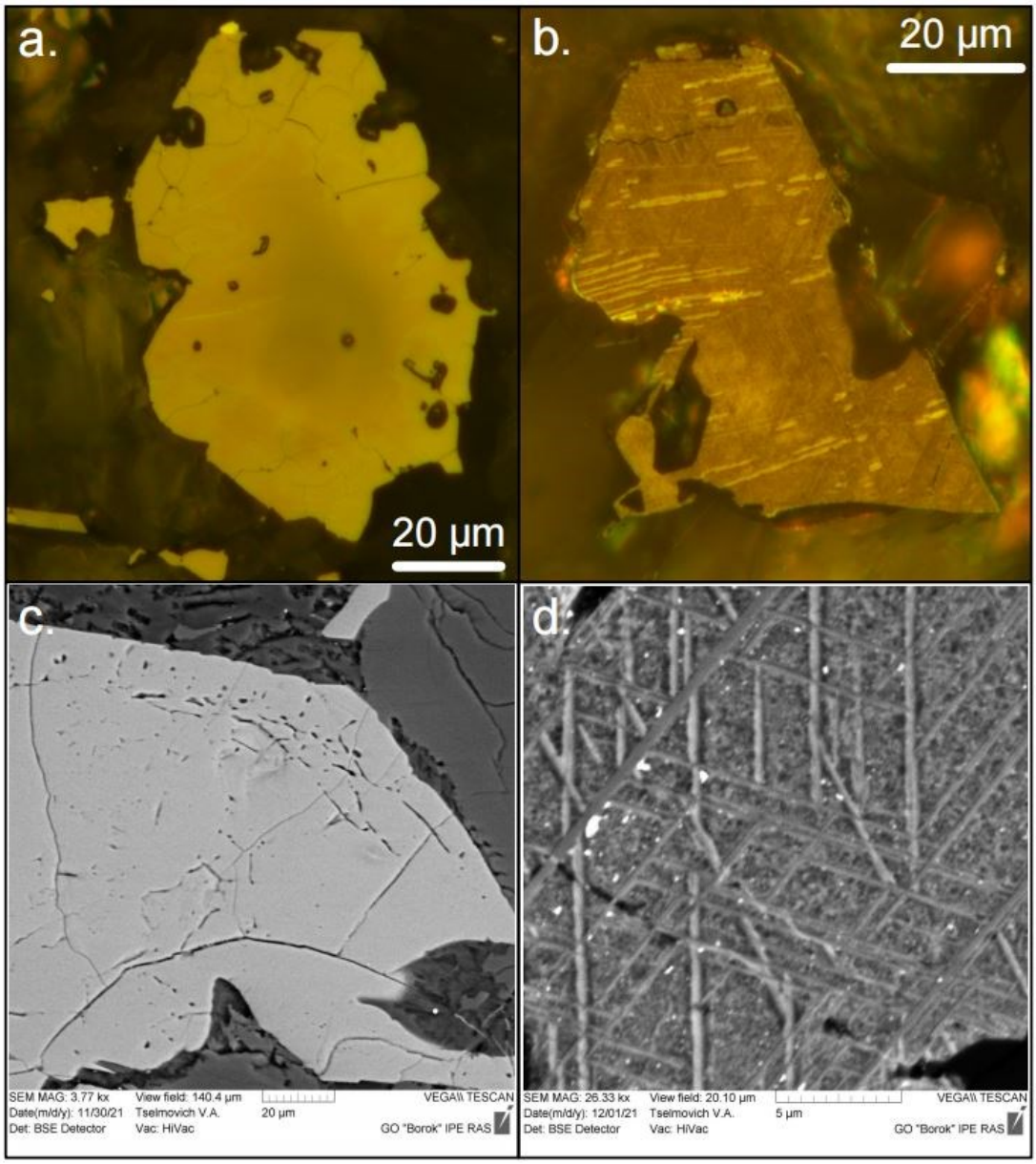

Figure 4.8: Microphotographs of titanomagnetite grains (adapted from Eid et al., 2022) from group 1 (flows W060 and W062. panels a and c) showing micro-cracks suggestive of post-emplacement low-temperature oxidation. and from group 2 (flows W105 and W108. panels b and d) showing trellis-like intergrowths of ilmenite suggestive of deuteric high-temperature oxidation. Reflected-light observations (panels a and b) were conducted in Munich on a Leitz microscope. Scanning-electron observations (panels c and d) were conducted in Borok on a Tescan Vega microscope.

5. Palaeomagnetic Investigation

5.1. NRM Demagnetization

Methods

Stepwise thermal demagnetization was performed at LMU using an ASC TD48 furnace and an AGICO JR6 spinner magnetometer while stepwise alternating field (AF) demagnetization was conducted using the automated Sushibar system based on a custom-made coil and a three-axis, 2G Enterprises cryogenic magnetometer (Wack & Gilder, 2012). The characteristic remanent magnetization of the samples was determined by principal component analysis (Kirschvink, 1980) using the palaeomagnetism.org portal (Koymans et al., 2020). The existence of serial correlation between consecutive lava flows was tested using the algorithm proposed by Chenet et al. (2008). The angular distance δ between the flow-mean directions of each pair of adjacent flows was compared to a threshold value δ_0 given by the quadratic sum of the corresponding α_{95} values. When δ does not exceed δ_0, the mean directions of the adjacent flows are hypothetically correlated, and their individual directions were combined into a single directional group. The pilot samples—2 samples per site—underwent stepwise thermal and alternating field demagnetization. The ChRM directions were indistinguishable in most cases, so the remaining samples were AF demagnetized up to 90 mT (Figure 5.1).

Results

Among the 117 cooling units measured, 20 units were discarded due to erratic demagnetization behaviour and/or high within-unit dispersion (i.e., 95% confidence radius α_{95} >15°). ChRM directions were unambiguously determined by principal component analysis for the remaining 97 units. Ultimately 16 serial correlations were detected —nine with two flows each and seven with three flows each—, leading to a total of 74 independent mean directions (Table 5.1).

To minimise biases from excursional directions a Vandame cut-off was utilized: this was determining by first calculating the angular standard deviation (ASD) of the mean directions which was then plugged into the following equation: cut-off angle = 1.8×ASD° + 5° which produced the cut-off value of 52.3° (Vandamme,

1994). Six of the 74 mean directions, all from the lowermost 216 m of the section, lie outside the cut-off value, These six all have easterly (ca. 90°) declinations with inclinations ranging from 44 to –56° (Table 5.1), yet are not antipodal from the other 68, which together define an average of $D = 6.3°$, $I = 6.4°$ ($\alpha_{95} = 7.4°$), suggesting the six units with easterly declinations are representative of a transitional field, although we cannot discount that they stem from typical secular variation. As these six units do not show any special behaviour in terms of geochemistry, rock-magnetism, or geologic setting, we are confident that the transitional nature of their direction is an integral part of geomagnetic variability.

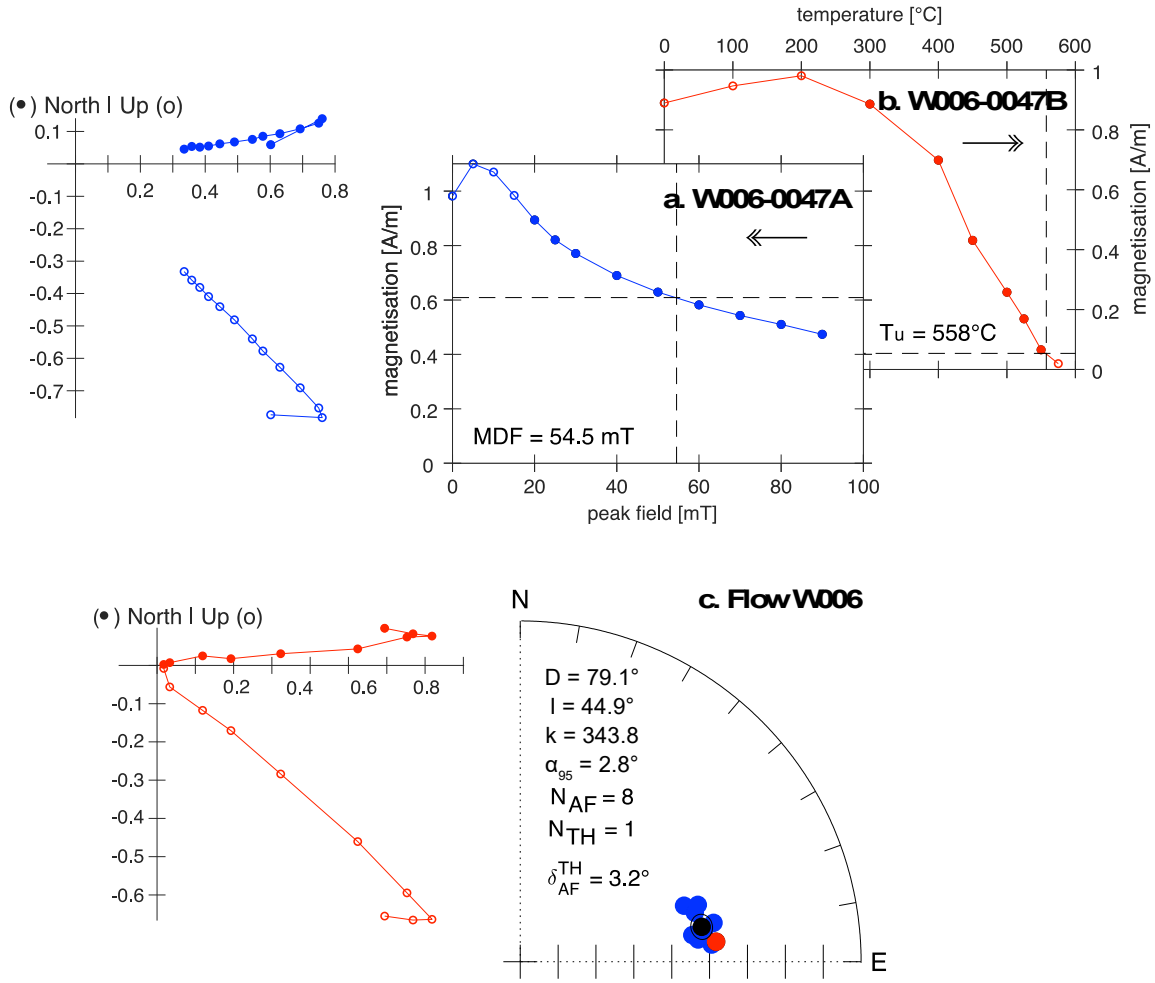

Figure 5.1: Typical demagnetization behaviour of accepted cooling units (adapted from Eid et al., 2021); AF (in blue, N_{AF}) and thermally (in red, N_{TH}) demagnetized sister specimens. (a–c) Flow W006 (2529 m) at the bottom of the section. The equal-area projections (right column) show the intra-site dispersion in geographic coordinates with the mean direction (*D, I*) in black. The parameter *k* (respectively α_{95}) is the Fisher (1953) precision parameter (respectively 95% confidence radius), whereas δ_{TH}^{AF} is the average angular distance between couples of thermally and AF demagnetized specimens. The median destructive field (MDF): the value for which half of the natural remanent magnetization (NRM) is randomized upon AF demagnetization and the unblocking temperature (T_U), the value for which 95% of the NRM is demagnetized upon thermal demagnetization were computed from the decay curves reconstructed by modular subtraction.

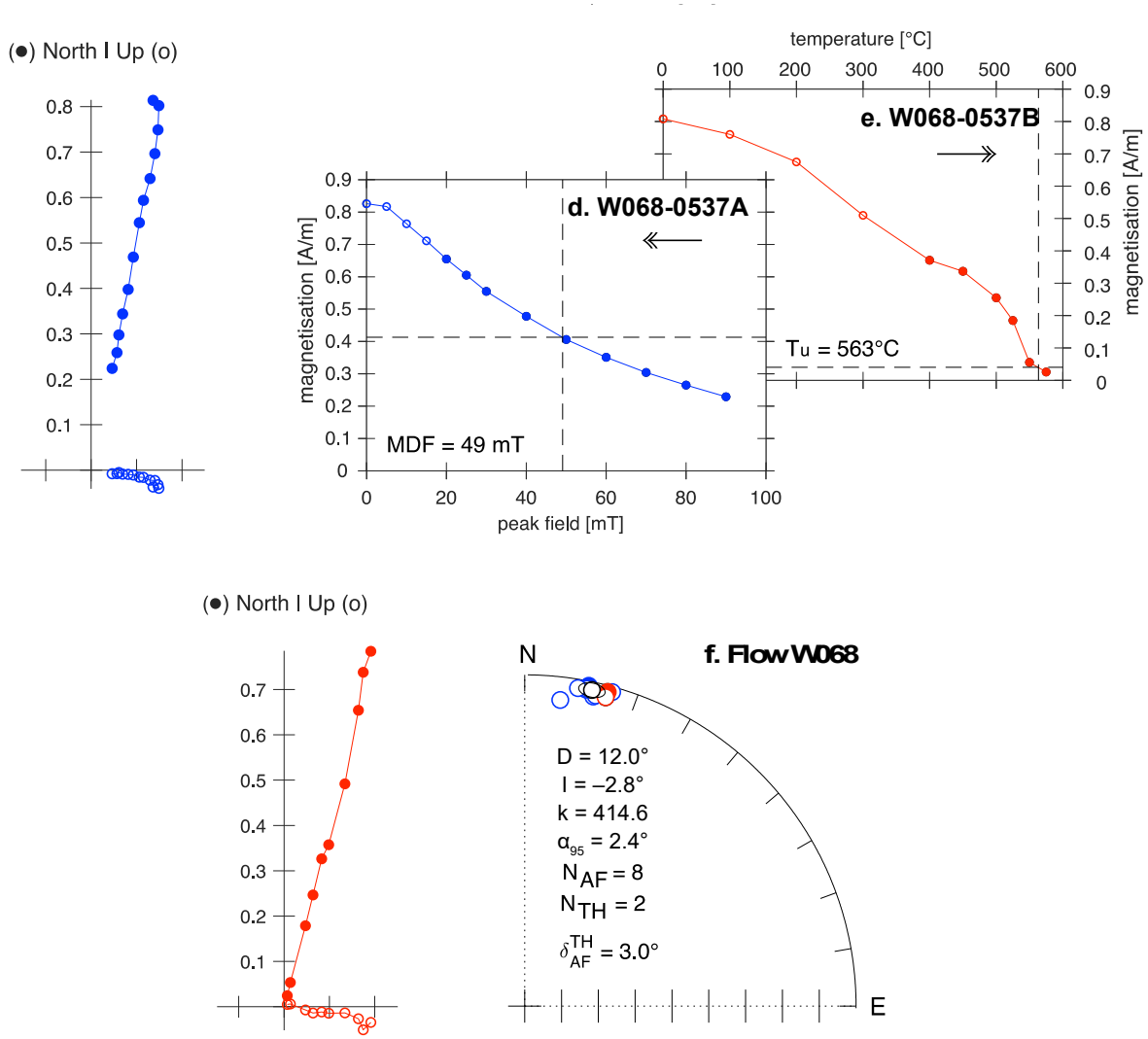

Figure 5.2 (Continued): Typical demagnetization behaviour of accepted cooling units (adapted from Eid et al., 2021); AF (in blue, N_{AF}) and thermally (in red, N_{TH}) demagnetized sister specimens. (d–f) Flow W068 (3019 m) at the middle of the section. The equal-area projections (right column) show the intra-site dispersion in geographic coordinates with the mean direction (*D, I*) in black. The parameter *k* (respectively α_{95}) is the Fisher (1953) precision parameter (respectively 95% confidence radius), whereas δ_{TH}^{AF} is the average angular distance between couples of thermally and AF demagnetized specimens. The median destructive field (MDF): the value for which half of the natural remanent magnetization (NRM) is randomized upon AF demagnetization and the unblocking temperature (T_U), the value for which 95% of the NRM is demagnetized upon thermal demagnetization were computed from the decay curves reconstructed by modular subtraction.

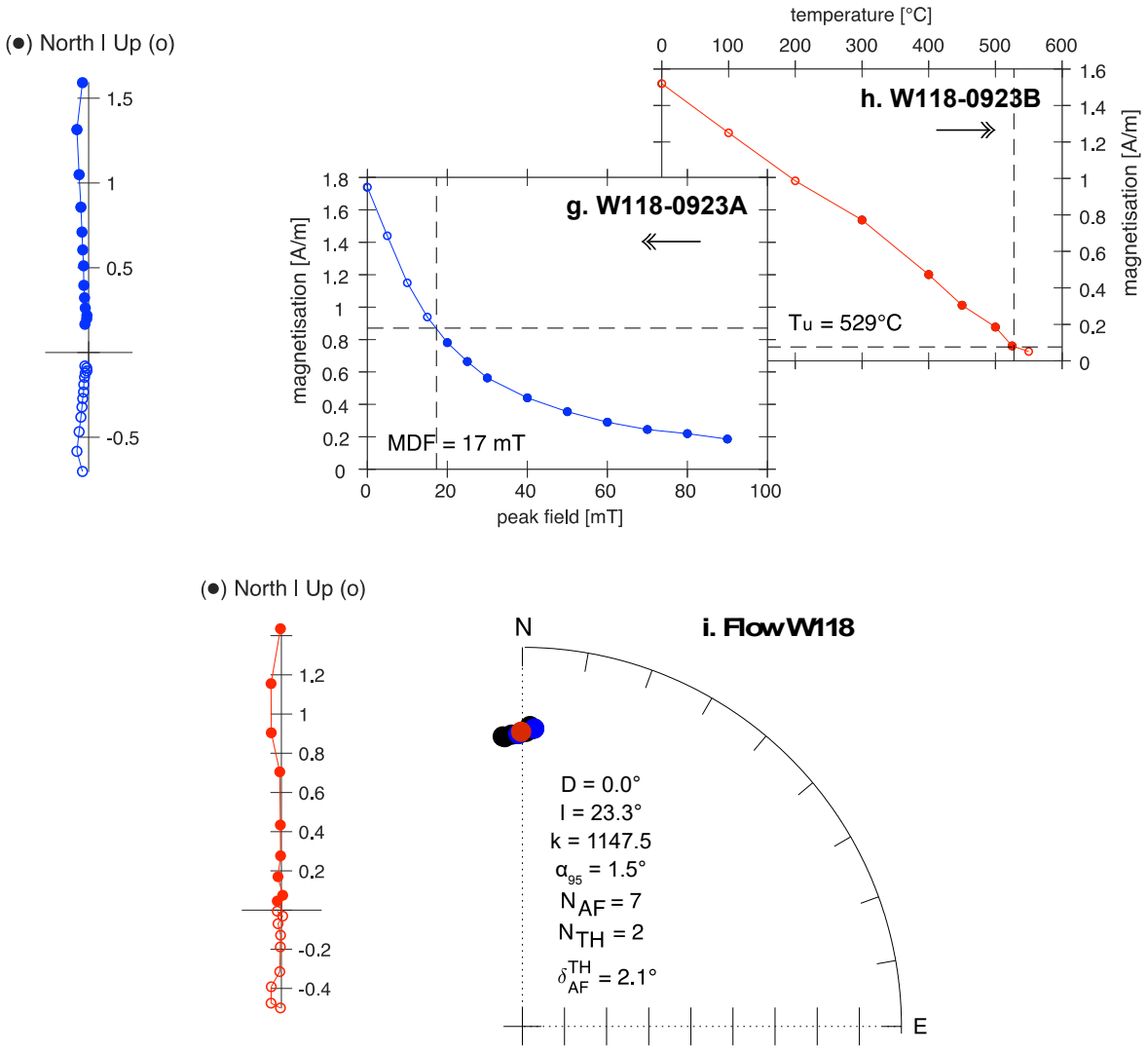

Figure 5.3 (Continued): Typical demagnetization behaviour of accepted cooling units (adapted from Eid et al., 2021); AF (in blue, N_{AF}) and thermally (in red, N_{TH}) demagnetized sister specimens. Flow W118 (3509 m) at the top of the section. The equal-area projections (right column) show the intra-site dispersion in geographic coordinates with the mean direction (*D, I*) in black. The parameter *k* (respectively α_{95}) is the Fisher (1953) precision parameter (respectively 95% confidence radius), whereas δ_{TH}^{AF} is the average angular distance between couples of thermally and AF demagnetized specimens. The median destructive field (MDF): the value for which half of the natural remanent magnetization (NRM) is randomized upon AF demagnetization and the unblocking temperature (T_U), the value for which 95% of the NRM is demagnetized upon thermal demagnetization were computed from the decay curves reconstructed by modular subtraction.

Table 5-1: Palaeomagnetic results for the Waja section: site (or group) name; number (n) of interpreted specimens; number (N) of measured specimens; longitude (Slon), latitude (Slat) and altitude (Alt) of the cooling unit; declination (*Dgeo*) and inclination (*Igeo*) in geographic coordinates with the precision parameter (k) and the 95% confidence radius (α_{95}); longitude (Plon) and latitude (Plat) of the virtual geomagnetic poles. Flows marked with an asterisk (*) were merged into directional groups highlighted in italics. Flows marked with a cross (†) record transitional directions.

Study	Site	n/N	Slat (°)	Slon (°)	Alt (m)	*Dgeo* (°)	*Igeo* (°)	*k*	α_{95} (°)	Plon (°E)	Plat (°N)
Eid et al. (2021)	W003†	8/8	39.44	12.15	2476	108.0	8.1	63.3	7.0	121.4	-16.6
	W004†	8/9	39.44	12.15	2497	90.5	9.3	232.8	3.6	124.8	0.5
	W005*	7/8	39.44	12.15	2516	73.1	42.5	49.6	8.7	107.0	20.9
	W006*	8/8	39.44	12.15	2529	78.4	45.3	362.7	2.9	104.7	15.7
	W005-006†	15/16	-	-	2521	75.9	44.0	91.6	4.0	105.7	18.1
	W008	8/8	39.44	12.15	2542	47.5	-4.6	37.7	9.1	143.4	40.7
	W009	8/8	39.44	12.15	2555	356.5	-5.5	20.3	12.6	232.3	74.8
	W013	5/8	39.43	12.15	2598	44.3	-4.6	230.4	5.1	144.6	43.7
	W014†	8/8	39.43	12.15	2613	101.1	41.0	526.2	2.4	104.0	-5.1
	W018†	7/7	39.43	12.15	2672	93.9	-55.9	126.1	5.4	165.1	-10.1
	W021†	8/8	39.42	12.14	2692	82.9	-40.4	149.6	4.5	153.6	1.7
	W026	7/7	39.42	12.14	2751	38.4	-29.3	47.4	8.9	164.7	42.5
	W027*	5/6	39.42	12.14	2757	348.9	40.3	219.8	5.2	357.2	74.8
	W028*	7/7	39.42	12.14	2760	344.7	36.3	198.7	4.3	340.2	73.2
	W029*	7/7	39.42	12.14	2767	345.8	36.6	344.7	3.3	342.5	74.0
	W027-029	19/20	-	-	2763	346.2	37.5	226.8	2.2	345.2	74.0
	W030	8/8	39.42	12.14	2779	337.2	21.6	165.2	4.3	309.4	67.6
	W031	8/8	39.42	12.14	2768	354.4	31.9	69.7	6.7	353.0	82.4
	W034	8/8	39.41	12.13	2804	28.6	7.4	243.9	3.6	143.6	60.5
	W035*	8/8	39.41	12.13	2822	23.5	14.1	74.7	6.5	139.1	66.3
	W036*	8/8	39.41	12.13	2832	19.3	11.7	112.1	5.3	145.5	69.9
	W035-036	16/16	-	-	2826	21.4	12.9	88.4	3.9	142.0	68.1
	W037	8/8	39.41	12.13	2842	29.0	3.3	193.2	4.0	147.1	59.4
	W038	8/8	39.41	12.13	2838	18.9	3.1	178.1	4.2	157.5	68.5
	W039*	8/8	39.41	12.13	2851	4.1	8.5	422.5	2.7	191.6	81.1
	W040*	7/7	39.41	12.13	2859	3.1	5.7	388.1	3.1	200.6	80.2
	W041*	8/8	39.41	12.13	2864	3.7	7.5	101.9	5.5	195.4	80.9
	W039-041	23/23	-	-	2860	3.7	7.3	208.0	2.1	195.8	80.8
	W042*	9/9	39.41	12.13	2868	18.8	-6.3	154.6	4.2	167.6	65.8

Table 5-1: Continued (1)

Study	Site	n/N	Slat (°)	Slon (°)	Alt (m)	*Dgeo* (°)	*Igeo* (°)	*k*	α_{95} (°)	Plon (°E)	Plat (°N)
Eid et al. (2021)	W043*	8/8	39.41	12.13	2877	19.0	-8.3	208.4	3.8	169.1	65.0
	W044*	8/8	39.41	12.13	2890	20.4	-7.3	208.7	3.8	166.1	64.3
	W042-044	25/25	-	-	2882	19.4	-7.3	194.6	2.1	167.6	65.1
	W045*	8/8	39.41	12.13	2893	8.5	10.2	224.6	3.7	168.2	79.1
	W046*	8/8	39.41	12.13	2902	8.9	5.7	392.4	2.8	175.3	77.2
	W045-046	16/16	-	-	2898	8.7	7.9	242.2	2.4	172.0	78.2
	W048	8/8	39.41	12.13	2903	337.7	-28.3	199.9	3.9	259.1	54.9
	W049	8/8	39.41	12.13	2914	321.4	-11.3	26.7	10.9	286.5	47.7
	W050	8/8	39.41	12.13	2917	344.7	-34.4	337.0	3.0	245.5	55.4
	W051	7/7	39.40	12.13	2933	5.1	31.1	291.6	3.5	84.9	83.2
	W052*	8/8	39.40	12.13	2943	328.4	35.8	251.7	3.5	327.8	58.7
	W053*	6/6	39.40	12.13	2953	324.5	34.4	534.0	2.9	325.1	55.2
	W052-053	14/14	-	-	2948	326.7	35.2	297.9	2.3	326.6	57.2
	W054*	7/8	39.40	12.13	2963	325.1	41.8	92.8	6.3	334.8	54.9
	W055*	8/8	39.40	12.13	2965	326.5	42.7	339.0	3.0	336.1	55.9
	W056*	8/8	39.40	12.13	2967	327.6	44.3	1697.9	1.3	338.6	56.5
	W054-056	23/24	-	-	2966	326.4	43.0	231.7	2.0	336.6	55.8
	W057	8/8	39.40	12.12	2976	323.6	48.6	348.3	3.0	342.6	52.0
	W058	8/8	39.40	12.12	2976	321.3	43.7	431.2	2.7	335.4	51.1
	W059*	8/8	39.40	12.12	2979	347.3	28.8	350.9	3.0	325.7	77.3
	W060*	8/8	39.40	12.12	2989	349.2	29.4	1053.0	1.7	329.8	78.9
	W061*	7/8	39.40	12.12	2994	348.1	32.7	194.0	4.3	337.7	77.1
	W059-061	23/24	-	-	2989	348.2	30.2	318.4	1.7	330.9	77.8
	W062	8/8	39.40	12.12	2999	6.6	29.2	604.1	2.3	100.1	82.7
	W063	8/8	39.40	12.12	3008	352.3	33.7	302.2	3.2	351.5	80.2
	W064	8/8	39.40	12.12	3011	3.7	22.5	318.0	3.1	135.4	86.4
	W065	8/8	39.40	12.12	3013	354.8	27.3	618.7	2.2	335.1	84.4
	W066	9/9	39.40	12.12	3013	347.7	29.6	216.5	3.5	328.4	77.5
	W067	8/8	39.40	12.12	3021	358.6	34.3	863.0	1.9	28.7	83.1
	W068	8/8	39.40	12.12	3019	11.3	-3.2	479.0	2.5	179.4	72.2
	W069	9/9	39.40	12.12	3023	344.5	-8.4	837.0	1.8	263.6	67.6
	W070	7/8	39.40	12.12	3029	351.1	-19.8	660.8	2.4	241.3	66.0
	W071*	8/8	39.40	12.12	3035	6.7	-29.7	239.9	3.6	206.0	61.1
	W072*	8/8	39.40	12.12	3041	7.3	-29.5	446.2	2.6	204.7	61.2
	W071-072	16/16	-	-	3038	7.0	-29.6	333.0	2.0	205.4	61.2
	W073	8/8	39.40	12.12	3049	359.1	-21.5	176.6	4.2	221.9	66.7

Table 5-1: Continued (2)

Study	Site	n/N	Slat (°)	Slon (°)	Alt (m)	*Dgeo* (°)	*Igeo* (°)	*k*	α_{95} (°)	Plon (°E)	Plat (°N)
Eid et al. (2021)	W074	8/8	39.40	12.12	3055	13.8	-31.2	218.7	3.8	193.8	57.9
	W076	8/8	39.40	12.12	3067	31.1	-22.3	373.1	2.9	165.9	51.1
	W075*	7/8	39.40	12.12	3056	21.9	-20.6	625.0	2.4	174.8	58.5
	W077*	7/8	39.40	12.12	3061	23.8	-22.6	1137.5	1.8	173.9	56.4
	W075-077	14/16	-	-	3067	22.8	-21.6	702.8	1.5	174.3	57.5
	W078	8/8	39.40	12.12	3085	38.5	-9.9	326.2	3.1	151.2	48.1
	W079	8/8	39.40	12.12	3094	39.6	-18.2	1542.1	1.4	156.2	45.2
	W080	7/7	39.40	12.12	3107	37.8	49.3	336.1	3.3	96.0	50.6
	W082*	8/8	39.40	12.12	3110	44.6	-16.0	212.2	3.8	151.9	41.2
	W083*	8/8	39.40	12.12	3114	48.8	-15.6	52.6	7.7	149.8	37.4
	W084*	8/8	39.40	12.12	3123	49.5	-18.3	451.3	2.6	150.8	36.3
	W082-084	24/24	-	-	3118	47.6	-16.6	113.6	2.8	150.8	38.3
	W085*	8/8	39.40	12.12	3128	47.1	-12.0	312.8	3.1	148.0	39.7
	W086*	8/8	39.40	12.12	3135	47.9	-10.0	922.1	1.8	146.4	39.4
	W085-086	16/16	-	-	3131	47.5	-11.0	458.9	1.7	147.2	39.6
	W088	8/8	39.40	12.11	3194	13.2	3.4	253.6	3.5	167.0	73.3
	W089*	8/8	39.40	12.11	3208	12.1	9.8	639.0	2.2	159.2	76.0
	W090*	8/8	39.40	12.11	3215	13.9	8.6	189.1	4.0	157.6	74.2
	W089-090	16/16	-	-	3210	13.0	9.2	296.2	2.1	158.4	75.1
	W092	8/8	39.40	12.11	3249	5.2	-28.9	537.7	2.4	208.6	61.9
	W093	6/8	39.40	12.11	3251	26.5	48.3	281.6	4.0	90.2	59.9
	W094	8/8	39.39	12.11	3258	29.3	55.5	202.9	3.9	82.2	54.4
	W095	6/7	39.40	12.11	3281	34.4	60.9	1085.5	2.0	78.1	47.7
	W096	7/8	39.40	12.11	3283	41.6	-5.1	201.2	4.3	146.2	46.1
	W097	8/8	39.40	12.11	3313	12.9	4.8	430.7	2.7	165.5	74.0
	W099*	8/8	39.40	12.11	3343	358.0	9.4	294.2	3.2	234.3	82.4
	W100*	8/8	39.39	12.10	3360	359.7	6.6	307.1	3.2	221.2	81.2
	W099-100	16/16	-	-	3351	358.9	8.0	282.8	2.2	227.3	81.8
	W101	7/7	39.39	12.10	3366	12.3	5.0	154.6	4.9	166.7	74.5
	W102	6/8	39.39	12.10	3371	10.3	30.7	218.4	4.5	104.4	79.0
	W103	8/8	39.39	12.10	3379	5.1	24.0	129.2	4.9	122.7	84.9
	W104*	4/4	39.39	12.10	3384	348.9	-10.1	474.1	4.2	252.8	69.6
	W105*	8/8	39.39	12.10	3386	346.1	-6.0	614.7	2.2	262.6	69.5
	W106*	8/8	39.39	12.10	3399	347.2	-9.4	398.3	2.8	257.2	68.9
	W104-106	20/20	-	-	3388	347.1	-8.2	395.2	1.6	258.5	69.3
	W107	8/8	39.39	12.10	3417	351.8	-32.7	809.3	1.9	234.7	59.0

Table 5-1: Continued (3)

Study	Site	n/N	Slat (°)	Slon (°)	Alt (m)	*Dgeo* (°)	*Igeo* (°)	*k*	α_{95} (°)	Plon (°E)	Plat (°N)
Eid et al. (2021)	W108	8/8	39.39	12.10	3423	5.7	-41.2	56.2	7.4	210.4	53.8
	W109	7/8	39.39	12.10	3436	6.1	-12.6	191.1	4.4	200.9	70.5
	W110	8/8	39.39	12.10	3451	350.7	-27.2	195.1	4.0	238.7	61.9
	W111	8/8	39.39	12.10	3454	345.0	-1.6	110.1	5.3	269.4	70.3
	W112	8/8	39.39	12.10	3462	334.3	19.9	102.5	5.5	307.9	64.7
	W113	7/8	39.39	12.10	3469	16.0	-3.3	184.6	4.5	169.1	68.9
	W114	7/7	39.39	12.10	3478	351.5	-5.3	171.7	4.6	249.7	73.0
	W115	8/8	39.39	12.10	3485	353.7	10.4	142.8	4.7	262.2	80.8
	W116	8/8	39.39	12.10	3488	357.9	21.5	314.7	3.1	285.4	87.7
	W117	8/8	39.39	12.10	3492	354.1	11.9	672.3	2.1	263.6	81.6
	W118	7/7	39.38	12.10	3509	359.5	23.3	1022.0	1.9	317.1	89.5
	W119	8/9	39.38	12.10	3517	23.0	-5.1	46.7	8.2	160.6	62.8

The distribution of stable directions (Figure 5.2 a–b) may be described using the precision parameter (k) and elongation (e). The quantity k is a parameter in Fisher statistics (Fisher, 1953) which represents how close the measurements are to one another—the higher the value of k, the more tightly the values are clustered around their mean. The parameter e was proposed by Tauxe (2018) to quantify the general shape of the distribution—the higher the value of e,the more elongated the shape of the distribution. The distribution of stable directions (Figure 5.2 a) from the Waja section (k = 6.4, e = 1.9, N = 68) differs significantly from the reference distribution (Figure 5.2 b) (k = 17.0, e = 2.7, N = 167) for the whole EYT (Lhuillier & Gilder, 2019), suggesting that the Waja section was emplaced over a duration shorter than ~1 Myr, which is needed to average out secular variation (Lhuillier & Gilder, 2013). The rather smooth variation in the reversal angle θ (angular distance of an individual palaeodirection from the section-mean direction, Figure 5.2 c) suggests that the Waja section likely constitutes a short but continuous record of the Earth's magnetic field, which is consistent with the $^{40}Ar/^{39}Ar$ ages. Focusing on the stable part of the section above 2760 m, the root-mean-square rate of change of θ with respect to elevation h is ~1°/m after smoothing θ with a 10-m rolling average. Note that we chose to quantify secular variation with θ rather than the angular change between directions of

consecutive lava flows as θ is a more robust estimator (i.e., less prone to amplify experimental errors).

Solely normal polarities isolated from all flows within the entire section, combined with a mean $^{40}Ar/^{39}Ar$ age of 31.18 ± 0.28 Ma (Section 3.3), indicate that the Waja section was most likely emplaced during chron C12n (30.98–30.59 Ma; (Ogg, 2020); Figure 5.2 d); chrons C13n (33.73–33.21 Ma) and C11n.2n (30.00–29.53 Ma) can be excluded as they lie outside 95% confidence limits of the radio-isotopic dating. The mean age slightly predates the beginning of chron C12n predicted by the geomagnetic polarity timescale (GPTS; Ogg, 2020), which can be explained by uncertainties on our $^{40}Ar/^{39}Ar$ ages or on the absolute calibration of the GPTS for. Age constraints chron C12n in the GPTS stems from astronomical tuning of an IODP core of sedimentary rocks from the Pacific Ocean (Westerhold et al., 2014). On the other hand, $^{206}Pb/^{238}U$ calibrated sections from North America and Italy yielded dates of 31.28 ± 0.15 and 31.23 ± 0.07 Ma (Sahy et al., 2020), which are fully compatible with our $^{40}Ar/^{39}Ar$ ages.

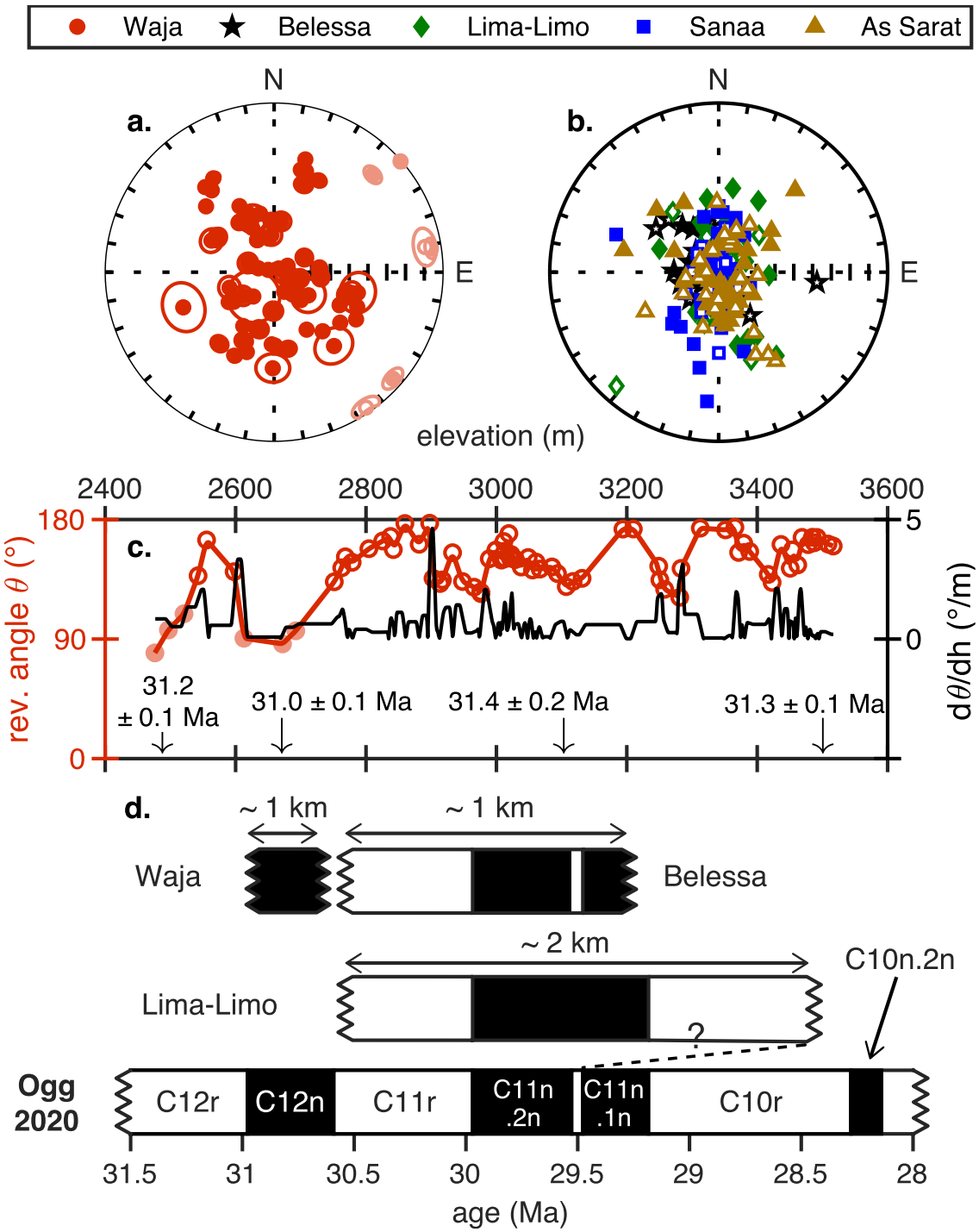

Figure 5.4: palaeomagnetic results (adapted from Eid et al., 2021) (a) directions recentred around the principal axis from the Waja section, (b) recentred directions from Belessa (Lhuillier & Gilder, 2019), Lima-Limo (Rochette et al., 1998), Sanaa (Riisager et al., 2005), and As Sarat (Kellogg & Reynolds, 1983) sections, (c) reversal angle and its rate of change as a function of elevation. Means of the six units with transitional directions are in light red (d) tentative match of the Waja, Belessa, and Lima-Limo sections with the geomagnetic polarity time scale (Ogg, 2020).

5.2. Absolute Palaeointensity

Methods

Twenty-seven out of 119 cooling units were preselected to undergo API measurements based on the following selection criteria:

1) an unambiguous characteristic remanent magnetization (ChRM) in the vector-endpoint diagrams of the TH samples from the directional analysis.
2) A dominant Curie point between 500 and 600°C.
3) Thermostability to within ± 20 per cent of the cyclic *Ms(T)* curves.

We conducted Thellier-style experiments on 140 specimens (8.8-mm or 1-in diameter cores), according to the double-heating protocol of Coe (1967) with partial thermoremanent magnetization (pTRM) checks, using either an ASC-TD48 furnace together with an AGICO JR6 spinner magnetometer or a three-component ORION VSM. In both cases, laboratory fields of 20 μT (50 specimens) and 30 μT (90 specimens) were chosen based on previous knowledge of the EYT (Lhuillier et al., 2019a). To guide the interpretation of the results, we additionally conducted 35 Wilson-style experiments involving comparing the thermal demagnetization curves of the natural remanence magnetization (NRM) and of a thermal remanence magnetization (TRM) induced in a known laboratory field. These domain-state independent experiments are useful to interpret Arai-Nagata diagrams with multiple slopes and, if need be, characterize the single-domain (SD) or multidomain (MD) behaviour of the remanence carriers (Muxworthy, 2010). The final acceptance of the Thellier-style palaeointensities was based on the PICRIT-03 selection criteria (Kissel & Laj, 2004; Paterson et al., 2014)

Results

Amongst the 27 preselected cooling units, only seven yielded interpretable Arai-Nagata diagrams, the others being strongly affected by alteration during experiments. The results from flow W105 are the most satisfactory with a unique slope in the Arai-Nagata diagrams interpreted over 75–86% —interquartile range— of the NRM fraction f (Figure 5.3 c, Table 5.2). In contrast, the Arai-Nagata diagrams from flows W035, W060, W062, W108, W114 and W117 yield two slopes, the steepest one up to 400–500°C (with f = 27–55% for flow W035, 51–65% for the other flows,

interquartile ranges) being interpreted as the hypothetical palaeofield record (Figure 5.3 a, b, and d; Table 5.2). Several arguments tend to suggest that the two-slope nature of the Arai-Nagata diagrams stems from alteration during experiments rather than contamination by MD grains: (i) the pTRM checks often fail for the high-temperature slope; (ii) the vector endpoints of the NRM often deviate from the characteristic direction for the high-temperature slope; (iii) the pTRM tail checks are positive ($DRAT_{tail}$ = 1.4–4.2%, interquartile range) on the chosen temperature interval; and (iv) the domain-state independent Wilson experiments also yield two slopes (Figure 5.3 e, f and h).

To assess the reliability of the Thellier-Coe palaeointensities, we required in the Arai-Nagata diagrams (Nagata et al., 1963) the following conditions: at least four points over the chosen temperature interval T; the NRM fraction for the best fit line, f $\geq$ 0.35; the standard error of the slope normalised by its absolute value, $\beta \leq 0.1$; the quality factor (Coe et al., 1978), $q \geq 2$; the maximum difference ratio measured from pTRM checks (Selkin & Tauxe, 2000), DRAT < 10%; the absolute value of the sum of the pTRM differences (Kissel & Laj, 2004), CDRAT < 10%; and when available, the maximum difference ratio measured from pTRM tail checks (Biggin et al., 2007), $DRAT_{tail}$ < 10%. In the Zijderveld diagrams (Zijderveld, 1967), we required the following two conditions: the mean angular deviation for the free-floating fit (Kirschvink, 1980), MAD < 10%; and the angular difference between the free-floating and anchored best-fit directions, α < 10%. These selection criteria are intermediate between the strict PICRIT03 (Biggin et al., 2007; Kissel & Laj, 2004) and the lenient SELCRIT2 (Biggin et al., 2007) criteria, in their modified version by Paterson et al. (2014).

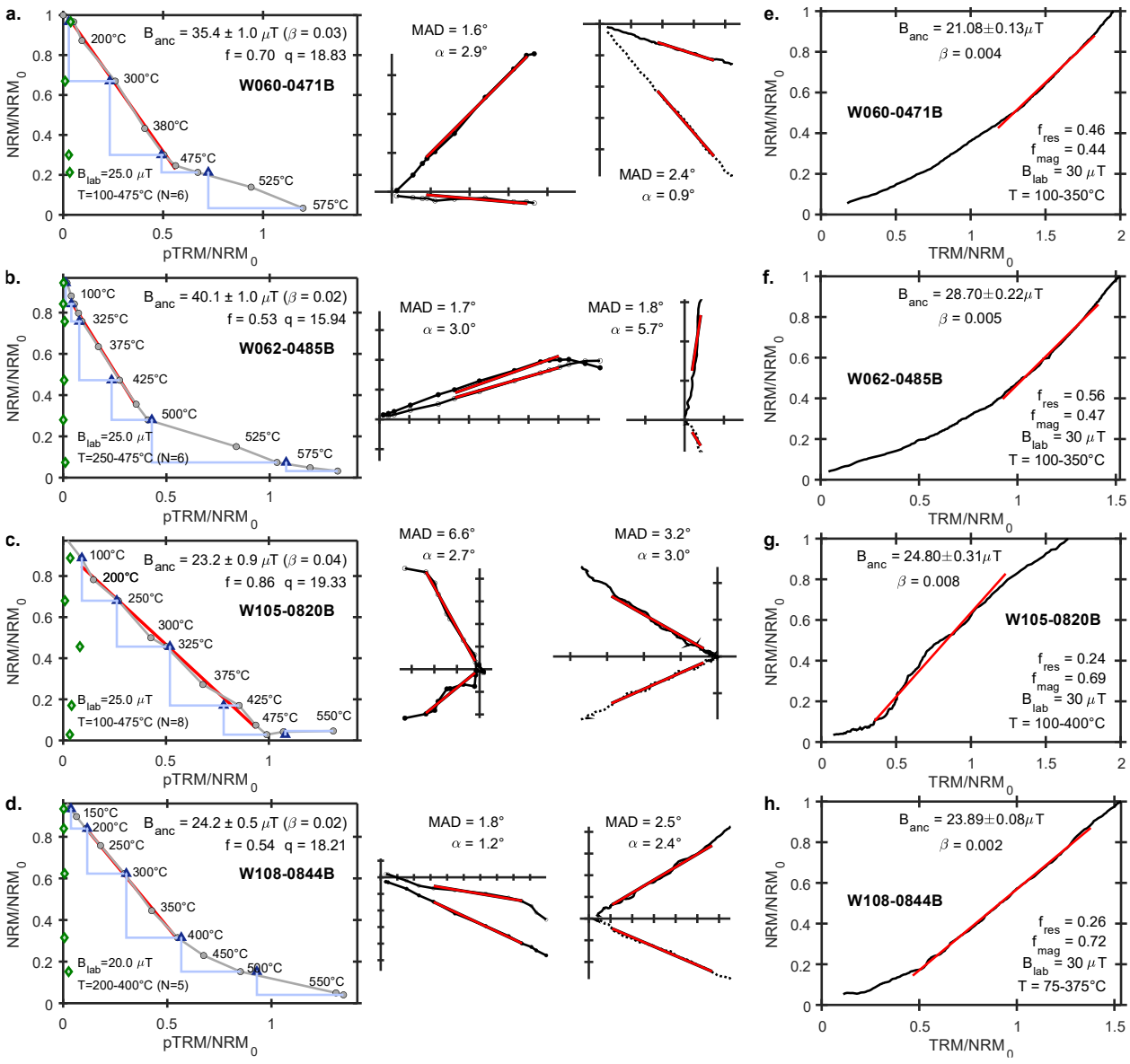

Figure 5.5 Typical accepted absolute palaeointensity results for four flows (adapted from Eid et al., 2022). (a – d) NRM-TRM diagrams with pTRM checks (blue triangle) and pTRM tail checks (green diamonds) obtained from Thellier-Coe experiments. (e – h) NRM-TRM diagrams obtained from Wilson experiments. In both cases. the NRM-TRM diagram is accompanied with the corresponding vector-endpoint diagram in specimen coordinates.

Table 5-2: Accepted specimen level results (Category A); chosen temperature segment ($T_{seg.}$), number of points over T_{int} (n), laboratory field (B_{lab}), absolute palaeointensity and its 1σ error (B_{anc}, σ(B_{anc})), NRM fraction for the best fit line (f), relative standard error of the absolute palaeointensity (β), quality factor (q), maximum difference ratio measured from pTRM checks (DRAT), cumulative DRAT (CDRAT), maximum difference ratio from pTRM tail checks (DRATtail), mean angular deviation for the free-floating fit (MAD) and angular difference between the free-floating and anchored best-fit directions (α).

Study	Sample	$T_{seg.}$ (°C)	n	B_{lab} (mT)	B_{anc} (mT)	σ(B_{anc}) (mT)	f	β	q	DRAT (%)	CDRAT (%)	$DRAT_{tail}$ (%)	MAD (%)	α (%)
Eid et al. (2022)	W060-0466A	200/450	4	20	36.1	0.4	0.42	0.01	21.8	1.0	1.0		2.0	1.2
	W060-0466B	200/450	4	20	37.9	0.4	0.42	0.01	24.1	3.1	3.1		6.7	1.8
	W060-0467A	200/450	4	20	34.4	0.5	0.58	0.01	24.6	1.0	1.0		1.6	0.9
	W060-0468B(1)	100/450	8	20	34.6	1.0	0.70	0.03	20.8	0.6	0.3	1.42	1.8	0.8
	W060-0469B(2)	100/475	6	25	32.4	1.3	0.74	0.04	14.3	2.2	2.3	1.28	2.4	1.8
	W060-0470B(1)	100/475	9	25	33.7	0.9	0.73	0.03	22.9	2.2	4.3	1.74	2.7	1.2
	W060-0471A	200/450	4	20	31.7	1.4	0.53	0.04	7.4	2.0	2.0		3.1	1.7
	W060-0471B(3)	100/475	6	25	35.4	1.0	0.70	0.03	18.8	3.1	5.8	4.30	1.6	1.5
	W062-0482B	200/500	5	20	40.1	1.8	0.68	0.05	9.1	4.3	6.6		2.7	1.8
	W062-0482C	150/425	12	30	38.4	1.9	0.66	0.05	10.8	2.7	6.5		2.3	1.2
	W062-0483B(1)	150/515	10	20	31.2	0.4	0.76	0.01	51.3	6.4	6.6	0.86	1.9	0.9
	W062-0484A	200/500	5	20	35.9	1.3	0.65	0.04	13.2	1.2	0.0		3.4	1.4
	W062-0484B(2)	200/475	6	25	39.2	1.6	0.58	0.04	11.2	1.5	0.2	0.95	3.4	1.8
	W062-0484B	150/425	12	30	39.0	1.0	0.52	0.03	16.5	4.4	7.2		4.4	1.3
	W062-0485B(2)	250/475	6	25	40.1	1.0	0.53	0.02	15.9	2.6	6.0	1.35	1.6	0.9
	W062-0486C(1)	300/500	6	20	38.2	2.5	0.61	0.07	7.1	2.5	7.0	1.48	0.8	1.3
	W062-0487B(1)	200/500	8	20	36.5	1.2	0.56	0.03	14.3	2.0	5.9	0.92	2.4	1.6
	W105-0820A	200/500	5	20	20.5	0.8	0.79	0.04	12.2	8.4	8.8		2.4	1.5
	W105-0820B(3)	100/475	8	25	23.2	0.9	0.86	0.04	19.3	1.5	1.0	6.92	6.6	3.7
	W105-0820B(3)	100/475	8	25	23.2	0.9	0.86	0.04	19.3	1.5	1.0	6.92	6.6	3.7
	W105-0820B	125/475	15	30	24.3	0.8	0.90	0.03	26.0	3.8	5.0		2.9	1.9
	W105-0821A	200/500	5	20	23.9	1.6	0.82	0.06	8.1	8.3	8.2		3.6	2.3
	W105-0821B	200/500	5	20	22.9	0.8	0.81	0.04	15.0	7.1	9.4		1.8	1.6
	W105-0822B(1)	100/400	7	20	28.3	0.9	0.55	0.03	12.6	1.2	1.2	4.44	3.0	0.8
	W105-0823B(1)	100/400	8	20	29.6	0.9	0.64	0.03	17.8	2.4	3.0	1.56	3.0	1.2
	W105-0824B(1)	100/450	8	20	23.4	1.2	0.77	0.05	12.0	3.0	3.0	1.39	2.2	1.2
	W105-0825A	200/500	5	20	24.7	1.1	0.72	0.04	10.8	7.8	8.7		3.2	2.4

Table 5-2: Continued.

Study	Sample	$T_{seg.}$ (°C)	n	B_{lab} (mT)	B_{anc} (mT)	σ(B_{anc}) (mT)	f	β	q	DRAT (%)	CDRAT (%)	$DRAT_{tail}$ (%)	MAD (%)	α (%)
Eid et al. (2022)	W062-0482B	200/500	5	20	23.8	1.0	0.78	0.04	12.2	8.4	9.3		1.7	1.0
	W105-0826C	125/475	15	30	24.9	0.5	0.88	0.02	35.4	3.1	4.3		2.6	1.7
	W108-0844B(1)	200/400	5	20	24.2	0.5	0.54	0.02	18.2	1.3	3.1	1.01	1.8	0.7
	W108-0845A	200/525	6	20	22.1	0.8	0.77	0.04	16.2	3.5	3.6		4.6	2.7
	W108-0845B(2)	100/375	6	25	20.8	0.8	0.45	0.04	8.7	4.3	1.7	5.82	7.5	1.9
	W108-0845B	125/425	13	30	21.5	0.7	0.70	0.03	18.3	3.4	4.7		3.0	1.3
	W108-0847B(1)	100/450	8	20	24.4	0.7	0.72	0.03	20.6	0.7	0.1	3.39	2.4	1.1
	W108-0848B	200/450	4	20	25.1	0.1	0.66	0.00	77.3	0.1	0.1		5.1	2.7
	W108-0849B(1)	100/400	7	15	20.3	0.9	0.56	0.04	11.0	1.0	1.0	2.52	2.7	2.1
	W114-0893B	200/450	4	20	31.0	3.0	0.49	0.10	3.3	1.0	1.0		2.8	4.9
	W114-0897A	200/450	4	30	40.6	1.8	0.49	0.04	6.7	1.0	1.0		3.5	2.6
	W114-0898C(1)	100/450	8	25	28.7	0.6	0.59	0.02	23.2	1.5	2.5	3.94	4.8	1.7
	W117-0919C(1)	150/450	7	20	20.6	0.8	0.68	0.04	12.7	1.7	3.7	2.94	4.4	1.6
	W117-0920B(1)	150/450	9	20	19.7	0.5	0.64	0.03	20.4	4.3	5.1	3.53	1.8	1.0
	W117-0921A	200/450	4	20	24.0	1.9	0.51	0.08	4.1	2.5	2.5		6.1	2.9
	W117-0922A	200/450	4	30	30.1	1.0	0.55	0.03	10.6	4.0	4.0		4.0	1.7

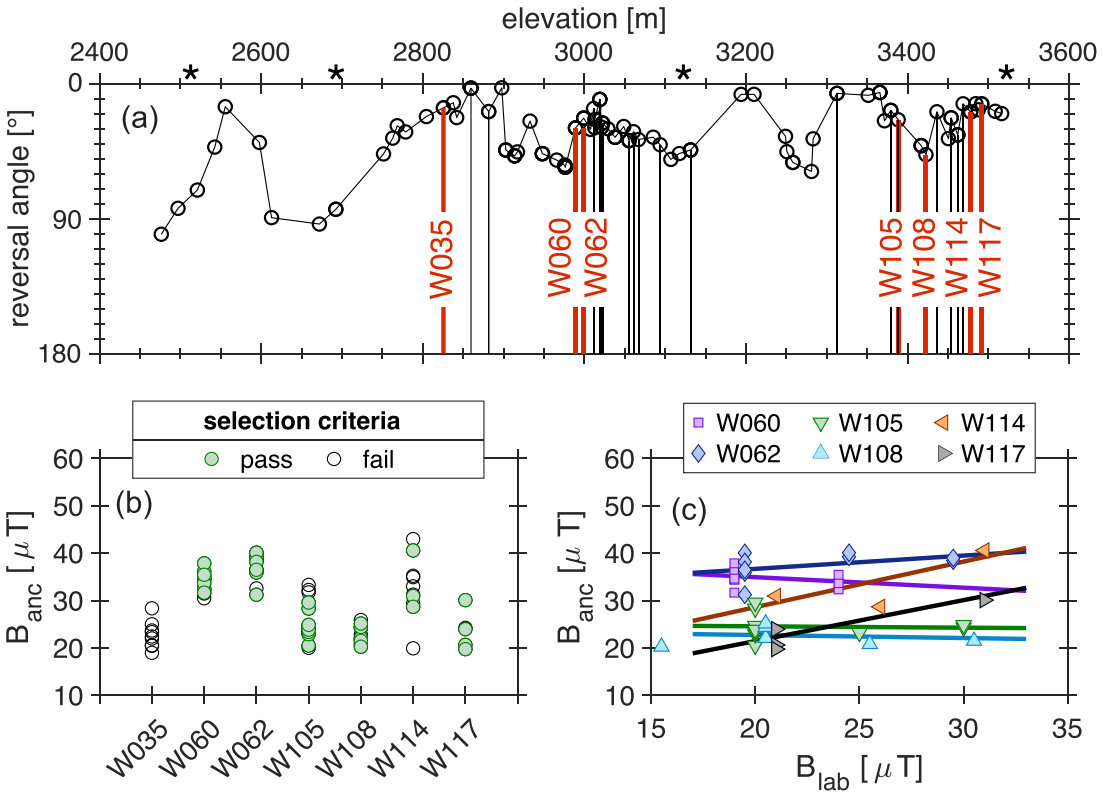

Figure 5.6: Palaeointensity results from the Waja section (adapted from Eid et al., 2022). (a) Reversal angle (angular distance from the section mean direction) as a function of elevation. Black bars represent the preselected flows for API and the red bars represent the interpreted flows. The black asterisks indicate the elevations where $^{40}Ar/^{39}Ar$ determinations were performed, leading to a weighted-mean age of 31.18 ± 0.28 Ma (95% confidence) for the whole section (Eid et al., 2021). (b) Individual API determinations B_{anc} for the seven interpreted lava flows. (c) Dependency of B_{anc} on laboratory field Blab for the specimens passing our selection criteria.

To compute flow-mean API values (Table 5.3), API estimates from multiple specimens were first arithmetically averaged at the sample level. API estimates from multiple samples were then arithmetically averaged at the flow level. Specimens from flow W035 systematically fail to pass our selection criteria, whereas 42 specimens from flows W060, W062, W105, W108, W114 and W117 successfully pass our selection criteria (Figure 5.4, Table 5.2). Amongst the latter flows, W114 and W117 yield the less convincing statistics, with less than five samples satisfying the selection criteria, within-flow relative standard deviation in excess of 15%, and possible

dependency of B_{anc} on B_{lab} (Figure 5.4 c). Consequently, we decided to exclude flows W035, W114 and W117 from our analysis and only retained flows W060, W062, W105 and W108 as potential API records. However, rock-magnetic and microscopy observations provided grounds for excluding the two flows W060 and W062 (sections 3.4 and 4.3) and allowed us to retain only flows W105 and W108 as robust API records.

Table 5-3: Flow-mean API results from the Waja section (31.18 ± 0.28 Ma, 95% confidence; (Eid et al., 2021): number N_{int} (resp. n_{int}) of samples (resp. specimens) used to determine the palaeointensity B_{anc} with standard deviation $\sigma(B_{anc})$ and relative standard deviation β; Virtual Dipole Moment (VDM) provided with its standard deviation σ(VDM); Virtual Axial Dipole Moment (VADM) provided with its standard deviation σ(VADM). Category A specimens pass our selection criteria; category B specimens do not pass our selection criteria (Section 3.5). The two flows marked with an asterisk are those retained for our final interpretation.

Study	Site	Cate.	N_{int}	n_{int}	B_{anc} (µT)	$\sigma(B_{anc})$ (µT)	β (%)	VDM ZAm^2	σ(VDM) ZAm^2	VADM ZAm^2	σ(VADM) ZAm^2
Eid et al. (2021)	W035	B	7	9	22.9	3.0	13.2	57.8	7.6	58.1	7.7
	W060	B	7	12	33.8	1.9	5.7	79.2	4.5	86.0	4.9
	W060	A	6	8	34.3	1.6	4.5	80.2	3.6	87.1	4.0
	W062	B	6	11	37.2	2.8	7.6	87.1	6.6	94.5	7.2
	W062	A	6	9	37.2	3.2	8.5	87.2	7.4	94.6	8.1
	W105	B	8	16	26.2	3.7	14.2	67.4	9.6	66.6	9.5
	W105*	**A**	**7**	**11**	**25.2**	**2.7**	**10.6**	**64.9**	**6.9**	**64.1**	**6.8**
	W108	B	5	10	23.2	1.8	7.8	49.3	3.8	59.0	4.6
	W108*	**A**	**5**	**7**	**23.1**	**2.1**	**9.2**	**49.1**	**4.5**	**58.7**	**5.4**
	W114	B	7	10	33.0	7.6	23.1	85.0	19.6	83.8	19.4
	W114	A	3	3	33.4	6.3	18.9	86.1	16.3	84.9	16.1
	W117	B	4	5	24.1	4.4	18.2	61.2	11.2	61.2	11.1
	W117	A	4	4	23.6	4.7	19.9	60.1	11.9	60.0	11.9

On a general note, the recurrent observation of convex shaped Arai-Nagata diagrams with two distinct slopes often complicates the interpretation of Thellier-style API experiments on volcanic rocks (e.g. Bobrovnikova et al., 2022; Hawkins et al., 2019; Lhuillier et al., 2019a) as it can result from multiple causes such as (i) the

presence of two NRM components, (ii) the presence of non-ideal MD remanence carriers (e.g. Calvo et al., 2002; Kosterov & Prévot, 1998; Levi, 1977; Shcherbakov & Shcherbakova, 2001; Xu & Dunlop, 2004), (iii) the presence of SD-like remanence carriers bearing a TCRM produced by grain-volume growth (e.g. Gribov et al. 2021; Shcherbakov et al. 2021), (iv) the insufficient averaging of PSV for slowly cooled units (e.g. Shcherbakov et al., 2021), or (v) thermal alteration in the course of double heating experiments. In this study, we think that the two-slope Arai-Nagata diagrams observed for flows W035, W060 and W062 are likely the consequence of non-ideal TCRMs produced by grain volume growth, in opposition to TCRMs produced by T_C increase that are indistinguishable from pure TRMs and preserves the linearity of the remanence acquisition process (e.g. Shcherbakov et al., 2019, 2021).

In terms of qualitative reliability factors (QPI; Biggin & Paterson, 2014; Hawkins et al., 2021; Kulakov et al., 2019), flows W105 and W108 are well-dated with $^{40}Ar/^{39}Ar$ ages (Q_{AGE} = 1), carry a stabilised thermally activated remanence (QTRM = 1), and yield well defined palaeodirections (Q_{DIR} = 1). Their Thellier-style determinations are statistically well constrained (Q_{STAT} = 1), not contaminated by alteration (Q_{ALT} = 1) nor MD effect (Q_{MD} = 1). Conducted on thin, rapidly cooled basaltic flows, the API estimates do not need a cooling rate correction, do not show obvious signs of anisotropy (γ = 2.9–4.5◦, interquartile range; (Paterson, 2013) or of non-linear field acquisition (Figure 5.4 c; Q_{ACN} = 1). The Thellier-style determinations are consistent with Wilson-style determinations (Q_{TECH} = 1) and the measurement-level data are available for inspection (Q_{MAG} = 1), thus reaching a QPI score of 9/10. In contrast, the Thellier-style determinations from flows W060 and W062 are likely impaired by low-temperature oxidation (Q_{TRM} = 0) and anisotropy (γ = 2.8–9.0◦, interquartile range; Q_{ACN} = 0), are inconsistent with Wilson-style determinations (Q_{TECH} = 0), thus reaching a QPI score of 6/10.

5.3. Relative Palaeointensity

Methods

Based on the following criteria 29 flows were preselected to undergo RPI measurements:

1) An unambiguous ChRM in the vector-endpoint diagrams of the AF demagnetized samples from the directional analysis.
2) An average median destructive field higher than 20 mT.

To investigate the RPI, we conducted pseudo-Thellier experiments (Tauxe et al., 1995; Yu et al., 2003) on 230 specimens using the automated Sushibar system based on a custom-made coil and a three-component 2G enterprises cryogenic magnetometer (Wack & Gilder, 2012). The first stage involves the three-axis stepwise AF demagnetization of a specimen's NRM, the second stage the stepwise acquisition of an anhysteretic remanent magnetization (ARM, with a bias field of 20 μT in our case), and the third stage the one-axis stepwise AF demagnetization of the last imparted ARM. We performed the experiments in 5 mT steps up to 30 mT, in 10 mT steps up to 90 mT. To account for the variable amounts of NRM remaining after 90 mT, were moved the residual magnetization from all remanence data (Lhuillier et al., 2017b; Meng et al., 2020). The reliability of the RPI determinations is discussed in the framework of the selection criteria defined by Paterson et al. (2016) and the grain-size indicator $B_{1/2}^{ARM}$ —the AF field for which half of the maximum ARM is imparted— introduced by de Groot et al. (2013).

Results

To determine the pseudo-Thellier slope, we chose a constant AF segment (15–40 mT for the lower bound, 60–80 mT for the upper bound) for all 7–9 specimens of each investigated flow (Figure 5.5, Table 5.4). We first applied selection criteria at the specimen level: correlation coefficient $R_C^2 > 0.95$, relative standard error $\beta \leq 0.10$ and NRM fraction $f \geq 0.30$ in the pseudo-Arai diagram; ARM residual fraction —defined as the x-intercept of the linear fit— $f_{res} \leq 0.40$ in the demag-demag diagram; grain-size indicator B_{12}^{ARM} in the range 17–60 mT. Then, we only retained the flows with at least three determinations and a standard deviation ≤ 0.75, leading us to a set of 106 accepted RPI estimates scattered amongst 19 flows (Figure 5.6 b, Table 5.4).

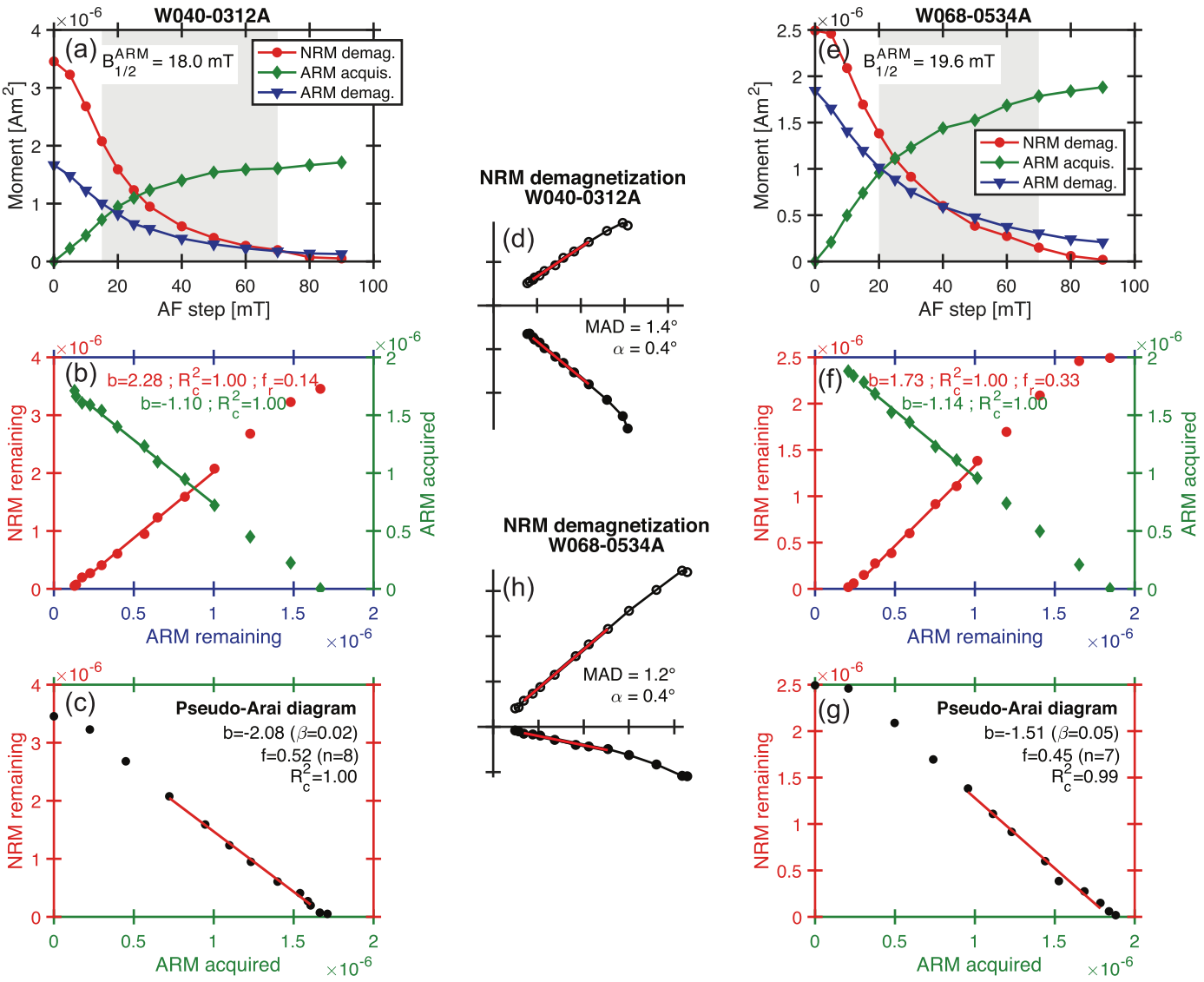

Figure 5.7 Typical relative palaeointensity results using the pseudo-Thellier method (adapted from Eid et al., 2022). (a & e) Evolution of dipole moment during the three stages of the experiment. (b & f) Combined demag-demag and ARM-ARM diagrams. (c & g) Pseudo-Arai diagrams with relative palaeointensity estimate b and normalised standard error β. (d & h) Vector-endpoint diagrams of the NRM.

Table 5-4: Accepted flow-mean relative palaeointensity results: pseudo-Thellier slope (b) and its standard deviation (sb); Specimen level results Pseudo-Thellier slope (b_{PT}) and their standard deviation (sb_{PT}) with their parameters: chosen AF segment ($AF_{seg.}$), number of points over AFseg (n), grain size indicator(B_{12}^{ARM}); from the pseudo-Arai diagram: correlation coefficient (R_C^2), relative standard error (β), NRM fraction for the best fit line (f); from the demag-demag diagram: ARM residual fraction (f_{res}).

Study	Flow	b	sb	Sample	b_{PT}	sb_{PT}	$AF_{seg.}$ (mT)	n	B_{12}^{ARM} (mT)	R_C^2	β	f	f_{res}
Eid et al. (2022)	W021	0.46	0.19	0160A	-0.36	0.03	20/70	7	18.5	0.98	0.07	0.36	0.36
				0163A	-0.33	0.03	20/70	7	18.1	0.96	0.09	0.36	0.31
				0166A	-0.68	0.04	20/70	7	23.7	0.98	0.06	0.42	0.34
	W030	0.70	0.10	0226A	-0.88	0.04	25/70	6	48.8	0.99	0.05	0.51	0.13
				0227A	-0.64	0.02	25/70	6	43.2	1.00	0.03	0.51	0.25
				0229A	-0.66	0.04	25/70	6	28.1	0.98	0.06	0.37	0.30
				0230A	-0.66	0.06	25/70	6	37.6	0.97	0.09	0.44	0.10
				0231A	-0.75	0.07	25/70	6	44.6	0.97	0.09	0.49	0.18
				0233A	-0.62	0.04	25/70	6	44.7	0.98	0.07	0.44	0.20
	W040	1.94	0.09	0309A	-1.92	0.05	15/70	8	18.6	1.00	0.03	0.53	0.18
				0310A	-1.88	0.03	15/70	8	18.9	1.00	0.01	0.58	0.17
				0311A	-1.88	0.03	15/70	8	17.2	1.00	0.02	0.51	0.15
				0312A	-2.08	0.04	15/70	8	18.0	1.00	0.02	0.52	0.14
	W048	1.67	0.33	0371A	-1.28	0.03	20/70	7	17.7	1.00	0.03	0.42	0.23
				0372A	-1.81	0.03	20/70	7	26.2	1.00	0.02	0.54	0.18
				0373A	-1.91	0.03	20/70	7	22.9	1.00	0.02	0.50	0.18
	W049	2.54	0.52	0379A	-2.63	0.05	15/70	8	22.9	1.00	0.02	0.60	0.22
				0380A	-2.78	0.11	15/70	8	29.9	0.99	0.04	0.75	0.28
				0381A	-2.84	0.11	15/70	8	29.9	0.99	0.04	0.75	0.28
				0382A	-1.95	0.05	15/70	8	18.0	1.00	0.03	0.50	0.12
				0384A	-1.88	0.03	15/70	8	17.1	1.00	0.01	0.49	0.14
				0385A	-3.16	0.09	15/70	8	30.4	1.00	0.03	0.74	0.31
	W052	1.88	0.39	0401A	-1.49	0.04	25/80	7	20.7	1.00	0.02	0.39	0.17
				0402A	-1.30	0.02	25/80	7	22.0	1.00	0.02	0.41	0.19
				0404A	-2.00	0.06	25/80	7	23.1	1.00	0.03	0.44	0.20
				0405A	-2.04	0.06	25/80	7	24.0	1.00	0.03	0.44	0.17
				0406A	-2.15	0.06	25/80	7	24.4	1.00	0.03	0.45	0.09
				0408A	-2.30	0.09	25/80	7	22.9	0.99	0.04	0.40	0.10

Table 5-4: Continued (1).

Study	Flow	b	sb	Sample	b_{PT}	sb_{PT}	$AF_{seg.}$ (mT)	n	B_{12}^{ARM} (mT)	R_C^2	β	f	f_{res}
Eid et al. (2022)	W053	2.00	0.48	0409A	-1.97	0.05	25/80	7	27.2	1.00	0.03	0.46	0.06
				0410A	-2.69	0.06	25/80	7	27.8	1.00	0.02	0.48	0.18
				0412A	-2.24	0.11	25/80	7	26.2	0.99	0.05	0.46	0.16
				0415A	-1.52	0.03	25/80	7	30.7	1.00	0.02	0.56	0.33
				0416A	-1.61	0.03	25/80	7	30.3	1.00	0.02	0.54	0.31
	W057	3.32	0.42	0441A	-3.25	0.16	20/70	7	26.2	0.99	0.05	0.54	0.35
				0442A	-3.55	0.17	20/70	7	26.7	0.99	0.05	0.55	0.34
				0443A	-2.78	0.09	20/70	7	23.0	0.99	0.03	0.49	0.28
				0444A	-2.64	0.13	20/70	7	21.2	0.99	0.05	0.47	0.26
				0445A	-3.48	0.19	20/70	7	28.1	0.98	0.05	0.57	0.36
				0446A	-3.39	0.17	20/70	7	29.0	0.99	0.05	0.58	0.37
				0447A	-3.72	0.15	20/70	7	29.3	0.99	0.04	0.57	0.32
				0448A	-3.78	0.14	20/70	7	30.7	0.99	0.04	0.59	0.33
	W058	3.03	0.60	0449A	-3.51	0.13	20/60	6	23.9	0.99	0.04	0.44	0.30
				0450A	-3.92	0.15	20/60	6	24.0	0.99	0.04	0.46	0.31
				0451A	-3.08	0.19	20/60	6	22.9	0.99	0.06	0.47	0.37
				0454A	-2.43	0.06	20/60	6	17.5	1.00	0.02	0.38	0.28
				0455A	-2.80	0.12	20/60	6	19.5	0.99	0.04	0.42	0.40
				0456A	-2.44	0.12	20/60	6	19.0	0.99	0.05	0.41	0.33
	W060	1.81	0.16	0465A	-1.65	0.05	25/70	6	34.1	1.00	0.03	0.60	0.30
				0466A	-1.66	0.06	25/70	6	34.6	0.99	0.04	0.62	0.33
				0467A	-1.98	0.06	25/70	6	28.5	1.00	0.03	0.45	0.12
				0468A	-1.94	0.05	25/70	6	27.8	1.00	0.03	0.45	0.11
				0469A	-1.90	0.07	25/70	6	28.9	1.00	0.03	0.44	0.09
				0470A	-1.98	0.09	25/70	6	28.8	0.99	0.05	0.43	0.08
				0471A	-1.69	0.04	25/70	6	30.1	1.00	0.02	0.50	0.17
				0472A	-1.64	0.04	25/70	6	30.2	1.00	0.03	0.49	0.15
	W062	1.58	0.07	0482A	-1.52	0.07	25/70	6	36.6	0.99	0.05	0.63	0.24
				0483A	-1.50	0.06	25/70	6	37.5	0.99	0.04	0.64	0.25
				0484A	-1.67	0.10	25/70	6	38.8	0.99	0.06	0.70	0.40
				0485A	-1.58	0.10	25/70	6	38.2	0.98	0.06	0.69	0.36
				0486A	-1.63	0.09	25/70	6	38.1	0.99	0.06	0.69	0.36

Table 5-4: Continued (2).

Study	Flow	b	sb	Sample	b_{PT}	sb_{PT}	$AF_{seg.}$ (mT)	n	B_{12}^{ARM} (mT)	R_C^2	β	f	f_{res}
Eid et al. (2022)	W068	1.58	0.27	0530A	-1.49	0.04	20/70	7	20.9	1.00	0.03	0.45	0.31
				0531A	-1.38	0.03	20/70	7	20.2	1.00	0.02	0.46	0.34
				0532A	-1.35	0.03	20/70	7	19.2	1.00	0.02	0.43	0.35
				0533A	-1.37	0.04	20/70	7	17.6	1.00	0.03	0.38	0.24
				0534A	-1.51	0.08	20/70	7	19.6	0.99	0.05	0.45	0.33
				0535A	-1.96	0.03	20/70	7	25.2	1.00	0.02	0.49	0.35
				0537A	-1.98	0.04	20/70	7	24.6	1.00	0.02	0.46	0.31
	W069	2.18	0.25	0538A	-1.81	0.02	20/70	7	23.6	1.00	0.01	0.48	0.25
				0539A	-1.98	0.05	20/70	7	24.1	1.00	0.02	0.47	0.21
				0540A	-2.28	0.10	20/70	7	20.6	0.99	0.04	0.42	0.15
				0541A	-2.47	0.09	20/70	7	21.5	0.99	0.04	0.43	0.16
				0542A	-2.48	0.07	20/70	7	25.5	1.00	0.03	0.51	0.17
				0543A	-2.30	0.05	20/70	7	25.7	1.00	0.02	0.49	0.22
				0544A	-2.11	0.08	20/70	7	19.2	0.99	0.04	0.40	0.15
				0546A	-2.00	0.08	20/70	7	18.7	0.99	0.04	0.40	0.15
	W071	2.61	0.57	0555A	-2.34	0.05	25/80	7	34.0	1.00	0.02	0.58	0.30
				0556A	-2.57	0.08	25/80	7	34.2	1.00	0.03	0.56	0.30
				0557A	-2.76	0.07	25/80	7	33.2	1.00	0.03	0.56	0.29
				0558A	-3.21	0.09	25/80	7	33.9	1.00	0.03	0.56	0.28
				0559A	-3.09	0.09	25/80	7	30.9	1.00	0.03	0.55	0.28
				0560A	-3.18	0.05	25/80	7	32.2	1.00	0.01	0.56	0.32
				0561A	-2.07	0.04	25/80	7	31.3	1.00	0.02	0.54	0.26
				0562A	-1.63	0.14	25/80	7	31.9	0.96	0.09	0.64	0.27
	W074	1.24	0.11	0579A	-1.41	0.08	30/80	6	28.0	0.99	0.06	0.40	0.18
				0580A	-1.17	0.04	30/80	6	32.2	1.00	0.03	0.48	0.26
				0581A	-1.25	0.08	30/80	6	30.7	0.99	0.06	0.45	0.23
				0582A	-1.12	0.03	30/80	6	34.2	1.00	0.02	0.52	0.30
				0583A	-1.23	0.04	30/80	6	35.4	1.00	0.03	0.53	0.29
	W086	1.06	0.06	0675A	-1.00	0.03	20/70	7	25.1	1.00	0.03	0.53	0.26
				0676A	-1.01	0.05	20/70	7	25.2	0.99	0.05	0.55	0.25
				0677A	-1.13	0.04	20/70	7	24.9	0.99	0.03	0.54	0.27
				0678A	-1.11	0.04	20/70	7	24.5	0.99	0.03	0.55	0.28
				0679A	-1.14	0.04	20/70	7	25.0	0.99	0.03	0.51	0.17
				0680A	-1.03	0.06	20/70	7	21.9	0.98	0.05	0.49	0.21
				0681A	-1.00	0.06	20/70	7	21.9	0.98	0.06	0.47	0.17

Table 5-4: Continued (3).

Study	Flow	b	sb	Sample	b_{PT}	sb_{PT}	$AF_{seg.}$ (mT)	n	B_{12}^{ARM} (mT)	R_C^2	β	f	f_{res}
Eid et al. (2022)	W101	2.69	0.07	0796A	-2.61	0.22	30/80	6	34.7	0.97	0.08	0.51	0.36
				0797A	-2.75	0.20	30/80	6	34.5	0.98	0.07	0.51	0.29
				0798A	-2.71	0.17	30/80	6	34.2	0.98	0.06	0.50	0.34
	W107	1.31	0.26	0835A	-1.26	0.09	25/60	5	35.2	0.98	0.08	0.50	0.29
				0836A	-1.08	0.07	25/60	5	33.1	0.99	0.06	0.49	0.22
				0837A	-1.68	0.11	25/60	5	34.0	0.99	0.07	0.51	0.23
				0838A	-1.23	0.06	25/60	5	30.5	0.99	0.05	0.44	0.13
	W112	1.67	0.37	0879A	-1.50	0.08	25/70	6	20.8	0.99	0.06	0.36	0.14
				0880A	-1.24	0.08	25/70	6	20.5	0.98	0.06	0.36	0.21
				0881A	-1.93	0.10	25/70	6	20.4	0.99	0.05	0.34	0.15
				0882A	-2.03	0.13	25/70	6	21.5	0.98	0.07	0.36	0.17

We a posteriori checked that the pseudo-Thellier slope does not correlate with the selection parameters (Figure 5.6 c). A peculiarity of the present dataset are the high values of f_{res} (mean value around 25%) whereas this quantity should theoretically tend towards zero (Paterson et al., 2016). This can be either explained by experimental errors (e.g. misalignment of the specimens) as the ARM demagnetization was only performed in the z-direction or by physical causes such as ARM anisotropy, the presence of a pARM tail or magnetostatic interactions between the investigated ARM fraction and the residual NRM. However, as f_{res} does not correlate with the pseudo-Thellier slope, its high values have probably no influence on the reliability of the RPI determinations. Based on the 19 accepted flow mean palaeointensities, we obtained by bootstrap experiments (10,000 trials) the estimate $\varepsilon_F = 0.39 \pm 0.07$ (1σ) for the RPI, defined as the ratio of the standard deviation to the mean of the palaeointensities.

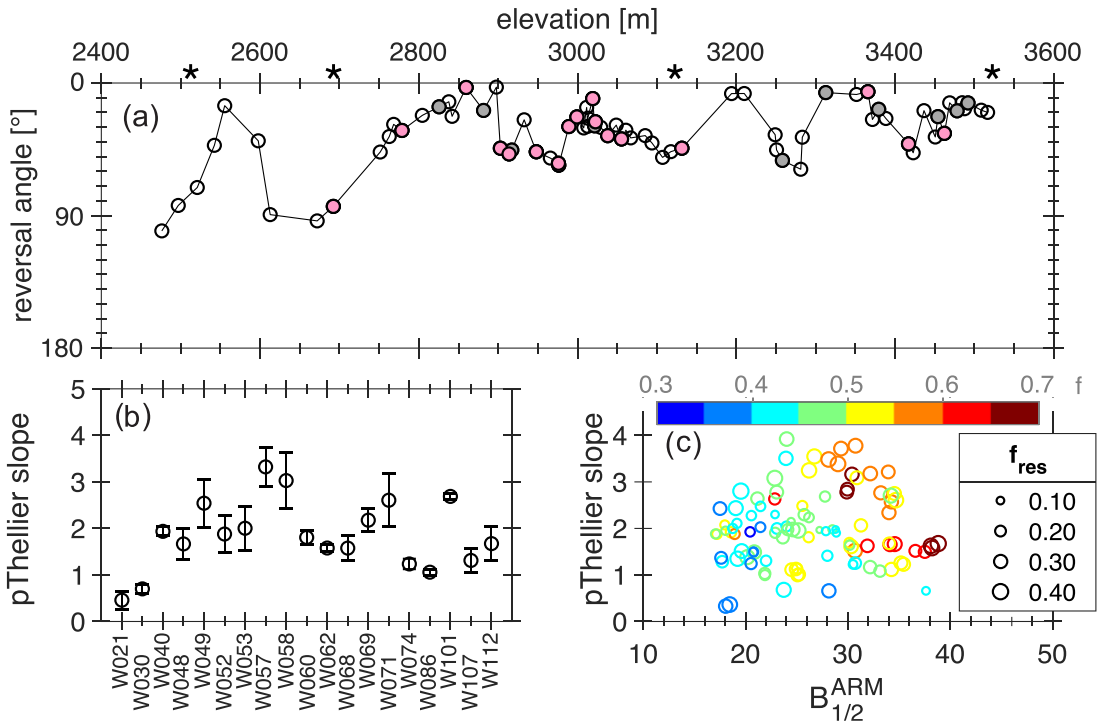

Figure 5.8 Relative palaeointensity results from the Waja section (adapted from Eid et al., 2022). (a) Reversal angle (angular distance from the section-mean direction) as a function of elevation. Grey discs represent the preselected flows while the pink discs represent the interpreted flows for RPI. The black asterisks indicate the elevations where $^{40}Ar/^{39}Ar$ determinations were performed. leading to a weighted-mean age of 31.18 ± 0.28 Ma (95% confidence) for the whole section (Eid et al., 2021). (b) Average RPI determinations (±1σ) for the 19 accepted lava flows. (c) Dependency of accepted RPI determinations on grain-size indicator $B_{1/2}^{ARM}$. NRM fraction f (colour of the circles). residual fraction f_{res} of ARM at the end of the experiment (size of the circles).

5.4. World Palaeointensity Database

In addition to the API results described in section 5.2, I was involved in obtaining API results from two other sections. The first was the Tuoyun section from the Tian Shan province in China (Meng et al., 2020) which produced four robust API records during the Paleocene. The second was the Chukotka section from the Chukotka-Okhotsk Volcanic Belt in far eastern Russia (Bobrovnikova et al., 2022) which produced two reliable API records during the Cretaceous.

To analyse the evolution of the dipole moment over the past 155 Myr, we updated the WPD (Shcherbakov & Sycheva, 2006, 2013) by scanning new publications available on the Web of Science since 2015. The WPD, maintained by the Borok Geophysical Observtory (BGO) and the LMU, contains all known results in terms of reconstructed dipole strength—virtual dipole moment (VDM) or virtual axial dipole moment (VADM) when palaeoinclination is unknown—obtained from igneous or baked rocks, irrespective of the chosen API method. Its last version lists 409 publications for a total of 5420 palaeointensity records. API measurements have been obtained from various locations on Earth and to be able to compare them to one another they need to first be expressed in terms of VDM or VADM. Assuming that the Earth's magnetic field is approximated as a geocentric axial dipole then magnetic field intensity measured at any point on Earth (API) could be used to calculate the dipole strength in terms of VDM (if the inclination is known) or VADM (if the inclination is unknow).

For our analysis, we only retained the most robust API records obtained from Thellier-style experiments with pTRM checks, i.e., offering a self-consistent reliability assessment and relying on a proven theory (e.g. Dunlop, 2011; Shcherbakov et al., 2021). Additionally, strengthening the selection criteria proposed by Perrin & Shcherbakov (1997), we only retained the API records derived from at least 5 individual determinations and a relative standard error lower than 10% per cooling unit. Finally, we discarded records associated with transitional directions according to the authors' prescriptions.

6. Interpretation & Discussion

6.1. Eruption Rate of HT2 Basalts

The Waja section was most likely emplaced during Chron C12n (Section 5.1) which spans less than 400 kyr according to the latest version of the GPTS (Ogg, 2020). This is entirely consistent with the four robust and indistinguishable $^{40}Ar/^{39}Ar$ ages from flows spanning the 1-km thick section. Under the assumption that the rate of change of geomagnetic secular variation (SV) did not significantly vary during the last 30 Myr, we used field models based on data from past few millennia to estimate $d\theta/dt$, and then calculate the emplacement rate dt/dh (h being stratigraphic thickness in meters) for the Waja section. To guarantee the similarity of the remanence acquisition process, we only relied on SV models derived from archaeomagnetic and volcanic data (Table 6.1); remanences from sediments usually produce smoother field variations than thermoremanences (e.g. Constable et al., 2016; Hellio & Gillet, 2018). A 300 yr step was used which a posteriori matches the average time interval between the successive magnetic readings from the Waja section. We finally obtained the following 3 approximations of $d\theta/dt$ = 0.06 °/yr (ARCH3k.1, Korte et al., 2009), 0.03 °/yr (COV_ARCH, Hellio & Gillet, 2018) and 0.04 °/yr (BIGMUDI4k.1, Arneitz et al., 2019).

Table 6-1: Secular Variation models based on Archaeomagnetic and Volcanic data (Arneitz et al., 2019; Hellio & Gillet, 2018; Korte et al., 2009) used to estimate the change in reversal angle ($d\theta/dt$), this was divided by the computed root-mean-square rate of change of θ with respect to elevation h to produce the emplacement rate (dt/dh) of the Waja section, multiplying the emplacement rate with the stratigraphic height of the section (1,040 m) gave us the duration of emplacement of the Waja section.

Study	SV Model	Developed from	$d\theta/dt$ (°/yr)	dt/dh (yr/m)	Duration (Yr)
Korte et al., 2009	ARCH3k.1	Archaeomagnetic	0.06	16.67	17,334
Hellio et al., 2018	COV_ARCH	Archaeomagnetic + Volcanic	0.04	25.00	26,000
Arneitz et al., 2019	BIGMUDk.1I	Archaeomagnetic + Volcanic	0.03	33.34	34,667

The range in dθ/dt of 0.03–0.06°/yr was assumed as representative of SV over the past 30 Myr and was subsequently divided by the root-mean-square rate of change of θ with respect to elevation h (~1°/m, Section 5.1) thus we obtained dt/dh = 17 – 33 yr/m for the Waja section. dt/dh was then multiplied by the stratigraphic height (1,040 m) the result of which suggests that the Waja section may have been emplaced within as little as 18–34 kyr. Noting that the reversal frequency during the Pleistocene (3.9 Myr^{-1}) was higher than during the Early Oligocene (1.7 Myr^{-1}; (Ogg, 2020) and that SV may increase with reversal frequency (e.g. Biggin et al., 2008; Doubrovine et al., 2019), we recognized that dθ/dt may have been overestimated and that the estimated emplacement duration of the Waja section (18–34 kyr) should be considered as a lower bound.

The original horizontal extent of the EYT was estimated to be $4 \cdot 10^5$ km^2 (Natali et al., 2016) and $8 \cdot 10^5$ km^2 (Rochette et al., 1998) considering circular areas with radii of 350 and 500 km. For an estimated thickness of ~1.5 km, the original volume of the EYT ranges between 0.6 and $1.2 \cdot 10^6$ km^3, in agreement with the estimate of $0.7 \cdot 10^6$ km^3 based on geological mapping (Rooney, 2017). Assuming the total emplacement took place over 1–2 Myr yields an average extrusion rate of 0.3–1.2 km^3/yr. For local extrusion rates, the LT basalts cover ~30% of the entire EYT (Beccaluva et al., 2009), leading to an estimated volume of $0.18–0.36 \cdot 10^6$ km^3. The Belessa section was deposited during all chrons C11n.2n and C11n.1r and partially C11r and C11.1n (Lhuillier & Gilder, 2019). A duration of 0.5–1.4 Myr for Belessa yields an extrusion rate of 0.1–0.7 km^3/yr.

The magnetostratigraphy of the Lima-Limo section is more ambiguous (Rochette et al., 1998). It starts in chron C11r but ends either in chron C10r (in which case chron C11n.1r is absent from the stratigraphy) or in C11n.1r. In the former case, which is more compatible with the magnetostratigraphy of the Belessa section, a duration of 0.8–2.3 Myr implies extrusion rates of 0.1–0.5 km^3/yr. In the latter case, preferred by Touchard et al. (2003) based on the correlation of tephra layers with marine sediments, a duration of 0.4–1.1 Myr implies extrusion rates of 0.2–0.9 km^3/yr. The area encompassed by HT2 comprises ~20% of the EYT (Beccaluva et al., 2009). The Waja section, which provides the first continuous magnetostratigraphy of the HT2

facies, was emplaced in less than 386 kyr according to the GTPS, less than 260 kyr according to $^{40}Ar/^{39}Ar$ age determinations, and within 18–34 kyr using the SV geochronometer, which implies an extrusion rate of 4–13 km^3/yr.

The spatial variability in the geochemistry of the EYT is thus associated with strong contrasts in the local extrusion rates estimated to 0.1–0.9 km^3/yr for LT basalts versus 4–13 km^3/yr for HT2 basalts. No age constraints exist for the HT1 basalts; however, if those dated by Ukstins et al. (2002) from the Dessie-Bati section at 29.34 ± 0.15 Ma were HT1, as inferred from the map (Figure 6.1), HT1 and LT overlap in time. In the framework of the plume theory (Campbell, 2007), the EYT have been linked with the Afar mantle plume, the existence of which is corroborated by local tomographic models of the mantle beneath East Africa (Adams et al., 2012; Hansen et al., 2012). Our study provides quantitative constraints on the extrusion duration of the plume head, thereby confirming geodynamic models that predict the first stage of flood volcanism is the most intense. For the Ethiopian-Yemen Traps, 20% of the HT2 basalts, representative of the plume head, were emplaced within ~0.02–0.2 Myr, whereas the remaining 80% was erupted over ca. 1.5 Myr.

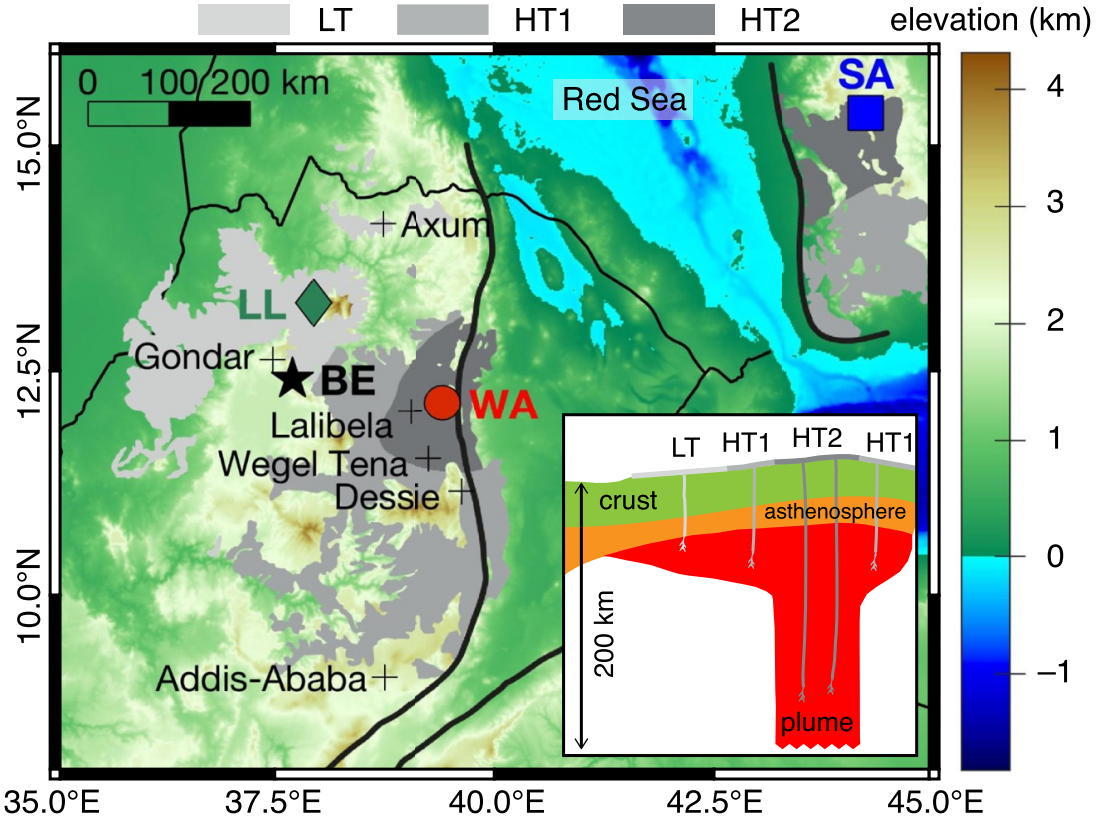

Figure 6.1: Schematic map and geodynamic interpretation of the Ethiopia-Yemen Traps (adapted from Eid et al., 2021; Natali et al., 2016). Section names are: Belessa (BE, Lhuillier et al., 2019a), Lima-Limo (LL, Rochette et al., 1998), Sana'a (SA, Kellogg & Reynolds, 1983) and Waja (WA, Eid et al., 2021). Gray patches indicate the spatial distribution of the basalt flows based on titanium concentrations following Pik et al. (1998): LT, TiO_2 1–3 wt%, HT1, TiO_2 2–4 wt% and HT2, TiO_2 3–7 wt%. Black thin lines indicate the land borders. Black thick lines delimit the Afar escarpment.

The Eocene/Oligocene boundary, associated with the Oi-1 global cooling event, followed by five subsequent global cooling events in the Oligocene based on variations in $\delta^{13}C$ and $\delta^{18}O$ (Figure 6.2, Speijer et al., 2020). The Oi-2 event within chron C11r has been linked to a major sea-level drop and the lowest diversity in land mammals (Pekar & Miller, 1996; Prothero, 1994). Rochette et al. (1998) and subsequently Touchard et al. (2003) proposed that silicic volcanism at the terminating stage of the EYT eruption may be responsible for the Oi-2 event. Ukstins et al. (2002) refuted this correlation by noting that the bimodal volcanism postdated the Oi-2 event. In contrast, results from the Waja section are indicative that the emplacement of the

HT2 flood basalts during chron C12n, constituting 20% of the total trap volume over a rapid interval of 18–34 kyr, may be the trigger for the Oi-2 glacial event. Indeed, the intensely pulsed extrusion rate of 4–13 km^3/yr largely exceeds the average values of 1.5–3.0 km^3/yr for the Siberian and Deccan Traps.

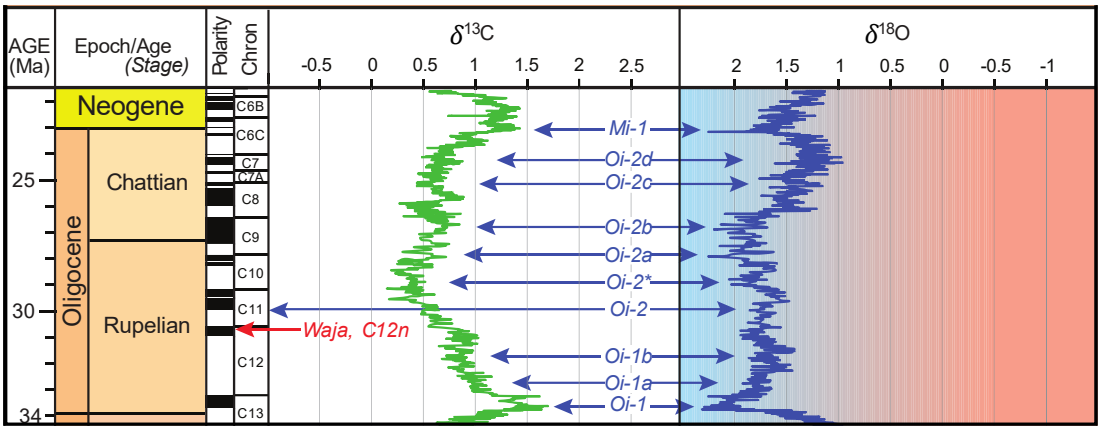

Figure 6.2: Figure adapted from Speijer et al., (2020) showing global cooling events during the Oligocene (Blue arrows) based on the generalized oxygen and carbon isotope curves for the Oligocene (Cramer et al., 2009) the Waja section (Red arrow) emplaced within 18-34 Kyr during chron C12n.

6.2. API From Ethiopia-Yemen Traps

Three studies (Table 2.4) already reported API determinations from the Early Oligocene Ethiopian Traps. For the Lima-Limo section (chrons C11r to C11n.1r or C10r; Ahn et al., 2021; Coulié et al., 2003; Rochette et al., 1998), Riisager et al. (1999) reported Thellier-Thellier results from six lava flows, yielding an average intensity of 23.7 ± 9.3 (1σ) μT (VDM = 57 ± 24 [1σ] ZAm^2, N = 17). For the same section, Yoshimura et al. (2020) recently reported Tsunakawa-Shaw results from eleven lava flows, yielding an average intensity of 16.2 ± 8.0 (1σ) μT (VADM = 42 ± 21 [1σ] ZAm^2, N = 30). For the Belessa section (chrons C11r to C11n.1n, Lhuillier & Gilder, 2019), Lhuillier et al. (2019a) reported Thellier-Coe results from five lava flows, yielding a mean intensity of 12.0 ± 3.0 (1σ) μT (VDM = 30 ± 8 [1σ] ZAm2, N = 48). For the Waja section (chron C12n, Eid et al., 2021), the only trustworthy API determinations were from flows W105 and W108, yielding a mean intensity of 24.2 ± 1.4 (1σ) μT (VDM = 57 ± 9 [1σ] ZAm^2, N = 18, Table 5.3).

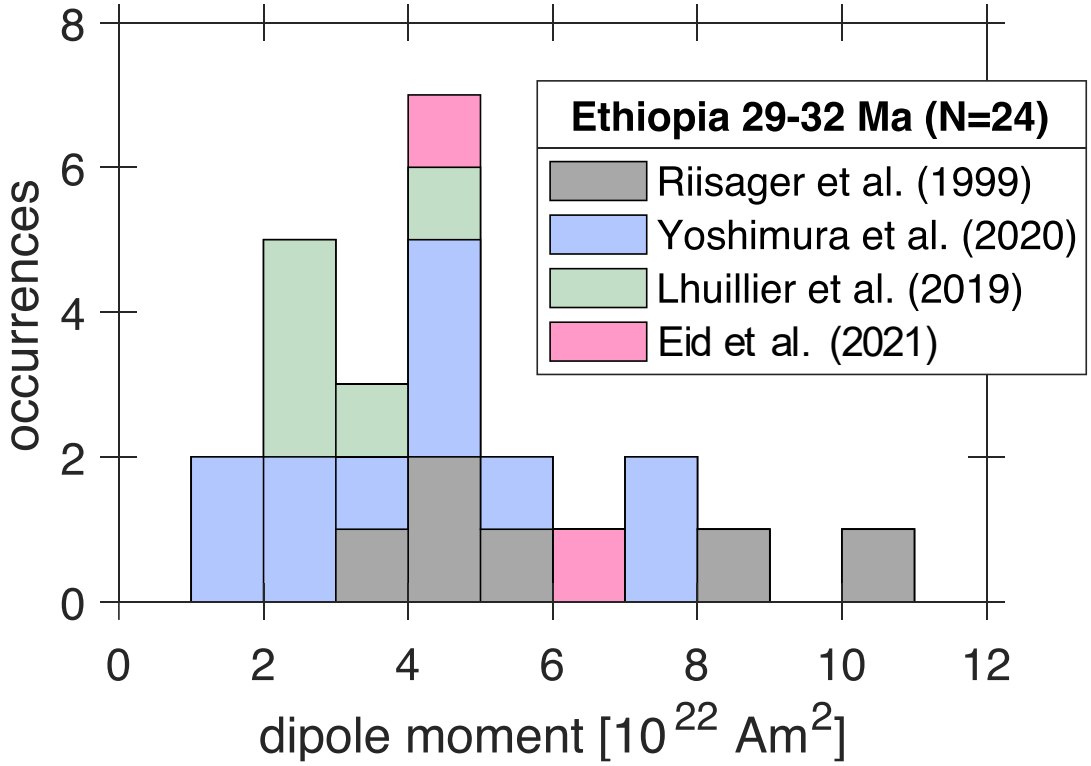

Figure 6.3: Histogram of dipole moments from the Ethiopia Yemen Traps (29–32 Ma) (adapted from Eid et al., 2021) without applying selection criteria except a minimum of two determinations per cooling unit.

We combined the flow-mean determinations with a minimum of two individual determinations (i.e., only applying lenient selection criteria to retain a sufficient number of determinations), As illustrated in Figure 5.3, we obtain a right-tailed, seemingly bimodal, distribution of intensities (median of 17.8 μT, skewness of 0.7), leading to a median reconstructed dipole strength of 45.5 ± 22.0 (1σ) ZAm^2 (N = 24). Although we cannot exclude contamination by experimental errors, which could be due to variation in heating and cooling times, lack of precision of applied field, sample orientation and equipment calibration errors, the apparent bimodality of the distribution is most likely the signature of secular variation. The EYT were indeed emplaced in multiple pulses, the Lima-Limo and Belessa sections being known to be slightly posterior to the Waja section (Eid et al., 2021).

6.3. API Variability Over The Past 155 Myr

At a global scale, we analysed the reconstructed dipole strength over the past 155 Myr using the updated version of the WPD that was filtered with the selection criteria (Section 5.2) More specifically, we tested whether the division of the past 155 Myr into four "stationary" segments—intervals over which the distribution of chrons follows a Poisson distribution and an average reversal frequency can be defined—based on reversal frequency (Gallet & Hulot, 1997; Lowrie & Kent, 2004) also has a signature in the global API record. Following Lowrie & Kent (2004), the first segment was defined from polarity chron C12n to present, the second from subchron C32r.2r to chron C12r, and the fourth from chron M27n to chron M0r. The third segment solely consists of chron C34n (CNS) whereas the two chrons C33n and C33r adjacent to the CNS were omitted (Lowrie & Kent, 2004). Using the latest version of the GPTS (Ogg, 2020), we estimated the four intervals as 0–31 Ma, 31–74 Ma, 84–121 Ma and 121–155 Ma, yielding average f_{rev} values of 4.2 Myr^{-1}, 1.3 Myr^{-1}, 0 Myr^{-1} and 2.8 Myr^{-1}, respectively.

Before proceeding to the analysis, we would like to stress three salient peculiarities of the investigated dataset:

1) The distribution of reconstructed dipole moments for the 0–31 Ma segment (N = 348) is dominated by data from the Brunhes chron (N = 244). Within this segment, the 0–0.77 and 0.77–31 Ma, API distributions are statistically distinct (Kolmogorov-Smirnov test, p-value of $1 \cdot 10^{-11}$), suggesting abnormal geomagnetic field behaviour during the Brunhes chron (e.g. Khokhlov & Shcherbakov, 2015) and/or insufficient sampling during the 0.77–31 Ma interval.
2) The distribution for the 84–121 Ma segment (N = 67) appears to be bimodal (e.g. Bobrovnikova et al., 2022; Shcherbakova et al., 2012), which may reflect distinct geomagnetic field behaviour during the CNS with a bistable geodynamo (e.g. Lhuillier et al., 2016) and/or insufficient sampling during this interval.
3) The unfiltered distribution of dipole moments for the Ethiopian traps (Section 6.2, Figure 6.3) is statistically indistinguishable from the 0.77–31 Ma and 31–74 Ma distributions (Kolmogorov-Smirnov test, p-values of 0.19 and 0.20 respectively; Figure 6.4 b). It indicates that, even if the unfiltered distribution of the Ethiopian dataset does not fulfil our strict selection criteria—in the sense that (i) Riisager et

al. (1999) reported only 2–3 successful Thellier determinations per cooling unit; and (ii) Yoshimura et al. (2020) reported only 2–4 successful Tsunakawa-Shaw determinations per cooling unit—it seems to adequately capture the geomagnetic behaviour during the Palaeogene.

Table 6-2: Analysis of the Thellier-style absolute palaeointensity determinations (adapted from Eid et al., 2022) from the WPD and PINT8 databases over the intervals 0–0.77 Ma (Brunhes chron), 0.77– 31 Ma, 31–74 Ma, 84–121 Ma (Cretaceous Normal Superchron) and 121–155 Ma. The number of absolute palaeointensity determinations (N) The average dipole moment (μ), the standard deviation (σ) and the relative standard deviation ($\varepsilon_F = \sigma/\mu$) are provided with 95 per cent uncertainties deduced from 10,000 bootstrap experiments. Results marked with a cross (†) were obtained with the selection criteria from Section 5.2 (at least five determinations with pTRM check per cooling unit, and within-unit relative standard error lower than 10 per cent). Results marked with an asterisk (∗) were obtained for a QPI score greater than five (Biggin & Paterson, 2014; Hawkins et al., 2021; Kulakov et al., 2019).

Interval (Ma)	**Database**	**N**	μ **(10^{22} Am^2)**	σ **(10^{22} Am^2)**	ε_F **(%)**
0 – 0.77	WPD †	244	8.21 ± 0.40	3.18 ± 0.26	39 ± 4
	PINT8 †	124	6.22 ± 0.42	2.40 ± 0.26	39 ± 4
	PINT8 *	52	6.35 ± 0.77	2.77 ± 0.59	44 ± 9
0.77–31	WPD †	104	5.62 ± 0.44	2.22 ± 0.30	40 ± 6
	PINT8 †	87	6.03 ± 0.50	2.34 ± 0.36	39 ± 6
	PINT8 *	136	5.37 ± 0.47	2.71 ± 0.55	50 ± 9
31–74	WPD †	25	5.77 ± 1.12	2.71 ± 1.30	47 ± 18
	PINT8 †	24	5.05 ± 1.44	3.44 ± 1.24	68 ± 18
	PINT8 *	21	4.86 ± 1.50	3.34 ± 1.50	69 ± 22
84–121	WPD †	67	7.13 ± 0.98	4.05 ± 0.48	57 ± 6
	PINT8 †	77	7.19 ± 0.86	3.77 ± 0.48	52 ± 6
	PINT8 *	61	7.97 ± 1.03	4.03 ± 0.47	51 ± 7
121–155	WPD †	36	4.69 ± 1.14	3.35 ± 1.34	71 ± 20
	PINT8 †	27	5.10 ± 1.36	3.39 ± 1.54	66 ± 22
	PINT8 *	7	3.75 ± 2.35	2.94 ± 2.18	79 ± 43

With this, we subsequently compare the average dipole moment μ for the previously defined intervals: 0–0.77 Ma, 31–74 Ma, 84–121 Ma, and 121–155 Ma (Figure 6.4 a–b). The 95% confidence limits of μ were estimated from the distribution of 10,000 bootstrapped samples (Table 6.2). When compared over the whole 0–155 Ma interval, average dipole moment during the Brunhes chron (82 ± 4 ZAm^2, N = 244) is ∼15% stronger than during the CNS (71 ± 10 ZAm^2, N = 67), with the two distributions being statistically distinct (Kolmogorov-Smirnov test, p-value of $2 \cdot 10^{-5}$). However, if we omit the Brunhes chron from the analysis due to its potential abnormal behaviour (e.g. Khokhlov & Shcherbakov, 2015), the current version of the WPD is consistent with higher dipole strength during the CNS than during the three other segments. Average dipole moment during the CNS is 34% stronger than during the 121–155 Ma segment (47 ± 11 ZAm^2, N = 36) and 21% stronger than during the 0.77–31 Ma segment (56 ± 4 ZAm^2, N = 104), with statistically distinct distributions (Kolmogorov-Smirnov test, p-values of $2 \cdot 10^{-2}$ and $3 \cdot 10^{-2}$ respectively). Average dipole moment during the CNS is also 19% stronger than during the 31–74 Ma segment (58 ± 11 ZAm^2, N = 25), although the two distributions are in this case statistically indistinguishable (Kolmogorov-Smirnov test, p-values of 0.11).

We can now investigate the relationship between average dipole moment and average reversal frequency for the four previously defined "stationary" segments: 0.77–31 Ma, 31–74 Ma, 84–121 Ma, and 121–155 Ma (Figure 6.4c). Given the intersection of the 95% confidence limits of the segments 0.77–74 Ma, 31–74 Ma and 121–155 Ma—confirmed by inconclusive Kolmogorov-Smirnov tests; p-value of 0.13 when comparing the 31–74 Ma and 121–155 Ma segments; p-value of 0.99 when comparing the 0.77–31 Ma and 31–74 Ma segments—no gradual decrease of average dipole strength with increasing reversal frequency can be unambiguously identified, contrary to predictions from numerical dynamo simulations (e.g. (Driscoll & Olson, 2009; Lhuillier et al., 2019b). Average dipole moment during the CNS is certainly 20–35% higher than during the three other segments with reversals, but this observation relies on two strong assumptions.

1) The determinations from the Brunhes chron were excluded from the analysis, assuming that this chron represents an anomalous behaviour of the Earth's magnetic field, such as the onset of a superchron (e.g. Shcherbakov & Fabian, 2012).

2) The bimodality of the distribution of dipole moments during the CNS was taken for granted, whereas it was shown to be partly ascribed to the nature of the used material (e.g. Bobrovnikova et al., 2022). Determinations on single crystals (123 ± 6 ZAm^2, N = 15) indeed yield significantly higher dipole moments than determinations on whole rocks (56 ± 10 ZAm^2, N = 52), in which case the distribution of dipole moments from whole-rock determinations during the CNS becomes statistically indistinguishable from the three distribution of dipole moments for the three other segments.

Note that the analysis of the PINT8 database (Bono et al., 2022), using the same selection criteria as for the WPD, leads to unchanged conclusions (Table 6.2). Within the 95% confidence limits, the values of μ calculated from the WPD or PINT databases are statistically indistinguishable for the four "stationary" segments: only significantly different for the Brunhes chron. This can be explained by the following discrepancies between the two databases:

1) PINT8 only reports API determinations older than 50 kyr (whereas WPD also reports younger API determinations obtained from geological material).
2) PINT8 only reports data published until the end of 2019 (whereas WPD also reports data published in 2020 and 2021)
3) PINT8 tends to report multi-method averages (whereas WPD usually follows the authors' choice, i.e., with different entries for each palaeointensity method if the authors did not average the results in the publication).

An alternative filtering approach based on QPI for the Thellier-style determinations of PINT8 leads once more to unchanged conclusions (QPI ≥ 5, Table 6.2). Basing our analysis on the current versions of the WPD and PINT databases, we thus cautiously conclude that a decrease of average dipole moment with increasing reversal frequency cannot be unambiguously identified for the 0–155 Ma interval.

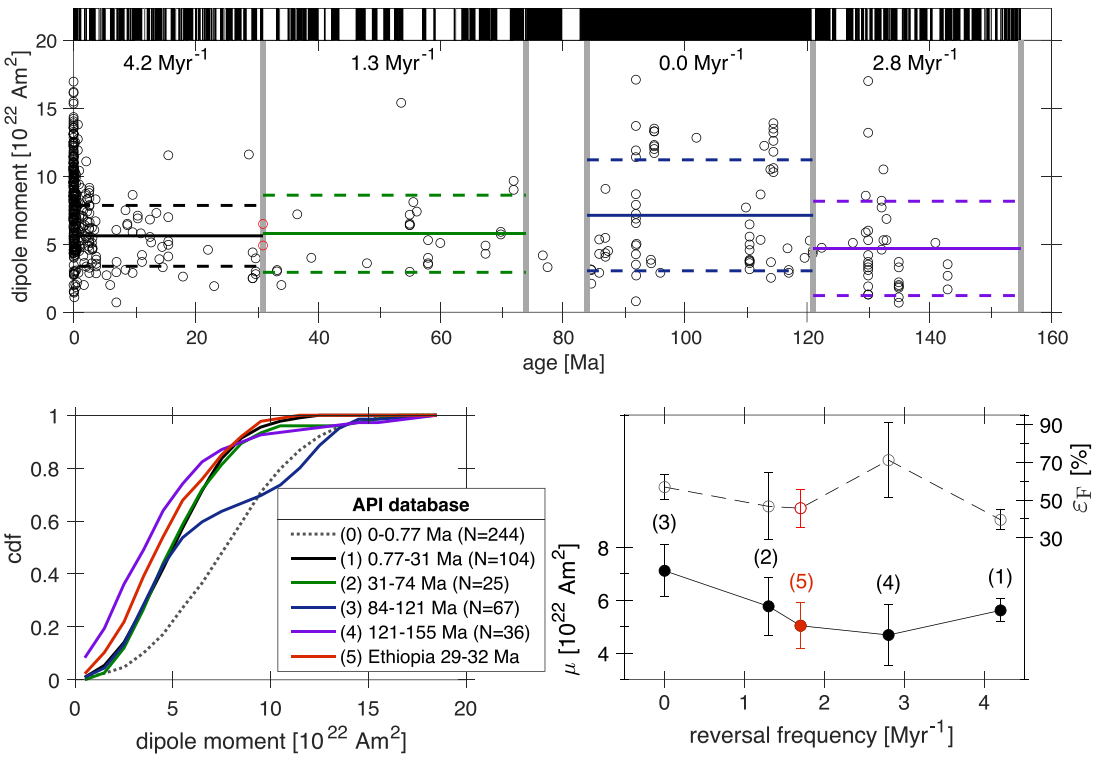

Figure 6.4: Analysis of absolute palaeointensity results over the past 155 Myr (adapted from Eid et al., 2022). (a) Temporal evolution of reconstructed dipole moments (VDM or VADM) using the strict selection criteria from Section 5.2. The red discs correspond to the VDMs from flows W105 and W108 (Waja section). Geomagnetic polarity timescale on the top based on the most recent update of the C- and M- sequences (Ogg, 2020). (b) Cumulative distribution function of the reconstructed dipole moments for the four "stationary" segments defined by Lowrie & Kent (Lowrie & Kent, 2004). (c) Average and relative standard deviation of reconstructed dipole moments as a function of reversal frequency for the previously considered time intervals as well as the Ethiopian dataset in red.

6.4. Relative Field Strength Variability as PSV Proxy

The relative variability ε_F in intensity (standard deviation normalised by the mean for a sequence of palaeointensity determinations) constitutes an alternative to the VGP scatter S to quantify PSV, with its own strengths and weaknesses. Whereas the palaeolatitude dependent S parameter requires the combination of local palaeodirectional datasets from several palaeolatitudes to construct a latitudinal profile (e.g. Cromwell et al., 2018; de Oliveira et al., 2018; Doubrovine et al., 2019), ε_F provides a self-consistent PSV proxy (i.e., representative of the geodynamo activity) at a section's level but with the difficulty that it requires the estimation of a sufficient number of RPI determinations. It has been predicted from numerical dynamo simulations that ε_F linearly increases with reversal frequency f_{rev} (Lhuillier & Gilder, 2013), which itself increases with the vigour of the geodynamo (e.g. Driscoll & Olson, 2009; Lhuillier et al., 2013, 2019b).

For the present selection of the WPD, we obtain the bootstrap estimates $\varepsilon_F = 0.40 \pm 0.02$ (N = 306) for the 0–3 Ma interval, $\varepsilon_F = 0.39 \pm 0.03$ (N = 105) for the 0.77–31 Ma interval (Figure 6.4c). Interestingly, these two API-based estimates fit inside the confidence interval of the RPI-based estimate for the Plio-Pleistocene of 0.44 ± 0.05 (1σ, N = 47) (Lhuillier et al., 2017b). In contrast, the other API based estimates tend to increase with age {$\varepsilon_F = 0.48 \pm 0.09$ (N = 26) for 31–74 Ma, $\varepsilon_F = 0.66 \pm 0.04$ (N = 80) for 84–121 Ma, $\varepsilon_F = 0.64 \pm 0.09$ (N = 31) for 120–155 Ma} independent of the changes in reversal frequency (Figure 6.4c). The agreement in one case (0.77–31 Ma) added to the disagreement in all other cases (31–74, 84–121 and 121–155 Ma) with the modelled dependency between ε_F and f_{rev} might naturally be fortuitous. Nevertheless, this dichotomy likely shows that the statistical distribution of the API determinations is well converged for the 0.77–31 Ma segment whereas the insufficient number and/or lacunary quality of the API determinations does not allow a robust characterisation of the distribution prior to 31 Ma yet.

However, relying on the WPD to estimate ε_F at various time intervals is questionable. The obvious advantage of such a global approach would be to average

out spatial variability but the main drawback would be the introduction of additional errors due to:

1) The inevitable diversity in the measurement protocols and acceptance criteria chosen by the experimenters. This could be potentially minimised by employing stricter and/or additional selection criteria when the API database is analysed (e.g. Biggin & Paterson, 2014; Kulakov et al., 2019) with the risk of introducing subjectivity and drastically decreasing the number of records.
2) The propagation of experimental errors when converting the intensities into virtual dipole moments. This critically depends on the uncertainties on the measured palaeoinclination or expected palaeolatitude.
3) The implicit assumption that the geomagnetic field is dipolar during the investigated time interval. This is probably the most difficult to constrain (e.g. Courtillot & Besse, 2004).

A local approach would be a much more reliable technique even though it could inopportunely emphasise a local geomagnetic anomaly. In addition to the new estimate $\varepsilon_F = 0.39 \pm 0.07$ (1σ, N = 19) provided from Waja (Eid et al., 2022) for the Ethiopian traps (29–32 Ma, $f_{rev} = 2.8$ Myr^{-1}), three other estimates have been published from sequences of lava flows: $\varepsilon_F = 0.44 \pm 0.05$ (1σ, N = 47) for the Boring Volcanic Field (0–3 Ma, $f_{rev} = 3.9$ Myr^{-1}; Lhuillier et al., 2017), $\varepsilon_F = 0.31 \pm 0.05$ (1σ, N = 15) for the Tuoyun Palaeocene volcanics (60–70 Ma, $f_{rev} = 1.3$ Myr^{-1}; Meng et al. 2020), and $\varepsilon_F = 0.31 \pm 0.04$ (1σ, N = 28) for the Tuoyun Cretaceous volcanics (112–115 Ma, $f_{rev} = 0$ Myr^{-1}; Lhuillier et al., 2016). To assess the relationship between ε_F and f_{rev}, we plotted previously published ε_F values as well as our new estimate as a function of f_{rev} (Figure 6.5). As predicted from numerical dynamo simulations, we find that ε_F tends to increase with f_{rev}, yielding a linear relationship $\varepsilon_F = 0.29 + 0.036 \times f_{rev}$. We note that the experimental slope is steeper than the prediction by Lhuillier & Gilder (2013).

This can naturally be ascribed to the limited number of ε_F estimates on volcanic rocks as well as to their individual uncertainties. In this respect, we recall that the reliability of RPI determinations critically depends on the assumed homogeneity of the rock-magnetic properties of the remanence carriers throughout the section. Alternatively, the discrepancy may also reflect intrinsic inaccuracies of dynamo modelling (such as overestimated viscosity or simplified boundary conditions). At any

rate, the four available observations convincingly corroborate a positive correlation between changes in PSV (here quantified by ε_F) and f_{rev} over the past 120 Myr.

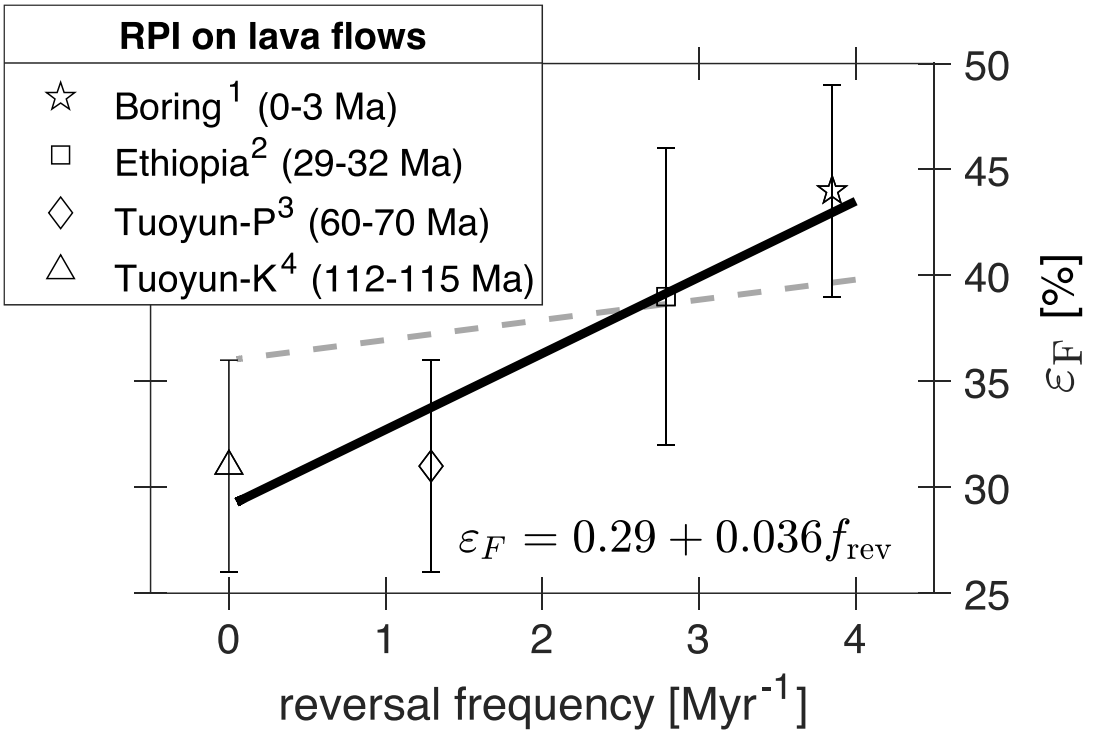

Figure 6.5 Analysis RPI results over the past 115 Myr (adapted from Eid et al., 2022). Relative variability ε_F in intensity (PSV proxy. (Lhuillier & Gilder, 2013) as a function of reversal frequency for the four available RPI datasets on lava flows: (1) Boring Volcanic Field (0–3 Ma. Lhuillier et al., 2017). (2) Waja section (~31 Ma. Eid et al., 2022). (3) Tuoyun palaeocene volcanics (60–70 Ma. Meng et al., 2020). (4) Tuoyun Early Cretaceous volcanics (112– 115 Ma. Lhuillier et al., 2016). The grey dashed line corresponds to the prediction from numerical dynamo simulations (Lhuillier & Gilder, 2013).

7. Conclusions

A 1 km-thick section of flood basalts was sampled on the Kobo Lalibela mountain road near the town of Waja along with 500 m thick section from the Tarmaber-Gussa formation north of Lalibela, producing 1,029 samples from 123 cooling units. Geochemical investigation on samples collected from the Waja section were compared with major element results from the Waja section flood basalts consistently exhibited HT2 characteristics with high titanium content (3.11–4.60 wt% TiO_2) and except for two consecutive flows plotted in or near the picritic field in the TAS diagram. Furthermore, the Waja section's REE patterns showed great affinity to HT2 REE patterns from previous studies. Partial melt modelling indicated that the HT2 basalts originated from a deeper mantle source than the LT basalts.

Four robust and indistinguishable $^{40}Ar/^{39}Ar$ ages from flows spanning the 1-km thick Waja section were obtained with a weighted-mean $^{40}Ar/^{39}Ar$ age of 31.18 ± 0.28 Ma (95% confidence; Ludwig, 2008), timing the HT2 basalt eruption during the early stages of flood basalt activity. A single $^{40}Ar/^{39}Ar$ age of 17.02 ± 0.43 Ma (1σ) for the Tarmaber formation was determined, in addition to this the geochemical results for the Tarmaber-Gussa section were scattered on the TAS diagram, these two results support the hypothesis that the Tarmaber-Gussa basalts were emplaced due to shield volcanism which occurred ~12 Myr later than trap volcanism.

Palaeomagnetic direction data and analysis of the Waja section produced 68 solely normal polarities and six excursional directions not antipodal to the obtained normal polarities. The normal polarities in combination with the obtained $^{40}Ar/^{39}Ar$ age position the section's emplacement during chron C12n (<400 kyr). Furthermore, the precision parameter $k = 6.4$ and elongation $e = 1.9$ ($N = 68$) differs significantly from the reference distribution $k = 17.0$ and $e = 2.7$ ($N = 167$) from previous PSV studies indicating an emplacement <1 Myr for the entire 1 km-thick section. Further investigation using a secular variation geochronometer gives 18–34 kyr for the duration of emplacement of the Waja section.

The short duration of emplacement of 18–34 kyr implies an extrusion rate of 4–13 km^3/yr which is an order of magnitude higher than the average extrusion rate of the entirety of the EYT (0.3–1.2 km^3/yr). This unusually high extrusion rate during the

C12n chron could potentially be interpreted as the trigger for the Oi-2 glaciation event that was recorded during the C11r chron. Clearly these results warrant further investigation in the field of volcanology, in combination with palaeoenvironmental geology to fully understand the effects of such high emplacement rates on the palaeoclimate.

The API experiments and analysis produced two new VDMs for the early Oligocene from the EYT: 49.1 ± 4.5 ZAm^2 and 64.9 ± 6.9 ZAm^2. These results were added to the updated WPD, analysing the API records failed to show any robust trends such as a decrease of field strength with increasing reversal frequency. This may be the signature of a more complex modus operandi of the geodynamo than the one predicted by numerical dynamo simulations, but more likely reflects the insufficient resolution of the present API record and should be seen as an encouragement to acquire further data that fulfil the modern standards of palaeomagnetism.

The RPI experiments and analysis yielded an estimate $\varepsilon_F = 0.39 \pm 0.07$ (1σ, N = 19). This RPI was combined with the three other available estimates of ε_F from the Boring field in USA for 0-3 Ma, Toyun-P in China for 60-70 Ma and Toyun-K for 112-115 Ma, since the onset of the CNS, this showed that the variations in palaeosecular variation and reversal frequency are likely to positively correlate, in agreement with the predictions from numerical dynamo simulations.

8. Bibliography

Adams, A., Nyblade, A., & Weeraratne, D. (2012). Upper mantle shear wave velocity structure beneath the East African plateau: Evidence for a deep, plateauwide low velocity anomaly. *Geophysical Journal International*, *189*(1), 123–142. https://doi.org/10.1111/j.1365-246X.2012.05373.x

Ahn, H. S., Kidane, T., Otofuji, Y. I., Yamamoto, Y., Ishikawa, N., & Yoshimura, Y. (2021). High-resolution palaeomagnetic results of Ethiopian trap series from Lima Limo section: Implications for the Oligocene geomagnetic field behaviour and timing of volcanism. *Geophysical Journal International*, *225*(1), 311–328. https://doi.org/10.1093/gji/ggaa557

Arneitz, P., Egli, R., Leonhardt, R., & Fabian, K. (2019). A Bayesian iterative geomagnetic model with universal data input: Self-consistent spherical harmonic evolution for the geomagnetic field over the last 4000 years. *Physics of the Earth and Planetary Interiors*, *290*, 57–75. https://doi.org/10.1016/j.pepi.2019.03.008

Baker, J., Snee, L., & Menzies, M. (1996). A brief Oligocene period of flood volcanism in Yemen: implications for the duration and rate of continental flood volcanism at the Afro-Arabian triple junction. *Earth and Planetary Science Letters* (Vol. 38). https://pubs.er.usgs.gov/publication/70019397

Beccaluva, L., Bianchini, G., Natali, C., & Siena, F. (2009). Continental flood basalts and mantle plumes: A case study of the Northern Ethiopian Plateau. *Journal of Petrology*, *50*(7), 1377–1403. https://doi.org/10.1093/petrology/egp024

Biggin, A. J., & Paterson, G. A. (2014). A new set of qualitative reliability criteria to aid inferences on palaeomagnetic dipole moment variations through geological time. *Frontiers in Earth Science*, *2*. https://doi.org/10.3389/feart.2014.00024

Biggin, A. J., Perrin, M., & Dekkers, M. J. (2007). A reliable absolute palaeointensity determination obtained from a non-ideal recorder. *Earth and Planetary Science Letters*, *257*(3–4), 545–563. https://doi.org/10.1016/j.epsl.2007.03.017

Biggin, A. J., van Hinsbergen, D. J. J., Langereis, C. G., Straathof, G. B., & Deenen, M. H. L. (2008). Geomagnetic secular variation in the Cretaceous Normal

Superchron and in the Jurassic. *Physics of the Earth and Planetary Interiors*, *169*(1–4), 3–19. https://doi.org/10.1016/j.pepi.2008.07.004

Bobrovnikova, E. M., Lhuillier, F., Shcherbakov, V. P., Shcherbakova, V. v., Zhidkov, G. v., Lebedev, I. E., Eid, B., & Pavlov, V. E. (2022). High-Latitude Paleointensities During the Cretaceous Normal Superchron From the Okhotsk–Chukotka Volcanic Belt. *Journal of Geophysical Research: Solid Earth*, *127*(2). https://doi.org/10.1029/2021JB023551

Bogue, S. W. (2018). Correlated Relative and Absolute Geomagnetic Paleointensities From a Pliocene N-R Polarity Reversal Record in Basaltic Lava Flows on Kauai, Hawaii. *Geochemistry, Geophysics, Geosystems*, *19*(12), 4773–4787. https://doi.org/10.1029/2018GC007748

Bono, R. K., Paterson, G. A., van der Boon, A., Engbers, Y. A., Michael Grappone, J., Handford, B., Hawkins, L. M. A., Lloyd, S. J., Sprain, C. J., Thallner, D., & Biggin, A. J. (2022). The PINT database: A definitive compilation of absolute palaeomagnetic intensity determinations since 4 billion years ago. *Geophysical Journal International*, *229*(1), 522–545. https://doi.org/10.1093/gji/ggab490

Butler, R. F. (2004). *Paleomagnetism: magnetic domains to geologic terranes. Choice Reviews Online, 29(10), 29–5708-29–5708. https://doi.org/10.5860/CHOICE.29-5708*

Calvo, M., Prévot, M., Perrin, M., & Riisager, J. (2002). Investigating the reasons for the failure of palaeointensity experiments: A study on historical lava flows from Mt. Etna (Italy). *Geophysical Journal International*, *149*(1), 44–63. https://doi.org/10.1046/j.1365-246X.2002.01619.x

Campbell, I. H. (2007). Testing the plume theory. *Chemical Geology*, *241*(3–4), 153–176. https://doi.org/10.1016/j.chemgeo.2007.01.024

Cande, S. C., & Kent, D. v. (1995). Revised calibration of the geomagnetic polarity timescale for the Late Cretaceous and Cenozoic. *Journal of Geophysical Research: Solid Earth*, *100*(B4), 6093–6095. https://doi.org/10.1029/94JB03098

Channell, J., Erba, E., Nakanishi, M. & Tamaki, K., (1995). Late Jurassic-Early Cretaceous Time Scales And Oceanic Magnetic Anomaly Block Models. *SEPM*, *54*, 51–63. https://oceanrep.geomar.de/id/eprint/45831

Chenet, A. L., Fluteau, F., Courtillot, V., Gérard, M., & Subbarao, K. v. (2008). Determination of rapid Deccan eruptions across the Cretaceous-Tertiary boundary using paleomagnetic secular variation: Results from a 1200-m-thick section in the Mahabaleshwar escarpment. *Journal of Geophysical Research: Solid Earth*, *113*(4). https://doi.org/10.1029/2006JB004635

Coe, R. S. (1967). The Determination of Paleo-Intensities of the Earth's Magnetic Field with Emphasis on Mechanisms which Could Cause Non-ideal Behavior in Thellier's Method. *Journal of Geomagnetism and Geoelectricity* (Vol. 19, Issue 3). https://doi.org/10.5636/jgg.19.157

Coe, R. S., Grommé, S., & Mankinen, E. A. (1978). Geomagnetic paleointensities from radiocarbon-dated lava flows on Hawaii and the question of the Pacific nondipole low. *Journal of Geophysical Research: Solid Earth*, *83*(B4), 1740–1756. https://doi.org/10.1029/jb083ib04p01740

Constable, C., Korte, M., & Panovska, S. (2016). Persistent high paleosecular variation activity in southern hemisphere for at least 10 000 years. *Earth and Planetary Science Letters*, *453*, 78–86. https://doi.org/10.1016/j.epsl.2016.08.015

Coulié, E., Quidelleur, X., Courtillot, V., Lefèvre, J. C., & Chiesa, S. (2003). Comparative K-Ar and Ar/Ar dating of Ethiopian and Yemenite Oligocene volcanism: Implications for timing and duration of the Ethiopian traps. *Earth and Planetary Science Letters*, *206*(3–4), 477–492. https://doi.org/10.1016/S0012-821X(02)01089-0

Courtillot, V. and Besse, J. (2004). A Long-Term Octupolar Component in the Geomagnetic Field? (0–200 Million Years B.P.). *In Timescales Of The Paleomagnetic Field* (eds J.E.T. Channell, D.V. Kent, W. Lowrie and J.G. Meert). https://doi.org/10.1029/145GM05

Courtillot, V. E., & Renne, P. R. (2003). On the ages of flood basalt events. *Comptes Rendus - Geoscience*, *335*(1), 113–140. https://doi.org/10.1016/S1631-0713(03)00006-3

Cox, A. (1970). Latitude Dependence of the Angular Dispersion of the Geomagnetic Field. *Geophysical Journal International*, *20*(3), 253–269. https://doi.org/10.1111/j.1365-246X.1970.tb06069.x

Cramer, B. S., Toggweiler, J. R., Wright, J. D., Katz, M. E., & Miller, K. G. (2009). Ocean overturning since the Late Cretaceous: Inferences from a new benthic foraminiferal isotope compilation. *Paleoceanography*, *24*(4). https://doi.org/10.1029/2008PA001683

Cromwell, G., Johnson, C. L., Tauxe, L., Constable, C. G., & Jarboe, N. A. (2018). PSV10: A Global Data Set for 0–10 Ma Time-Averaged Field and Paleosecular Variation Studies. *Geochemistry, Geophysics, Geosystems*, *19*(5), 1533–1558. https://doi.org/10.1002/2017GC007318

Cronin, M., Tauxe, L., Constable, C., Selkin, P., & Pick, T. (2001). Noise in the quiet zone. *Earth and Planetary Science Letters*, *190*(1–2), 13–30. https://doi.org/10.1016/S0012-821X(01)00354-5

Day, R., Fuller, M., & Schmidt, V. A. (1977). Hysteresis properties of titanomagnetites: Grain-size and compositional dependence. *Physics of the Earth and Planetary Interiors*, *13*(4), 260–267. https://doi.org/10.1016/0031-9201(77)90108-X

de Groot, L. v., Béguin, A., Kosters, M. E., van Rijsingen, E. M., Struijk, E. L. M., Biggin, A. J., Hurst, E. A., Langereis, C. G., & Dekkers, M. J. (2015). High paleointensities for the Canary Islands constrain the Levant geomagnetic high. *Earth and Planetary Science Letters*, *419*, 154–167. https://doi.org/10.1016/j.epsl.2015.03.020

de Groot, L. v., Biggin, A. J., Dekkers, M. J., Langereis, C. G., & Herrero-Bervera, E. (2013). Rapid regional perturbations to the recent global geomagnetic decay revealed by a new hawaiian record. *Nature Communications*, *4*. https://doi.org/10.1038/ncomms3727

de Oliveira, W. P., Franco, D. R., Brandt, D., Ernesto, M., da Ponte Neto, C. F., Zhao, X., de Freitas, F. B. V., & Martins, R. S. (2018). Behavior of the Paleosecular Variation During the Permian-Carboniferous Reversed Superchron and Comparisons to the Low Reversal Frequency Intervals Since Precambrian Times.

Geochemistry, Geophysics, Geosystems, *19*(4), 1035–1048. https://doi.org/10.1002/2017GC007262

Doubrovine, P. v., Veikkolainen, T., Pesonen, L. J., Piispa, E., Ots, S., Smirnov, A. v., Kulakov, E. v., & Biggin, A. J. (2019). Latitude Dependence of Geomagnetic Paleosecular Variation and its Relation to the Frequency of Magnetic Reversals: Observations From the Cretaceous and Jurassic. *Geochemistry, Geophysics, Geosystems*, *20*(3), 1240–1279. https://doi.org/10.1029/2018GC007863

Driscoll, P., & Olson, P. (2009). Effects of buoyancy and rotation on the polarity reversal frequency of gravitationally driven numerical dynamos. *Geophysical Journal International*, *178*(3), 1337–1350. https://doi.org/10.1111/j.1365-246X.2009.04234.x

Dunlop, D. J. (2002). Theory and application of the Day plot (Mrs/Ms versus Hcr/Hc) 1. Theoretical curves and tests using titanomagnetite data. *Journal of Geophysical Research*, *107*(B3), 2057. https://doi.org/10.1029/2001JB000487

Dunlop, D. J. (2011). Physical basis of the Thellier–Thellier and related paleointensity methods. *Physics of the Earth and Planetary Interiors*, *187*(3–4), 118–138. https://doi.org/10.1016/j.pepi.2011.03.006

Eid, B., Lhuillier, F., Gilder, S. A., Pfänder, J. A., Gebru, E. F., & Aßbichler, D. (2021). Exceptionally High Emplacement Rate of the Afar Mantle Plume Head. *Geophysical Research Letters*, *48*(23). https://doi.org/10.1029/2021GL094755

Eid, B., Lhuillier, F., Shcherbakov, V. P., & Shcherbakova, V. v. (2022). Do changes in geomagnetic secular variation, dipole moment and polarity reversal frequency correlate over the past 155 Myr? *Geophysical Journal International*, *230*(2), 1132–1146.

Fisher, R., 1953. Dispersion on a sphere, Proc. R. Soc. Lond., A, 217(1130), 295–305. https://doi.org/10.1098/rspa.1953.0064

Gallet, Y., & Hulot, G. (1997). Stationary and nonstationary behaviour within the geomagnetic polarity time scale. *Geophysical Research Letters*, *24*(15), 1875–1878. https://doi.org/10.1029/97GL01819

Granot, R., Tauxe, L., Gee, J., & Ron, H. (2007). A view into the Cretaceous geomagnetic field from analysis of gabbros and submarine glasses. *Earth and*

Planetary Science Letters, *256*(1–2), 1–11. https://doi.org/10.1016/j.epsl.2006.12.028

Haggerty, S. E. (1991). Chapter 5.OXIDE TEXTURES - A MINI-ATLAS. In *Oxide Minerals* (pp. 129–220). De Gruyter. https://doi.org/10.1515/9781501508684-008

Hansen, S. E., Nyblade, A. A., & Benoit, M. H. (2012). Mantle structure beneath Africa and Arabia from adaptively parameterized P-wave tomography: Implications for the origin of Cenozoic Afro-Arabian tectonism. *Earth and Planetary Science Letters*, *319–320*, 23–34. https://doi.org/10.1016/j.epsl.2011.12.023

Hawkins, L. M. A., Anwar, T., Shcherbakova, V. V., Biggin, A. J., Kravchinsky, V. A., Shatsillo, A. V., & Pavlov, V. E. (2019). An exceptionally weak Devonian geomagnetic field recorded by the Viluy Traps, Siberia. *Earth and Planetary Science Letters*, *506*, 134–145. https://doi.org/10.1016/j.epsl.2018.10.035

Hawkins, L. M. A., Grappone, J. M., Sprain, C. J., Saengduean, P., Sage, E. J., Thomas-Cunningham, S., Kugabalan, B., & Biggin, A. J. (2021). Intensity of the Earth's magnetic field: Evidence for a Mid-Paleozoic dipole low. *Proceedings of the National Academy of Sciences*, *118*(34). https://doi.org/10.1073/pnas.2017342118

Hellio, G., & Gillet, N. (2018). Time-correlation-based regression of the geomagnetic field from archeological and sediment records. *Geophysical Journal International*, *214*(3), 1585–1607. https://doi.org/10.1093/GJI/GGY214

Hofmann, C., Courtillot, V., Féraud, G., Rochette, P., Yirgu, G., Ketefo, E., & Pik, R. (1997). Timing of the ethiopian flood basalt event and implications for plume birth and global change. *Nature*, *389*(6653), 838–841. https://doi.org/10.1038/39853

Hulot, G., & Gallet, Y. (2003). Do superchrons occur without any palaeomagnetic warning? *Earth and Planetary Science Letters*, *210*(1–2), 191–201. https://doi.org/10.1016/S0012-821X(03)00130-4

Kellogg, K., & Reynolds, R. (1983). Opening of the Red Sea: constraints from a palaeomagnetic study of the As Sarat volcanic field, south-western Saudi Arabia. *New York*, 649–665. https://doi.org/10.1111/j.1365-246X.1983.tb01898.x

Khokhlov, A., & Shcherbakov, V. (2015). Palaeointensity and Brunhes palaeomagnetic field models. *Geophysical Journal International*, *202*(2), 1419–1428. https://doi.org/10.1093/gji/ggv236

Kirschvink, J. L. (1980). The least-squares line and plane and the analysis of palaeomagnetic data. *Geophysical Journal International*, *62*(3), 699–718. https://doi.org/10.1111/j.1365-246X.1980.tb02601.x

Kissel, C., & Laj, C. (2004). Improvements in procedure and paleointensity selection criteria (PICRIT-03) for Thellier and Thellier determinations: application to Hawaiian basaltic long cores. *Physics of the Earth and Planetary Interiors*, *147*(2–3), 155–169. https://doi.org/10.1016/j.pepi.2004.06.010

Koenigsberger, J. G. (1938). Natural residual magnetism of eruptive rocks. *Journal of Geophysical Research*, *43*(3), 299. https://doi.org/10.1029/TE043i003p00299

Korte, M., Donadini, F., & Constable, C. G. (2009). Geomagnetic field for 0-3 ka: 2. A new series of time-varying global models. *Geochemistry, Geophysics, Geosystems*, *10*(6). https://doi.org/10.1029/2008GC002297

Kosterov, A. A., & Prévot, M. (1998). Possible mechanisms causing failure of Thellier palaeointensity experiments in some basalts. *Geophysical Journal International*, *134*(2), 554–572. https://doi.org/10.1046/j.1365-246x.1998.00581.x

Koymans, M. R., van Hinsbergen, D. J. J., Pastor-Galán, D., Vaes, B., & Langereis, C. G. (2020). Towards FAIR Paleomagnetic Data Management Through Paleomagnetism.org 2.0. *Geochemistry, Geophysics, Geosystems*, *21*(2). https://doi.org/10.1029/2019GC008838

Kulakov, E. v., Sprain, C. J., Doubrovine, P. v., Smirnov, A. v., Paterson, G. A., Hawkins, L., Fairchild, L., Piispa, E. J., & Biggin, A. J. (2019). Analysis of an Updated Paleointensity Database (Q_{PI} -PINT) for 65–200 Ma: Implications for the Long-Term History of Dipole Moment Through the Mesozoic. *Journal of Geophysical Research: Solid Earth*, *124*(10), 9999–10022. https://doi.org/10.1029/2018JB017287

le Bas, M. J. L., Maitre, R. W. L., Streckeisen, A., & Zanettin, B. (1986). A Chemical Classification of Volcanic Rocks Based on the Total Alkali-Silica Diagram. *Journal of Petrology*, *27*(3), 745–750. https://doi.org/10.1093/petrology/27.3.745

Lee, J. Y., Marti, K., Severinghaus, J. P., Kawamura, K., Yoo, H. S., Lee, J. B., & Kim, J. S. (2006). A redetermination of the isotopic abundances of atmospheric Ar. *Geochimica et Cosmochimica Acta*, *70*(17), 4507–4512. https://doi.org/10.1016/j.gca.2006.06.1563

Levi, S. (1977). The effect of magnetite particle size on paleointensity determinations of the geomagnetic field. *Physics of the Earth and Planetary Interiors*, *13*(4), 245–259. https://doi.org/10.1016/0031-9201(77)90107-8

Lhuillier, F., & Gilder, S. A. (2013). Quantifying paleosecular variation: Insights from numerical dynamo simulations. *Earth and Planetary Science Letters*, *382*, 87–97. https://doi.org/10.1016/j.epsl.2013.08.048

Lhuillier, F., & Gilder, S. A. (2019). Palaeomagnetism and geochronology of Oligocene and Miocene volcanic sections from Ethiopia: Geomagnetic variability in the Afro-Arabian region over the past 30 Ma. *Geophysical Journal International*, *216*(2), 1466–1481. https://doi.org/10.1093/gji/ggy517

Lhuillier, F., Gilder, S. A., Wack, M., He, K., Petersen, N., Singer, B. S., Jicha, B. R., Schaen, A. J., & Colon, D. (2016). More stable yet bimodal geodynamo during the Cretaceous superchron? *Geophysical Research Letters*, *43*(12), 6170–6177. https://doi.org/10.1002/2016GL069303

Lhuillier, F., Hulot, G., & Gallet, Y. (2013). Statistical properties of reversals and chrons in numerical dynamos and implications for the geodynamo. *Physics of the Earth and Planetary Interiors*, *220*, 19–36. https://doi.org/10.1016/j.pepi.2013.04.005

Lhuillier, F., Hulot, G., Gallet, Y., & Schwaiger, T. (2019). Impact of inner-core size on the dipole field behaviour of numerical dynamo simulations. *Geophysical Journal International*, *218*(1), 179–189. https://doi.org/10.1093/gji/ggz146

Lhuillier, F., Shcherbakov, V. P., Gilder, S. A., & Hagstrum, J. T. (2017a). Variability of the 0-3Ma palaeomagnetic field observed from the Boring Volcanic Field of

the Pacific Northwest. *Geophysical Journal International*, *211*(1), 69–79. https://doi.org/10.1093/GJI/GGX288

Lhuillier, F., Shcherbakov, V. P., Gilder, S. A., & Hagstrum, J. T. (2017b). Variability of the 0–3 Ma palaeomagnetic field observed from the Boring Volcanic Field of the Pacific Northwest. *Geophysical Journal International*, *211*(1), 69–79. https://doi.org/10.1093/gji/ggx288

Lhuillier, F., Shcherbakov, V. P., Shcherbakova, V. v, Ostner, S., Hervé, G., & Petersen, N. (2019). Palaeointensities of Oligocene and Miocene volcanic sections from Ethiopia: field behaviour during the Cainozoic. *Geophysical Journal International*, *216*(2), 1482–1494. https://doi.org/10.1093/gji/ggy491

Lowrie, W., & Kent, D. v. (2004). Geomagnetic polarity timescales and reversal frequency regimes. In *Geophysical Monograph Series* (Vol. 145, pp. 117–129). Blackwell Publishing Ltd. https://doi.org/10.1029/145GM09

Ludwig, K. R. (2008). Isoplot/ex ver. 3.6. *Berkley Geochronology Center. Spec. Publ 4*, *77*.

Mahoney & Coffin. (1997). *Large Igneous Provinces: Continental, Oceanic, and Planetary Flood Volcanism* (J. J. Mahoney & M. F. Coffin, Eds.). American Geophysical Union. https://doi.org/10.1029/GM100

McFadden, P. L., & Merrill, R. T. (1984). Lower mantle convection and geomagnetism. *Journal of Geophysical Research: Solid Earth*, *89*(B5), 3354–3362. https://doi.org/10.1029/JB089iB05p03354

McFadden, P. L., & Merrill, R. T. (2000). Evolution of the geomagnetic reversal rate since 160 Ma: Is the process continuous? *Journal of Geophysical Research: Solid Earth*, *105*(B12), 28455–28460. https://doi.org/10.1029/2000JB900258

McFadden, P. L., Merrill, R. T., McElhinny, M. W., & Lee, S. (1991). Reversals of the Earth's magnetic field and temporal variations of the dynamo families. *Journal of Geophysical Research: Solid Earth*, *96*(B3), 3923–3933. https://doi.org/10.1029/90JB02275

Meng, J., Lhuillier, F., Wang, C., Liu, H., Eid, B., & Li, Y. (2020). Paleomagnetism of Paleocene-Maastrichtian (60–70 Ma) Lava Flows From Tian Shan (Central

Asia): Directional Analysis and Paleointensities. *Journal of Geophysical Research: Solid Earth*, *125*(9). https://doi.org/10.1029/2019JB018631

Merrill, R. T., McElhinny, M. W. , & & McFadden, P. L. (1996). *The magnetic field of the earth: paleomagnetism, the core, and the deep mantle* (Vol. 63). Academic Press.

Min, K., Mundil, R., Renne, P. R., & Ludwig, K. R. (2000). A test for systematic errors in 40Ar/39Ar geochronology through comparison with U/Pb analysis of a 1.1-Ga rhyolite. *Geochimica et Cosmochimica Acta*, *64*(1), 73–98. https://doi.org/10.1016/S0016-7037(99)00204-5

Muxworthy, A. R. (2010). Revisiting a domain-state independent method of palaeointensity determination. *Physics of the Earth and Planetary Interiors*, *179*(1–2), 21–31. https://doi.org/10.1016/j.pepi.2010.01.003

Nagata, T., Arai, Y., & Momose, K. (1963). Secular Variation of the Geomagnetic Total Force during the Last 5000 Years. *Journal of Geophysical Research*, *68*(18), 5277–5281. https://doi.org/10.1029/j.2156-2202.1963.tb00005.x

Natali, C., Beccaluva, L., Bianchini, G., Ellam, R. M., Savo, A., Siena, F., & Stuart, F. M. (2016). High-MgO lavas associated to CFB as indicators of plume-related thermochemical effects: The case of ultra-titaniferous picrite-basalt from the Northern Ethiopian-Yemeni Plateau. *Gondwana Research*, *34*, 29–48. https://doi.org/10.1016/j.gr.2016.02.009

Nishitani, T., Kono, M. (1983). Curie temperature and lattice constant of oxidized titanomagnetite, *Geophysical Journal International*, Volume 74, Issue 2, August 1983, Pages 585–600, https://doi.org/10.1111/j.1365-246X.1983.tb01890.x

Ogg, J. G. (2020). Geomagnetic Polarity Time Scale. In *Geologic Time Scale 2020* (pp. 159–192). Elsevier. https://doi.org/10.1016/B978-0-12-824360-2.00005-X

Paterson, G. A. (2013). The effects of anisotropic and non-linear thermoremanent magnetizations on Thellier-type paleointensity data. *Geophysical Journal International*, *193*(2), 694–710. https://doi.org/10.1093/gji/ggt033

Paterson, G. A., Heslop, D., & Pan, Y. (2016). The pseudo-Thellier palaeointensity method: New calibration and uncertainty estimates. *Geophysical Journal International*, *207*(3), 1596–1608. https://doi.org/10.1093/gji/ggw349

Paterson, G. A., Tauxe, L., Biggin, A. J., Shaar, R., & Jonestrask, L. C. (2014). On improving the selection of Thellier-type paleointensity data. *Geochemistry, Geophysics, Geosystems*, *15*(4), 1180–1192. https://doi.org/10.1002/2013GC005135

Pekar, S., & Miller, K. G. (1996). New Jersey Oligocene "Icehouse" sequences (ODP Leg 150X) correlated with global δ18O and Exxon eustatic records. *Geology*, *24*(6), 567. https://doi.org/10.1130/0091-7613(1996)024<0567:NJOISO>2.3.CO;2

Perrin, M., & Shcherbakov, V. (1997). Paleointensity of the Earth's Magnetic Field for the Past 400 Ma: Evidence for a Dipole Structure during the Mesozoic Low. *Journal of Geomagnetism and Geoelectricity*, *49*(4), 601–614. https://doi.org/10.5636/jgg.49.601

Pick, T., & Tauxe, L. (1993). Geomagnetic palaeointensities during the Cretaceous normal superchron measured using submarine basaltic glass. *Nature*, *366*(6452), 238–242. https://doi.org/10.1038/366238a0

Pik, R., Deniel, C., Coulon, C., Yirgu, G., Hofmann, C., & Ayalew, D. (1998). The northwestern Ethiopian Plateau flood basalts: Classification and spatial distribution of magma types. In *Journal of Volcanology and Geothermal Research* (Vol. 81).

Pik, R., Deniel, C., Coulon, C., Yirgu, G., & Marty, B. (1999). Isotopic and trace element signatures of Ethiopian flood basalts: Evidence for plume-lithosphere interactions. *Geochimica et Cosmochimica Acta*, *63*(15), 2263–2279. https://doi.org/10.1016/S0016-7037(99)00141-6

Prévot, M., Derder, M. E.-M., McWilliams, M., & Thompson, J. (1990). Intensity of the Earth's magnetic field: Evidence for a Mesozoic dipole low. *Earth and Planetary Science Letters*, *97*(1–2), 129–139. https://doi.org/10.1016/0012-821X(90)90104-6

Prothero. (1994). The Late Eocene-Oligocene extinctions. *Annu. Rev. Earth Planet. Sci.*, *22*, 145–165. https://doi.org/10.1146/annurev.ea.22.050194.001045

Renne, P. R., Mundil, R., Balco, G., Min, K., & Ludwig, K. R. (2010). Joint determination of 40K decay constants and 40Ar*/40K for the Fish Canyon

sanidine standard, and improved accuracy for 40Ar/39Ar geochronology. *Geochimica et Cosmochimica Acta*, *74*(18), 5349–5367. https://doi.org/10.1016/j.gca.2010.06.017

Riisager, J., Perrin, M., & Rochette, P. (1999). Palaeointensity results from Ethiopian basalts: implications for the Oligocene geomagnetic field strength. *Geophysical Journal International*, *138*(2), 590–596. https://doi.org/10.1046/j.1365-246X.1999.00875.x

Riisager, P., Knight, K. B., Baker, J. A., Ukstins Peate, I., Al-Kadasi, M., Al-Subbary, A., & Renne, P. R. (2005). Paleomagnetism and 40Ar/39Ar Geochronology of Yemeni Oligocene volcanics: Implications for timing and duration of Afro-Arabian traps and geometry of the Oligocene paleomagnetic field. *Earth and Planetary Science Letters*, *237*(3–4), 647–672. https://doi.org/10.1016/j.epsl.2005.06.016

Rivera, T. A., Storey, M., Zeeden, C., Hilgen, F. J., & Kuiper, K. (2011). A refined astronomically calibrated 40Ar/39Ar age for Fish Canyon sanidine. *Earth and Planetary Science Letters*, *311*(3–4), 420–426. https://doi.org/10.1016/j.epsl.2011.09.017

Rochette, P., Tamrat, E., Féraud, G., Pik, R., Courtillot, V., Ketefo, E., Coulon, C., Hoffmann, C., Vandamme, D., & Yirgu, G. (1998). Magnetostratigraphy and timing of the Oligocene Ethiopian traps. In *Earth and Planetary Science Letters* (Vol. 164). https://doi.org/10.1016/S0012-821X(98)00241-6

Rooney, T. O. (2017). The Cenozoic magmatism of East-Africa: Part I — Flood basalts and pulsed magmatism. *Lithos*, *286–287*, 264–301. https://doi.org/10.1016/j.lithos.2017.05.014

Sahy, D., Hiess, J., Fischer, A. U., Condon, D. J., Terry, D. O., Abels, H. A., Hüsing, S. K., & Kuiper, K. F. (2020). Accuracy and precision of the late eocene-early oligocene geomagnetic polarity time scale. *Bulletin of the Geological Society of America*, *132*(1–2), 373–388. https://doi.org/10.1130/B35184.1

Schaen, A. J., Jicha, B. R., Hodges, K. v., Vermeesch, P., Stelten, M. E., Mercer, C. M., Phillips, D., Rivera, T. A., Jourdan, F., Matchan, E. L., Hemming, S. R., Morgan, L. E., Kelley, S. P., Cassata, W. S., Heizler, M. T., Vasconcelos, P. M.,

Benowitz, J. A., Koppers, A. A. P., Mark, D. F., … Singer, B. S. (2021). Interpreting and reporting 40Ar/39Ar geochronologic data. *Bulletin of the Geological Society of America*, *133*(3–4), 461–487. https://doi.org/10.1130/B35560.1

Selkin, P. A., & Tauxe, L. (2000). Long-term variations in palaeointensity. *Philosophical Transactions of the Royal Society of London. Series A: Mathematical, Physical and Engineering Sciences*, *358*(1768), 1065–1088. https://doi.org/10.1098/rsta.2000.0574

Shcherbakov, V., & Fabian, K. (2012). The geodynamo as a random walker: A view on reversal statistics. *Journal of Geophysical Research: Solid Earth*, *117*(B3). https://doi.org/10.1029/2011JB008931

Shcherbakov, V. P., Gribov, S. K., Lhuillier, F., Aphinogenova, N. A., & Tsel'movich, V. A. (2019). On the Reliability of Absolute Palaeointensity Determinations on Basaltic Rocks Bearing a Thermochemical Remanence. *Journal of Geophysical Research: Solid Earth*, *124*(8), 7616–7632. https://doi.org/10.1029/2019JB017873

Shcherbakov, V. P., Lhuillier, F., & Sycheva, N. K. (2021). Exact Analytical Solutions for Kinetic Equations Describing Thermochemical Remanence Acquisition for Single-Domain Grains: Implications for Absolute Paleointensity Determinations. *Journal of Geophysical Research: Solid Earth*, *126*(5). https://doi.org/10.1029/2020JB021536

Shcherbakov, V. P., & Shcherbakova, V. v. (2001). On the suitability of the Thellier method of palaeointensity determinations on pseudo-single-domain and multidomain grains. *Geophysical Journal International*, *146*(1), 20–30. https://doi.org/10.1046/j.0956-540x.2001.01421.x

Shcherbakov, V. P., & Sycheva, N. K. (2006). On the variation in the geomagnetic dipole over the geological history of the Earth. *Izvestiya, Physics of the Solid Earth*, *42*(3), 201–206. https://doi.org/10.1134/S1069351306030037

Shcherbakov, V. P., & Sycheva, N. K. (2013). On the intensity of the geomagnetic field in the geological past. *Izvestiya, Physics of the Solid Earth*, *49*(5), 699–717. https://doi.org/10.1134/S1069351313040095

Shcherbakova, V. v., Bakhmutov, V. G., Shcherbakov, V. P., Zhidkov, G. v., & Shpyra, V. v. (2012). Palaeointensity and palaeomagnetic study of Cretaceous and Palaeocene rocks from Western Antarctica. *Geophysical Journal International*, *189*(1), 204–228. https://doi.org/10.1111/j.1365-246X.2012.05357.x

Shcherbakova, V. v., Shcherbakov, V. P., & Heider, F. (2000). Properties of partial thermoremanent magnetization in pseudosingle domain and multidomain magnetite grains. *Journal of Geophysical Research: Solid Earth*, *105*(B1), 767–781. https://doi.org/10.1029/1999JB900235

Shcherbakova, V. v., Zhidkov, G. v., & Shcherbakov, V. P. (2008). Revised determination of the paleointensity in the cretaceous from the collection of A.S. Bol'shakov and G.M. Solodovnikov. *Izvestiya, Physics of the Solid Earth*, *44*(10), 816–821. https://doi.org/10.1134/S1069351308100091

Speijer, R. P., Pälike, H., Hollis, C. J., Hooker, J. J., & Ogg, J. G. (2020). The Paleogene Period. In *Geologic Time Scale 2020* (pp. 1087–1140). Elsevier. https://doi.org/10.1016/B978-0-12-824360-2.00028-0

Steiger, R. H., & Jäger, E. (1977). Subcommission on geochronology: Convention on the use of decay constants in geo- and cosmochronology. *Earth and Planetary Science Letters*, *36*(3), 359–362. https://doi.org/10.1016/0012-821X(77)90060-7

Sun, S. -s., & McDonough, W. F. (1989). Chemical and isotopic systematics of oceanic basalts: implications for mantle composition and processes. *Geological Society, London, Special Publications*, *42*(1), 313–345. https://doi.org/10.1144/GSL.SP.1989.042.01.19

Tadesse, M., Bekele, H., Mitiku, B., Teshome, M., Besufekade, A., Edris, M., Burussa, G., Yehualaeshet, E., Ashenafi, S., & Alemu, T. (2011). *Geology , Geochemistry and Gravity Survey of the Maychew Area*. *MEMOIR 31 December*, 61.

Tadesse, Melese; Bekele, Henok; Teshome, Meskerem; Besufekad, Asaminew; Mitiku, B. A. T. (2011). *Geological Map of The Maychew Area, Federal Democratic Republic of Ethiopia, Ministry of Mines, Geological Survey of Ethiopia*.

Tarduno, J. A., Cottrell, R. D., & Smirnov, A. v. (2001). High geomagnetic intensity during the mid-cretaceous from Thellier analyses of single plagioclase crystals. *Science*, *291*(5509), 1779–1783. https://doi.org/10.1126/science.1057519

Tarduno, J. A., Cottrell, R. D., & Smirnov, A. v. (2002). The Cretaceous superchron geodynamo: Observations near the tangent cylinder. *Proceedings of the National Academy of Sciences*, *99*(22), 14020–14025. https://doi.org/10.1073/pnas.222373499

Tauxe, L. (2005). Inclination flattening and the geocentric axial dipole hypothesis. *Earth and Planetary Science Letters*, *233*(3–4), 247–261. https://doi.org/10.1016/j.epsl.2005.01.027

Tauxe, L., Banerjee, S. K., Butler, R. F., & van der Voo R. (2018). *Essentials of paleomagnetism: Fifth Web Edition*. Univ of California Press.

Tauxe, L., & Kent, D. v. (2004). *A Simplified Statistical Model for the Geomagnetic Field and the Detection of Shallow Bias in Paleomagnetic Inclinations: was the Ancient Magnetic Field Dipolar?* (pp. 101–115). https://doi.org/10.1029/145GM08

Tauxe, L., Pick, T., & Kok, Y. S. (1995). Relative paleointensity in sediments: A Pseudo-Thellier Approach. *Geophysical Research Letters*, *22*(21), 2885–2888. https://doi.org/10.1029/95GL03166

Tauxe, L., & Staudigel, H. (2004). Strength of the geomagnetic field in the Cretaceous Normal Superchron: New data from submarine basaltic glass of the Troodos Ophiolite. *Geochemistry, Geophysics, Geosystems*, *5*(2), article 11. https://doi.org/10.1029/2003GC000635

Thébault, E., Finlay, C. C., Beggan, C. D., Alken, P., Aubert, J., Barrois, O., Bertrand, F., Bondar, T., Boness, A., Brocco, L., Canet, E., Chambodut, A., Chulliat, A., Coïsson, P., Civet, F., Du, A., Fournier, A., Fratter, I., Gillet, N., … Zvereva, T. (2015). International Geomagnetic Reference Field: the 12th generation. *Earth, Planets and Space*, *67*(1), 79. https://doi.org/10.1186/s40623-015-0228-9

Touchard, Y., Rochette, P., Aubry, M. P., & Michard, A. (2003). High-resolution magnetostratigraphic and biostratigraphic study of Ethiopian traps-related products in Oligocene sediments from the Indian Ocean. *Earth and Planetary*

Science Letters, 206 (3-4), 493–508. https://doi.org/10.1016/S0012-821X(02)01084-1

Turner, G. M., Rasson, J., & Reeves, C. (2015). Observation and Measurement Techniques. In *Treatise on Geophysics: Second Edition* (Vol. 5, pp. 91–135). Elsevier Inc. https://doi.org/10.1016/B978-0-444-53802-4.00098-1

Ukstins, I. A., Renne, P. R., Wolfenden, E., Baker, J., Ayalew, D., & Menzies, M. (2002). Matching conjugate volcanic rifted margins: 40Ar/39Ar chrono-stratigraphy of pre- and syn-rift bimodal flood volcanism in Ethiopia and Yemen. *Earth and Planetary Science Letters*, *198*(3–4), 289–306. https://doi.org/10.1016/S0012-821X(02)00525-3

Vandamme, D. (1994). A new method to determine paleosecular variation. *Physics of the Earth and Planetary Interiors*, *85*(1–2), 131–142. https://doi.org/10.1016/0031-9201(94)90012-4

Wack, M. R., & Gilder, S. A. (2012). The SushiBar: An automated system for paleomagnetic investigations. *Geochemistry, Geophysics, Geosystems*, *13*(12). https://doi.org/10.1029/2011GC003985

Warren. (1969). X.ray diffraction. *Addison-Wesley Series in Metallurgy and Materials*.

Westerhold, T., Röhl, U., Pälike, H., Wilkens, R., Wilson, P. A., & Acton, G. (2014). Orbitally tuned timescale and astronomical forcing in the middle Eocene to early Oligocene. *Climate of the Past*, *10*(3), 955–973. https://doi.org/10.5194/cp-10-955-2014

Xu, S., & Dunlop, D. J. (2004). Thellier paleointensity theory and experiments for multidomain grains. *Journal of Geophysical Research: Solid Earth*, *109*(B7). https://doi.org/10.1029/2004JB003024

Yoshimura, Y., Yamazaki, T., Yamamoto, Y., Ahn, H., Kidane, T., & Otofuji, Y. (2020). Geomagnetic Paleointensity Around 30 Ma Estimated From Afro-Arabian Large Igneous Province. *Geochemistry, Geophysics, Geosystems*, *21*(12). https://doi.org/10.1029/2020GC009341

Yu, Y., Dunlop, D. J., & Özdemir, Ö. (2003). Are ARM and TRM analogs? Thellier analysis of ARM and pseudo-Thellier analysis of TRM. *Earth and Planetary*

Science Letters, *205*(3–4), 325–336. https://doi.org/10.1016/S0012-821X(02)01060-9

Zijderveld, J. D. A. (1967). The natural remanent magnetizations of the exeter volcanic traps (Permian, Europe). *Tectonophysics*, *4*(2), 121–153. https://doi.org/10.1016/0040-1951(67)90048-0

9. Acknowledgment

This contribution would not have been possible if it weren't for the assistance I received from several people. I would like to thank Jörg Pfänder and Blanka Sperner for conducting and interpreting the Ar-Ar measurements; Donjá Aßbichler for helping me with sample preparation and conduting the XRF measurements; Valeriy Shcherbakov and Valentina Shcherbakova for assisting me with performing and interpreting the absolute palaeointensity measurements. I express my deepest gratitude to Florian Lhuillier who helped me through every step with his valuable advice and guidance from field work, laboratory work, data analysis to writing my papers and writing of the thesis. Special thanks to Stuart Gilder whose door was always open for any and all questions, allowing for the communication of invaluable advice throughout my time as a master's student and especially during my time as a PhD candidate.

No words can serve Valerian Bachtadse justice, for without his empathy I am sure that I wouldn't even have gotten into the geophysics masters program in Munich, let alone be writing this thesis. I appreciate all the help I received from my fellow colleague Vinzenz Weissbrodt who was always supporting me from the beginning of my studies in Munich from our time together as masters' students and all the way until the end, be it by instructing me in mathematics or helping me how to express any idea scientifically. I want to also acknowledge the support I received from my colleagues and close friends Sandra Ostner and Mandana Parsi who were next to me ever since we were masters' students and all throughout our time as PhD candidates.

Any expression of gratitude is incomplete without expressing thanks for one's family, particularly my parents, brothers, uncles, and aunts for their financial and emotional support throughout my studies. As to the family I chose, it's the people who were always by my side brightening my day and giving me the energy and patience to soldier through and achieve my goals in life. Finally, I want to express my appreciation for having my fiancé Lama Al Jurdi by my side, who cheered me through the rough times, pushed me to be better and encouraged me to work harder to finish my thesis.

I would finally like to thank the Deutsche Forschungsgemeinschaft (German Research Foundation, DFG) for financing this doctoral work through grants and LH55/4-1 and LH55/5-1 (405632737).